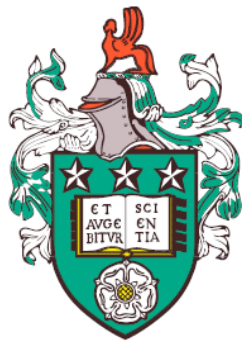


Polymerisation-induced self-assembly of liquid crystalline block copolymers



Bartłomiej Wojciech Czubak
Department of Physics and Astronomy
University of Leeds

A thesis submitted for the degree of

Doctor of Philosophy

November 2022

This thesis is dedicated to Agnieszka, for all her love and support.

Acknowledgements

My thanks to my supervisors, Mamatha and Nick, for your patience and guidance.

The entire Aubergine Room, may it live on in our hearts only because we all know it should not be out in the public.

And I know Dan, you might be tired of hearing it, but thanks for everything you've done to help me out throughout the last few years.

"The result, therefore, of our present enquiry is, that we find no vestige of a beginning, - no prospect of an end."

James Hutton, 1788

Declaration of Academic Integrity

The candidate confirms that the work submitted is his own, except where work which has formed part of jointly authored publications has been included. The contribution of the candidate and the other authors to this work has been explicitly indicated below. The candidate confirms that appropriate credit has been given within the thesis where reference has been made to the work of others. This copy has been supplied on the understanding that it is copyright material and that no quotation from the thesis may be published without proper acknowledgement. The right of Bartłomiej Wojciech Czubak to be identified as Author of this work has been asserted by Bartłomiej Wojciech Czubak in accordance with the Copyright, Designs and Patents Act 1988.

COVID-19 impact statement

Due to the global pandemic of COVID-19, the work presented in this thesis has been significantly affected, leading to increased challenges and complications. Below are the summarised impacts:

1. Being unable to attend university laboratories between March and September 2020.
2. Having a restricted access to the laboratories between September 2020 and April 2021.
3. Increased challenges in collaboration with other groups and external laboratories such as for x-ray scattering experiments at external synchrotron facilities and attendance of in person conferences.

On top of the above mentioned impact of the pandemic, this project was also affected by the migration of the Physics and Astronomy department and laboratories to a new building on campus which led to further two months of lab shutdowns in April and May 2021.

The impact of these events cannot be understated. It was offset to some degree by receiving a three month extension to complete the studies.

Conferences and Workshops

1. Poster presentation at BLCS 2019 Conference, Leeds, UK
2. Oral presentation at Smart NanoMaterials 2019 Conference, Paris, FR
3. BLCS Winter Workshop 2020, Birmingham, UK
4. Poster presentation at BLCS 2021 Conference, Online
5. Oral Presentation at BLCS 2022 Conference, Bristol, UK
6. Poster presentation at ILCC 2022 Conference, Lisbon, PT

Publications

1. **Czubak, B.**; Warren, N.J.; Nagaraj, M. Steroid-Based Liquid Crystalline Polymers: Responsive and Biocompatible Materials of the Future. *Crystals* **2022**, *12*, 1000. <https://doi.org/10.3390/cryst12071000>
2. **Czubak, B.**; Warren, N.J.; Nagaraj, M. Evolution of morphology in liquid crystalline nanoobjects prepared via polymerisation-induced self-assembly, Manuscript in preparation

Abstract

As we approach the technical limits of size scalability of electronics for the next generation of electronic devices, interest grows in novel materials with controllable feature sizes in the sub-10nm regime. Complex self-assembly behaviour has therefore become a significant area of research, both within academia as well as industry.

This thesis is concerned with the self-assembly behaviour of liquid crystalline block copolymers based on methacrylic backbone synthesised via reversible-addition fragmentation chain-transfer (RAFT) polymerisation. In particular, the effects of incorporation of liquid crystalline elements on the polymerisation-induced self-assembly (PISA) is investigated. PISA has in recent years been established as an effective method of preparing tunable nanostructures from copolymers. The morphology of these structures can be controlled based on reaction variables such as % solids, solvent and block fractions. Introduction of mesogens into the self-assembly process offers another potential way of controlling the self-assembly process.

Other methods can be used to manipulate the resulting morphologies of the nanoparticles and films once prepared. Within this thesis, the impact of thermal and solvent annealing on the thin films are investigated on thin films formed by the prepared LCBCPs.

Abbreviations

BCP	Block Copolymer
LC	Liquid Crystal
LCBCP	Liquid crystalline block copolymer
SCLP	Side chain liquid-crystallien polymer
LMWLC	Low-molecular weight liquid crystal
HMWLC	High-molecular weight liquid crystal
N*	Chiral Nematic
Sm	Smectic
δn	Birefringence
f	Volume fraction
χ	Flory–Huggins interaction parameter
DP	Degree of polymerisation
PD	Polydispersity
T_g	Glass transition temperature
T_{Cl}	Clearing temperature
RDRP	Reversible Deactivation Radical Polymerisation
RAFT	Reversible addition-fragmentation chain-transfer polymerization
CTA	chain transfer agent
mCTA	macro-chain transfer agent
PISA	Polymerisation-induced self-assembly
PI	Polyimide layer

Contents

1	Introduction	14
1.1	Liquid crystals	14
1.2	Types of mesophases	17
1.3	Chemical structures of mesogens	20
1.4	Polymers	23
1.4.1	Copolymers	23
1.4.2	Block copolymers	23
1.4.3	Liquid crystalline polymers	24
1.4.4	Perfluorinated LC polymers	26
1.4.5	Cholesterol-based LC polymers	27
1.5	Polymer synthesis	30
1.5.1	Reversible Deactivation Radical Polymerisation (RDRP)	30
1.5.2	Reversible addition-fragmentation chain-transfer polymerization (RAFT)	31
1.6	Self-assembly of block copolymers in thin films	32
1.7	Polymerisation-induced self-assembly	34
1.8	Aims and motivation	37
1.9	Thesis outline	38
2	Experimental methods	40
2.1	Liquid crystal sandwich devices	40
2.1.1	Standard liquid crystal device	40
2.1.2	Fabrication process	41
2.2	Characterisation of materials	45
2.2.1	Polarised Optical Microscopy (POM)	45

2.2.2	Differential Scanning Calorimetry (DSC)	47
2.2.3	X-ray scattering	50
2.2.4	Data analysis	54
2.2.5	Equipment used	54
2.2.6	Transmission electron microscopy (TEM)	54
2.2.7	Atomic force microscopy (AFM)	56
2.2.8	Ellipsometry	59
2.3	Synthetic characterisation	59
2.3.1	Solvents and materials	60
2.3.2	Thin layer chromatography	60
2.3.3	Column chromatography	60
2.3.4	NMR spectroscopy	61
3	Synthesis of liquid-crystalline methacrylic monomers bearing cholesteryl and cyanobiphenyl mesogens.	62
3.1	Introduction	62
3.2	Methacrylic monomers bearing mesogenic groups.	62
3.3	Synthesis of 6-(Methacryloyloxy)hexanoic acid 3-cholesteryl ester (Chol-6-MA)	64
3.3.1	Step 1: Preparation of acyl chloride	65
3.3.2	Step 3: Addition of methacrylic group	70
3.3.3	Synthesis of 6-(4-Cyano-biphenyl-4'-yloxy)hexyl methacrylate (CB-6-MA)	73
3.3.4	Notes and unsuccessful attempts at preparing the monomers	75
4	Self-assembly of liquid crystalline block copolymers bearing mesogenic perfluorinated side groups	76
4.1	Introduction	76
4.2	Background	78
4.3	Synthesis	79
4.3.1	Synthesis of macro chain-transfer agent	80
4.3.2	Preparation of $S_{11} - F_x$ (S = PStMA, B = PFOEMA, subscript represents DPs) assemblies by PISA.	81
4.4	Results and discussion	83

4.4.1	Characterisation of $S_{11} - F_x$ diblock copolymers	83
4.4.2	Morphology of PStMA-b-PFOEMA nanoobjects	85
4.4.3	Summary of results	99
5	Liquid-crystalline behaviour of the polymethacrylate block copolymers bearing cholesterol and cyanobiphenyl side chains	100
5.1	Introduction	100
5.2	Cholesteryl and cyanobiphenyl liquid crystals	100
5.3	Synthesis	101
5.3.1	Synthesis of monomers	101
5.3.2	Synthesis of homopolymers	102
5.3.3	Synthesis of copolymers	103
5.4	Liquid crystalline behaviour	104
5.4.1	Intermediates	104
5.4.2	Monomers	105
5.4.3	Homopolymers	115
5.4.4	Copolymers	117
5.5	PISA nanostructures	120
5.6	Conclusions	122
6	Self-assembly and applications of block copolymers in thin films	123
6.1	Overview	123
6.2	Materials and sample preparation	124
6.3	Self-assembly in thin films	124
6.3.1	Self-assembly of SEBS	125
6.3.2	Self-assembly of PStMA-b-PFOEMA	130
6.3.3	Self-assembly of PChol6MA-b-PCB6MA	133
6.3.4	Conclusion	137
7	Conclusions	139
A	Appendix	142
	References	166

List of Figures

1.1	Schematic representation of a liquid crystalline phase found in between the crystalline and isotropic liquid phases.	15
1.2	An example chemical structure of (a) Discotic and (b) Calamitic liquid crystals and their analogous nematic phases.	17
1.3	Schematic of a nematic liquid crystalline. The director (\mathbf{n}) describes average orientation of the anisotropic axis of the molecules.	18
1.4	A half-pitch of a chiral nematic phase (180° twist). \mathbf{n} marks the director.	19
1.5	Smectic A (SmA) and Smectic C (SmC) phases. n is the director and θ is the tilt angle of smectic layer in reference to layer normal. In SmA phase, \mathbf{n} lies parallel to the layer normal where as in SmC \mathbf{n} lies at an angle to the layer normal.	20
1.6	(a) Chemical structure of 4-Cyano-4'-pentylbiphenyl (5CB) liquid crystal molecule with the features contributing to its mesogenic properties highlighted. (b) Schematic diagram showing the antiparallel configuration of two 5CB molecules. The blue arrow indicates the direction of the permanent dipoles of each of the molecules.	21
1.7	Chemical structure of (a) typical sterol and (b) cholesterol.	22
1.8	Example of a block copolymer structure.	24
1.9	Example of liquid crystalline polymers. (a) side chain polymers (b) main chain polymers. The ovals represent the mesogenic groups. The green lines correspond to the chemical linkage between the mesogenic groups.	25

LIST OF FIGURES

1.10	An example of the influence of chemical differences in the spacer connecting the backbone and the cholesteryl mesogen, on the liquid crystallinity of the material. The introduction of each of the ester groups (A–C) gradually increases the relative stiffness of the backbone. N*—chiral nematic, I— isotropic, G—glass, Cr—crystal and Sm—smectic.	29
1.11	Examples of architectures of copolymers which can be synthesised by Reversible Deactivation Radical Polymerisation (RDRP) methods.	31
1.12	Mechanism of Reversible addition-fragmentation chain-transfer (RAFT) polymerisation. Step 1 - A source of free-radicals such as an initiator starts the reaction by forming available radical species. Step 2 - The radical monomer reacts with the RAFT agent forming an early polymer. Step 3 - The leaving group radical reacts with another monomer to form another active chain. Step 4 - The main equilibrium of the RAFT reaction where the present radicals propagate chain growth where the rate of the chain growth is controlled by the available radicals leading to narrow PD in the resulting polymers. Step 5 - Two alive chains undergo a bi-radical termination leading to a 'dead' chain which can not react further.	32
1.13	Examples of structures formed by the self-assembly mechanism in block copolymers. The f in the block corresponds to the volume fraction of one of the blocks.	33
1.14	Theoretical phase diagram of diblock copolymer melts calculated by the mean-field theory SCFT. χ is interaction parameter, N is the total number of segments, f_a is the volume fraction of block a. The phases are denoted as SPH (spherical), CYL (cylindrical), LAM (lamellar), GYR (gyroid), and DIS (disordered). ^[1]	34
1.15	Schematic representation of the self-assembly process in polymerisation-induced self-assembly (PISA).	35
1.16	Example of complex nanostructures of P2VA obtained via PISA (a) spheres, (b) worms, (c) vesicles, (d) 'yolk/shell' and (e) multi-shelled vesicles. Reproduced with permission from ^[2]	37

LIST OF FIGURES

2.1	(a) Side view of a typical LC sandwich device. (b) Top view of the same device.	41
2.2	Clean room in the Sir William Henry Bragg Building. The gold light is used to ensure photosensitive samples are not exposed to light.	43
2.3	(a) Schematic of unpolarised light passing through the polariser becomes linearly polarised, which when passes through the birefringent sample becomes elliptically polarised. (b) Diagram of polarised light microscope setup in transmission mode. The light passing through the liquid crystalline sample material leads changes the lights polarisation from linear to ellipsoidal which is then passed through the analyser and into the detector (i.e. camera) and eye pieces.	46
2.4	Oily streak texture of a chiral nematic material observed under POM at 20x magnification, reflection mode at 40°C. Arrows indicate the directions of polariser (P) and analyser (A). Scale bar = 1 μ m.	47
2.5	A schematic representation of the DSC setup showing the difference between the sample and the reference pan. Both of the pans are sealed airtight. The furnace chamber is filled with nitrogen during the run.	48
2.6	DSC heat flow trace for 5CB measured at 10K min ⁻¹ . A significant endothermic event is observed at phase transition from crystal (K) to nematic (N) and a smaller one for the nematic (N) to isotropic (I). On cooling, an exothermic event was observed where the sample shows negative heat flow as it transitions from I to N. The top and bottom traces correspond to cooling and heating respectively. The crystallisation was not observed on cooling due to super cooling of 5CB.	49
2.7	DSC heat flow trace for a glass transition of a pure FOEMA polymer (DP = 50) blockcopolymer.	50

LIST OF FIGURES

2.8	Diagram demonstrating small-angle X-ray scattering (SAXS) within two spherical particles with different diameters. (a) Larger particle diameter leads to smaller scattering (b) Small particle diameter leads to wider scattering	52
2.9	An example EDS spectrum collected for a block copolymer of PStMA-b-PFOEMA. The spectrum indicates high relative presence of fluorine group, indicating high abundance of the group within the region scanned in TEM.	53
2.10	(a) Diagram of transmission electron microscopy (TEM) setup. The green indicates electron beam path. (b) A typical copper TEM grid. Within each segment of the grid, multiple periodic holes can be found. The grid is suspended on a Polyvinyl formal and holey carbon support films.	55
2.11	An example TEM image of a block copolymer nanoparticle prepared via polymerisation-induced self-assembly. Scale bar = 500nm	56
2.12	A schematic representation of how Atomic Force Microscope works. The laser is constantly scanning the probe which deflects as it interacts with the surface. The reflection of the laser is then measured by the photodiode which passes the data to the detector and controller. Controller than adjusts the position of the scanner based on the setting of the feedback loop.	57
2.13	An example of a cantilever used for AFM experiments.	57
2.14	A schematic representation of how a typical ellipsometer operates. ϕ is the angle between the detector/light source and the sample surface normal.	59
3.1	Molecular structures of the starting material, intermediate and the end product of Chol-6-MA	64
3.2	Experimental setup for the preparation of acyl chloride through reaction of thionyl chloride with a carboxylic acid.	65
3.3	Experimental setup for the reaction of acyl chloride and an alcohol.	67
3.4	Experimental setup for the reaction of acyl chloride and an alcohol.	70

LIST OF FIGURES

4.1	Synthetic pathway for preparing PStMA-b-PFOEMA block copolymer via PISA	80
4.2	Assigned 1H NMR spectra for the PStMA mCTA prepared via RAFT synthesis.	80
4.3	Conversion of FOEMA vs. polymerisation time, calculated by 1H NMR performed at $80^\circ C$ in n-dodecane using the StMA ₁₁ mCTA and AIBN at 15%, [mCTA]:[AIBN] = 2.	82
4.4	Thermogravimetric analysis (TGA) of $S_{11} - F_{25}$. Two discrete steps were observed for the material. The blocks were assigned based on the relative mass of each of the fragments based on the degree of polymerisation.	84
4.5	DSC onset temperature of transition (left) and enthalpy of change (right) of melting of (A) StMA block and (B) FOEMA block. . .	85
4.6	Transmission electron microscopy (TEM) micrographs of PStMA ₁₀ -b-PFEOMAn nanoparticles prepared via RAFT mediated PISA stained with ruthenium tetroxide. (a) n = 10, spherical micelles, (b) n = 20, cylindrical micelles, (c) n = 35, ellipsoidal vesicles, (d) n = 50, ellipsoidal vesicles, (e) b = 75, large compound vesicles (f) n = 100, large compound vesicles. Insets show zoomed in sections. Black scale bar corresponds to $1\mu m$	87
4.7	TEM micrographs of $S_{11} - F_{20}$ showing the fusion of the ellipsoidal particles to form 1D cylindrical micelles. Inset shows the fusion overlap between the outer walls of the particles. Scale bar = $0.5\mu m$	88
4.8	TEM micrographs of $S_{11} - F_{35}$ particles at different stages of the opening progress. (A) Fully closed cylinder. (B) Partially open cylinder ('needle eye'), (C) Fully open ellipsoidal vesicles (note, the holes in the background are from the holey carbon film the particles were suspended on).	89
4.9	A TEM micrograph of (A) the $S_{11} - F_{50}$ nanoobjects with highlighted membrane thickness. (B) The membrane with its internal layer visible.	90
4.10	A schematic representation of the morphology evolution of $S_{11} - F_x$ block copolymer series.	90

LIST OF FIGURES

4.11 (a) Hydrodynamic radius (D_h) calculated for PStMA ₁₀ - FEOMA _x in n-dodecane at approx. 1% w/w. (b) The polydispersity index and the size distribution from DLS of the nanoobjects in n-dodecane at approx. 1% w/w. The DP corresponds to the degree of polymerisation of the FOEMA block.	91
4.12 (A) A WAXS scattering pattern of $S_{11} - F_{35}$ measured at 1% in n-dodecane at room temperature. The d-spacing and q values of the peaks highlighted. (B) WAXS scattering pattern of $S_{11} - F_{35}$ measured at 27°C , 80°C and at 27°C again after cooling down. The peaks at $q = 1.8nm^{-1}$ and $q = 3.8nm^{-1}$ were found to disappear on heating past transition temperature and reappear on cool although more broad and weaker in intensity.	93
4.13 A schematic representation of the Smectic A order of PFOEMA side groups in the vesicular walls as indicated by the WAXS results.	94
4.14 Small-angle X-ray scattering (SAXS) patterns recorded for a 1.0% w/w dispersion of $S_{11} - F_n$ nanoparticles in n-dodecane. The individual spectra have been offset in the intensity y-axis in order to not overlap.	95
4.15 Fitting of $T_m = kx^a$ to the membrane thickness calculated from SAXS for the $S_{11} - F_n$ series and the hydrodynamic radius (D_h) calculated from DLS.	96
4.16 Polarised optical microscopy (POM) images of the $S_{11} - F_{35}$ in 15% w/w in n-dodecane at (A) 25°C and (B) 125°C. Samples were held in between cover slips with no alignment layers. Magnification = 20x The solution remained isotropic and no textures or otherwise were observed. Black scale bar = 500 μ m.	97
4.17 Polarised optical microscopy (POM) images of bulk $S_{11} - F_{35}$ at (A) 100°C and (B) 150°C. Samples were held in between cover slips with no alignment layers. Magnification = 20x. The texture of Smectic A observed in (B) was short lived only forming on rapid heating at a rate of 10 $kmin^{-1}$. Black scale bar = 500 μ m.	98

LIST OF FIGURES

5.1	Molecular structures of homopolymers of PChol6MA, PCB6MA and block copolymer of PChol6MA-b-PCB6MA.	101
5.2	Molecular structures of the starting material, intermediate and the end product of Chol-6-MA	102
5.3	(a) Chemical structure of Chol-6-Br. (b) POM image of Chol-6-Br taken in a cover slip with no alignment layer on heating. Transmission mode, 20x magnification. Black scale bar = 500 μ m.	105
5.4	^1H NMR spectrum of Chol-6-MA with chemical structure and atom assignment. Values: ^1H NMR (CDCl_3): 0.65–2.1 (50H, m, CH,CH ₂ ,CH ₃), 2.30 (4H, m, CH ₂), 4.13 (2H, t, J 5 6.7 Hz, CH ₂), 4.60 (1H, m, CH), 5.37 (1H, m), 5.53 (1H, m), 6.08 (1H, bs)	107
5.5	(a) Chemical structure and phase sequence of Chol-6-MA. (b) POM image of Chol-6-MA taken in a cover slip with no alignment layer on heating. Transmission mode, 20x magnification, scale bar = 500 μ m	109
5.6	POM image of gradual phase transition of 6-(Methacryloyloxy)hexanoic acid 3-cholesteryl ester (Chol-6-MA) taken in a cover slip with no alignment layer held at 44.8°C for (a) 0 min, (b) 2min (c) 3min and (d) 6min after cooling from isotropic at rate of 5kmin ⁻¹ . Transmission mode, 20x magnification. Scale bar = 500 μ m.	111
5.7	POM image of gradual colour changed of Chol-6-MA taken in a 5 μ m cell with planar alignment (a) 26.3°C, (b) 28.0°C (c) 34°C and (d) 45.8°C after cooling from isotropic at rate of 5kmin ⁻¹ . Transmission mode, 20x magnification. Scale bar = 500 μ m.	112
5.8	Peak selective reflection wavelength of Chol-6-MA monomer as a function of temperature recorder with a UV-Vis Spectrometer connected to a reflection microscope in a 5 μ m cell with planar alignment.	113
5.9	^1H NMR spectrum of CB-6-MA with chemical structure and atom assignment. Values: ^1H NMR (CDCl_3): 1.4-2.1 (9H,m,CH,CH ₂ ,CH ₃), 2.6 (2H,t,CH ₂), 4.2 (2H,t,CH ₂), 5.6 (1H,m), 6.1 (1H,m), 7.0 - 8.0 (8H, m, aromatic)	114

LIST OF FIGURES

5.10 POM images of $PChol_{50}$ taken in between unaligned cover slips (a) 90.7°C , (b) 150.0°C (c) 165.7°C and (d) 169.7°C after cooling from isotropic at rate of 5kmin^{-1} . Transmission mode, 20x magnification. Scale bar = $500\mu\text{m}$	115
5.11 POM images of $PCB - 6 - MA_{50}$ taken in between unaligned cover slips (a) 20°C , (b) 70°C after cooling from isotropic at rate of 10kmin^{-1} . Transmission mode, 20x magnification. Scale bar = $500\mu\text{m}$	116
5.12 POM images of $PCB - 6 - MA_{100}$ taken in between unaligned cover slips (a) 40°C , (b) 50°C (b) 70°C and (d) 160°C after cooling from isotropic at rate of 10kmin^{-1} . Transmission mode, 20x magnification. Scale bar (b) = $500\mu\text{m}$, (a)(c)(d) = $1000\mu\text{m}$	116
5.13 POM images of $PChol_{50} - b - PCB_{50}$ taken in a $27.9\mu\text{m}$ cell with planar alignment (a) 95.0°C , (b) 130.0°C (c) 140.0°C and (d) 195.0°C after cooling from isotropic at rate of 2.5kmin^{-1} . Transmission mode, 20x magnification. Scale bar = $500\mu\text{m}$	118
5.14 POM images of $PChol_{50} - b - PCB_{100}$ taken in a $33.9\mu\text{m}$ cell with planar alignment (a) 90.7°C , (b) 125.0°C (c) 142.5°C and (d) 152.5°C after cooling from isotropic at rate of 2.5kmin^{-1} . Transmission mode, 20x magnification. Scale bar = $500\mu\text{m}$	119
5.15 POM images of $PChol_{50} - b - PCB_{150}$ taken in a $30.4\mu\text{m}$ cell with planar alignment (a) 114.0°C , (b) 125.0°C (c) 140.0°C and (d) 192.0°C after cooling from isotropic at rate of 2.5kmin^{-1} . Transmission mode, 20x magnification. Scale bar = $500\mu\text{m}$	120
5.16 AFM micrographs for height profiles for (a) $PChol_{50} - b - PCB_{50}$, (b) $PChol_{50} - b - PCB_{100}$ and (c) $PChol_{50} - b - PCB_{150}$. Samples were prepared by spin casting 1% solution of the stock solution onto cleaned silicon wafers at 3000RPM for 20 seconds.	121
6.1 Surface profile of a silicon wafer covered with 0.8% SEBS solution and thermally annealed using cyclohexane.	126

LIST OF FIGURES

6.2	AFM images of SEBS Control sample prepared from 0.8% solution of pure SEBS in toluene, spin cast at 3000RPM for 20seconds and left at ambient temperature for 22 hours. (A) - Height profile (B) - Phase profile	127
6.3	AFM images of SEBS sample prepared from 0.8% solution of pure SEBS in toluene, spin cast at 3000RPM for 20seconds and solvent annealed with toluene for 22 hours. (A) - Height profile (B) - Phase profile Inset in (B) corresponds to the FFT of the phase image.	128
6.4	Top left to bottom right diagonal cross section of (a) height and (b) phase images of Figure 6.5 respectively.	129
6.5	AFM images of SEBS sample prepared from 0.8% solution of pure SEBS in toluene, spin cast at 3000RPM for 20seconds and thermal annealed at 140°C for 22 hours. (A) - Height profile (B) - Phase profile. Inset in (B) corresponds to the FFT of the phase image.	129
6.6	AFM images of $PStMA_{11} - b - PFOEMA_{50}$ prepared from 0.8% solution of precipitated polymer in THF, spin cast at 3000RPM for 20 seconds and left at ambient for 24 hours. (A) - Height profile (B) - Phase profile. Inset in (B) corresponds to the FFT of the phase image.	130
6.7	AFM images of $PStMA_{11} - b - PFOEMA_{50}$ prepared from 0.8% solution of precipitated polymer in THF, spin cast at 3000RPM for 20 seconds and thermally annealed at 150°C for 24 hours. (A) - Height profile (B) - Phase profile. Inset in (B) corresponds to the FFT of the phase image.	131
6.8	AFM images of $PStMA_{11} - b - PFOEMA_{50}$ prepared from 0.8% solution of precipitated polymer in THF, spin cast at 3000RPM for 20 seconds and solvent vapour annealed with cyclohexane at for 24 hours. (A) - Height profile (B) - Phase profile. Inset in (B) corresponds to the FFT of the phase image.	132

LIST OF FIGURES

6.9	Height (left) and phase (right) AFM micrographs of PChol ₅₀ -b-PCB ₅₀ . (a) Control sample left at ambient conditions for 24 hours. (b) Solvent vapour annealed sample by exposure to toluene for 22hours at ambient room temperature. (c) Thermally annealed sample prepared at 100°C for 24 hours.	134
6.10	Height (left) and phase (right) AFM micrographs of PChol ₅₀ -b-PCB ₁₀₀ . (a) Control sample left at ambient conditions for 24 hours. (b) Solvent vapour annealed sample by exposure to toluene for 22hours at ambient room temperature. (c) Thermally annealed sample prepared at 100°C for 24 hours.	135
6.11	Height (left) and phase (right) AFM micrographs of PChol ₅₀ -b-PCB ₁₅₀ . (a) Control sample left at ambient conditions for 24 hours. (b) Solvent vapour annealed sample by exposure to toluene for 22hours at ambient room temperature. (c) Thermally annealed sample prepared at 100°C for 24 hours.	136
7.1	The number of publications containing the phrases 'liquid crystal' and 'polymerisation-induced self-assembly' per year as per Google Scholar. Accessed in 2022.	140

Chapter 1

Introduction

This introductory chapter provides relevant key background information for the results and experiments described in this thesis. It describes the some of the fundamentals of liquid crystals and polymers and their synthesis with focus on methods such as reversible addition-fragmentation chain-transfer polymerization and polymerisation-induced self-assembly.

1.1 Liquid crystals

Liquid crystals are a state of matter exhibited by certain organic molecules between the isotropic liquid and an ordered solid state (Figure 1.1). The word 'mesophase' was first used by Friedel to explain the liquid crystalline behaviour and comes from the Greek word for 'middle'. Liquid crystals) can be summarised as having properties of liquids (i.e. flow) and crystals (i.e. positional and orientational order). Since the initial discovery of LCs in 1888 liquid crystals have contributed to some of the greatest technological leaps. LCs have found a way into everyday life through Liquid Crystal Displays (LCDs) however their applications reach much further than just displays, including but not limited to light modulators, photonic band gap materials, smart windows and counterfeiting countermeasures on banknotes.^[3,4,5,6,7] Many different mesophases have been discovered and described, starting with simple nematic (N) phase where all molecules point in the same general direction described as the director, but with no positional order between themselves through more complicated smectic phases (Sm)

1.1 Liquid crystals

where the molecules not only point in the same direction but are also arranged in lamellar layers. Chiral nematic phase (N^*) is a special class of nematics where the preferred direction of the orientation changes throughout the sample forming a helix with a certain pitch. Chiral nematics are often interchangeably referred to as 'cholesterics' due to their original discovery being made in cholesterol derivatives. The helical structure formed allows for the unique ability of to selectively reflect one component of circularly polarised light. The chiral nematic LCs in particular are well known for their strong circular dichroism by selective reflection. Systems displaying N^* phases are frequently employed in thermochromic materials which change their appearance as a function of the temperature. This is due to the pitch of the helix changing and changing the wavelength of the light reflected.

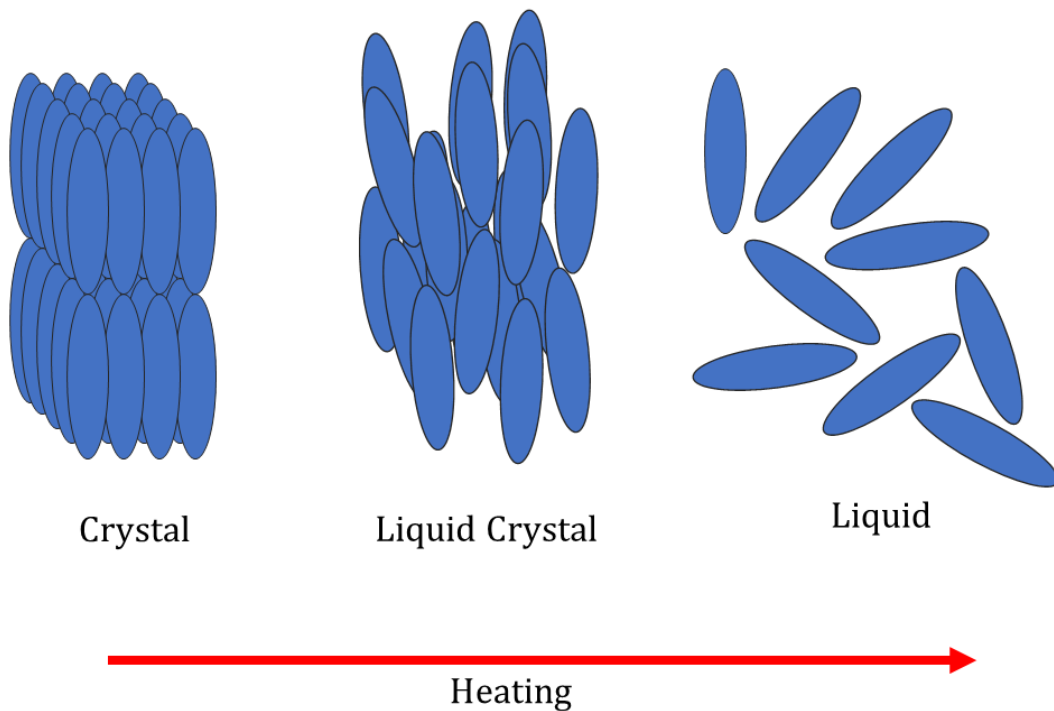


Figure 1.1: Schematic representation of a liquid crystalline phase found in between the crystalline and isotropic liquid phases.

LCs are particularly interesting as they display anisotropic properties usually

only observed in solids but also flow like liquids. The most obvious example is optical anisotropy where linearly polarised light is transmitted differently depending on the measurement angle. Dielectric anisotropy is another example of this where electric permittivity of the molecule is different depending on its orientation. LCs are usually studied in ‘cells’ which contain alignment layer. The alignment is predominantly either homeotropic or planar (also known as homogenous) and is induced by an alignment layer, usually a polyimide polymer. Liquid crystals are split into two main research areas: thermotropic and lyotropic. A thermotropic LC displays mesophases temperature of the sample is changed whereas a lyotropic LC mesophases are susceptible to change in the concentration of the solvents. Molecules which display both types of behaviour are rare and are described as amphotropic. The chemical structure of the mesogens has an important influence in its liquid crystalline properties. Within low molecular weight liquid crystals, these are predominantly split into two main groups: calamitics and discotics. Calamitic (also known as ‘rod like’) LCs are more prevalent in both literature and applications of liquid crystals, they usually possess a polarisable rigid core and a flexible chain. These usually form phases such as nematic, smectic and cholesteric phases (described in section below). The other type of low molecular weight LC is discotic. These are characterised by flat and ‘disk like’ centre group stabilised with aliphatic chains on the outer side of the discs. They tend to form discotic equivalent of nematic phase and stacked columnar phases analogous to smectic phases in calamitic molecules (Fig. 1.2).

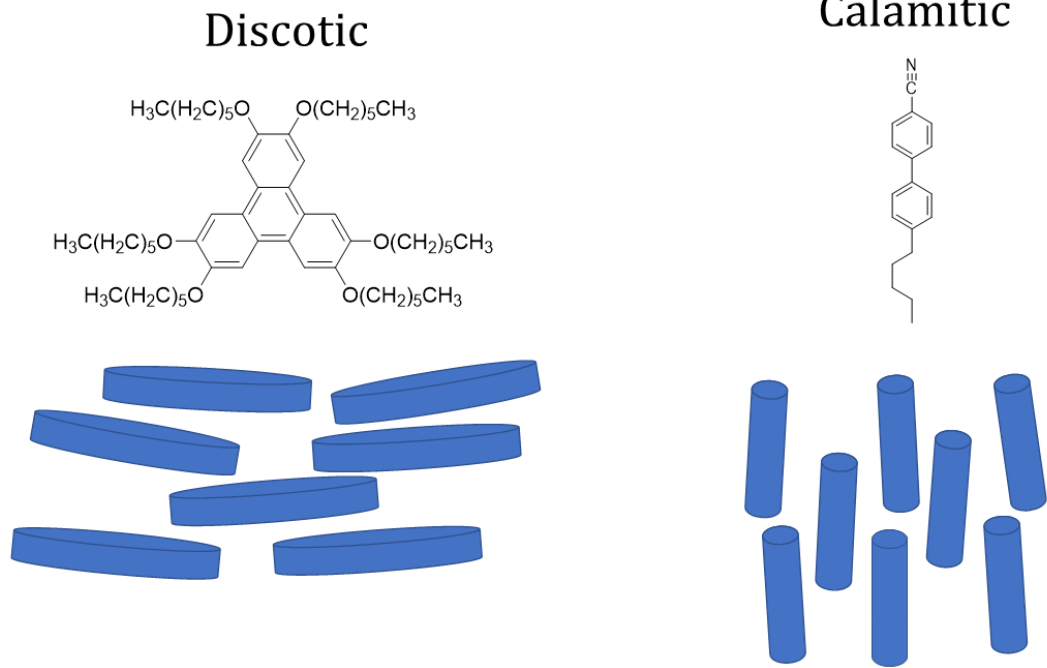


Figure 1.2: An example chemical structure of (a) Discotic and (b) Calamitic liquid crystals and their analogous nematic phases.

Currently, LCs remain an important field of research which brings together chemists, engineers, physicists and biologist alike.

1.2 Types of mesophases

A number of mesophases have been identified since the first discovery of liquid crystals. This section describes the ones that are relevant to this thesis.

Nematic phase

Nematic (N) phase is the most commonly observed and technologically relevant mesophase. Here the molecules self-assemble with long-range orientational order and no positional order, that is the centres of mass of the molecules are not correlated. [1.3](#)). In a nematic phase, the average orientation of the molecules

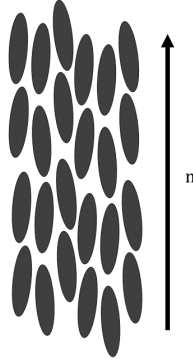


Figure 1.3: Schematic of a nematic liquid crystalline. The director (\mathbf{n}) describes average orientation of the anisotropic axis of the molecules.

with the director (\mathbf{n}) can be quantified using an orientational order parameter (\mathbf{S}) described by 2^{nd} order Legendre polynomial: $S = \frac{1}{2} \langle 3 \cos^2 \theta - 1 \rangle$ where θ represents the angle between the director and the individual molecular long axis. The value of the order parameter S depends on temperature and varies between $-\frac{1}{2} < S < 1$. In the isotropic phase, the order parameter is equal to zero as there is an equal probability of having the molecules in all directions and in a perfect crystal $S = 1$ as all the molecules are pointing in the same fixed direction. For a typical nematic phase, $S = 0.4 \rightarrow 0.8$ ^[8] A typical nematic phase is non-polar and therefore $n = -n$ and as such the two directions are indistinguishable.

Chiral nematic phase

Chiral nematic (N^*) phase is a mesophase most commonly observed for chiral liquid crystals or nematic materials with chiral dopants. A chiral molecule is a chemical molecule which possess a non-superimposable mirror image. It was first observed in cholesterol benzoate and soon after in other cholesterol derivatives. Because of this, the phase was first described as 'Cholesteric' phase however this name has since been supersede by chiral nematic. This phase posses long range orientational order similar to that seen in nematics however the director rotates throughout the sample resulting in formation of the helix. (Fig. 1.4)

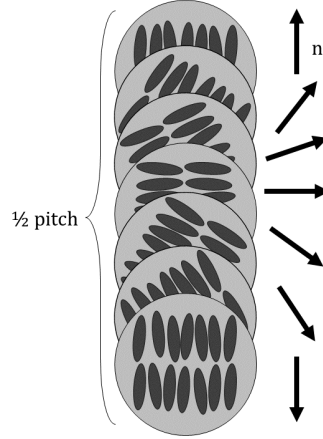


Figure 1.4: A half-pitch of a chiral nematic phase (180° twist). \mathbf{n} marks the director.

A full 360° rotation of the director is described as pitch (\mathbf{p}). The pitch is temperature dependent with higher temperatures resulting in shorter pitch. Typical pitch for chiral nematic materials is within hundredths of nanometers. It is possible for the pitch to match the visible light wavelengths. In this situation, shining white light onto the material results in the selective reflection of the light matching the pitch causing the sample to appear coloured. This relationship can be defined as

$$\lambda_p = \bar{n}p \quad (1.1)$$

where λ_p is the average peak reflected wavelength, \bar{n} is the mean refractive index and p is the pitch.^[9] N^* phase is usually found in compounds that are naturally chiral, often biological materials. However achiral mesogens can be doped with chiral dopants leading to formation of N^* over standard N phase. Here, the pitch can be controlled by the concentration of the chiral dopant and is given by:

$$p = \frac{1}{HTP \times c} \quad (1.2)$$

where HTP is the helical twisting power of the dopant and c is the concentration of the dopant as a fraction of the overall composition.

Smectic phase

The word 'smectic' is derived from the Greek word for cleanse as the smectic phase first observed in soaps. Unlike the nematic phase, smectic phases possess both orientational and positional order. There are many subtypes of the smectic phases but the most common ones are smectic A (SmA) and smectic C (SmC). In a SmA phase, the molecules are arranged in layers with definable spacing in between the layers. The director is perpendicular to the layer plane (Figure 1.5) and is parallel to the layer normal. In the SmC phase, the director is tilted away from the layer normal at an angle (θ) called the tilt angle.

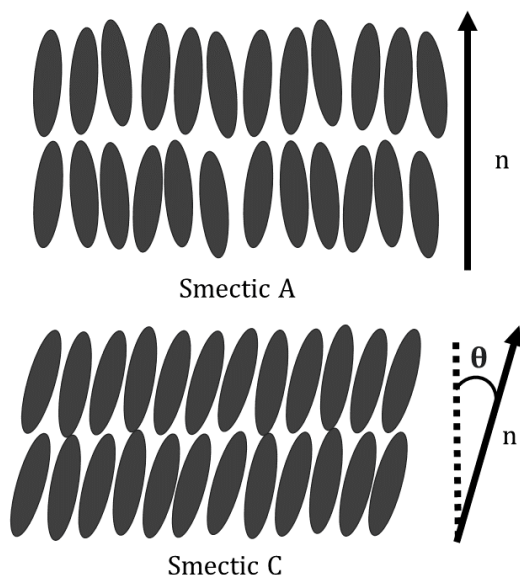


Figure 1.5: Smectic A (SmA) and Smectic C (SmC) phases. n is the director and θ is the tilt angle of smectic layer in reference to layer normal. In SmA phase, \mathbf{n} lies parallel to the layer normal where as in SmC \mathbf{n} lies at an angle to the layer normal.

1.3 Chemical structures of mesogens

Chemical structure of a liquid crystal molecules play a key role in their mesogenic properties. While the complete description of the impact of the chemical structure

1.3 Chemical structures of mesogens

on the mesogenic properties of the material are beyond the scope of this thesis, certain properties, in particular in the case of polymers, are important for the next chapters and will be described here.

Cyanobiphenyls

Cyanobiphenyls are the most common type of chemical studied and most commonly found in commercial applications of liquid crystals. They hold significant historical significance due to their usage in liquid-crystal displays (LCD). Their discovery in the 1970's led to a huge technological jump paving way for amongst other things, mobile phones, tablets and head-up displays. Cyanobiphenyls are an example of calamitic mesogens. The biphenyl ring provides the cylindrical symmetry to the rigid core. A polar group such as fluoride or nitrile is often found attached to the cyanobiphenyl core group to provide a dipole moment which can be exploited for to switch the liquid crystal under an external electric field (Figure 1.6)

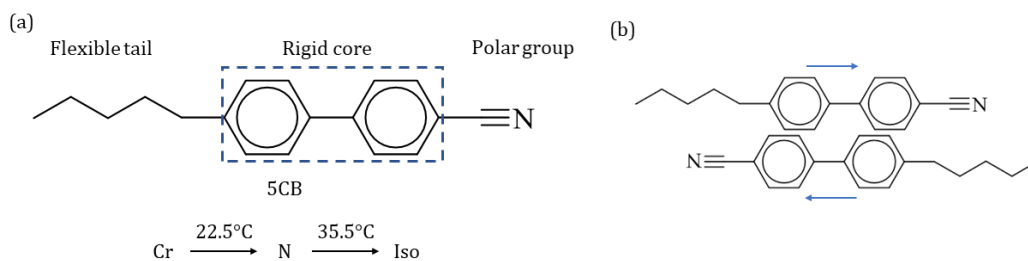


Figure 1.6: (a) Chemical structure of 4-Cyano-4'-pentylbiphenyl (5CB) liquid crystal molecule with the features contributing to its mesogenic properties highlighted. (b) Schematic diagram showing the antiparallel configuration of two 5CB molecules. The blue arrow indicates the direction of the permanent dipoles of each of the molecules.

One or more flexible tails are often found on calamitic mesogens as well. These increase entropy of the molecules preventing them from forming crystals and forming LC phases instead. The longer the hydrocarbon tail the more stable the nematic phase. This is due to the stabilising interaction between the tails

1.3 Chemical structures of mesogens

from different molecules. This however becomes unfavorable for the formation of the nematic phase as longer chains tend to suffer from excessive Van der Waals forces and lead to narrower stability of the nematic phase. CBs with longer chains also start to exhibit an odd-even effect where the molecules with odd-length of carbon in the tail higher T_{N-I} temperatures than even-length chains. This can be accounted for the deviation from the linear structure of the molecule where the structure would be in an *trans* configuration which would be more tightly packing. Another important aspect of the chain is the resulting phase formation, with the tendency of longer chains to form smectic phases and shorter chains to form nematic.

Cholesterol derived mesogens

As mentioned previously, one of the first discovered LCs was cholesterol-benzoate, a cholesterol derived ester. While cholesterol in itself is not liquid crystalline, a lot of its derivatives are, most commonly its esters. As cholesterol and its derivatives are inherently chiral, these compounds tend to form chiral nematic phase. Cholesterol is an example of a naturally occurring sterol. Cholesterol is found in every eukaryotic organism and as such is universally compatible with living matter. This makes it unique for applications within biomedicine e.g. in drug delivery or tissue scaffolds.^[10,11,12,13,14,15] Within literature, thousands of cholesterol based liquid crystals have been described.^[10,16,17,18,19,20,21,22,23,24,25,26,27,28,29,30]

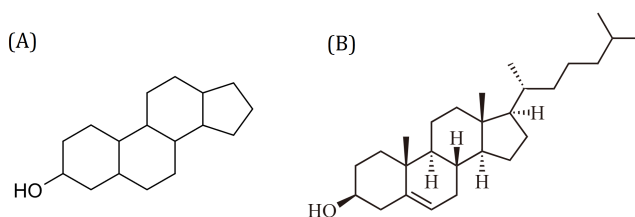


Figure 1.7: Chemical structure of (a) typical sterol and (b) cholesterol.

1.4 Polymers

Polymers are a class of macromolecules formed by many repeating units, usually referred to as monomers. Since the preparation of the first synthetic polymer in 1907, polymer science has expanded into one of the largest fields of research in history with 7 Nobel prizes awarded on research in the field. Approximately 300 tons of plastic is manufactured each year making them one of the most ubiquitous substances on earth. Their applications vary from generic storage containers to life-saving medical devices. One academically and industrially relevant area of polymers are liquid crystal polymers. These have found applications for sensors and security devices on small scale and within the defense market with polymers such as Kevlar being used for bulletproof vests. The importance of this class of molecules in the modern world cannot be understated.

1.4.1 Copolymers

Copolymers is a wide subgroup of polymers which consists of two or more different types of monomers coming together and forming a macromolecule. A significant part of the thesis will be devoted to block copolymers.

1.4.2 Block copolymers

Block copolymers (BCPs) are polymers consisting of two or more homopolymers joined together by covalent bonds (Figure 1.8). These types of polymers are specific class of molecules where two otherwise incompatible chemical species are brought into close contact but are unable to separate from each other due to the covalent bond linking the blocks. This type of behaviour leads to microphase separation which controls over the self-assembly of the molecules. The spatial resolution of the separation can be controlled by the chain lengths of each of the blocks. This sort of behaviour can be observed in bulk and in concentrated solutions as well as in thin films.

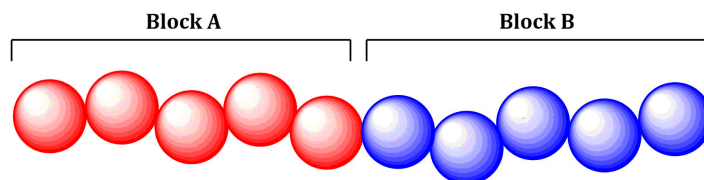


Figure 1.8: Example of a block copolymer structure.

Historically, these macromolecules were first described within literature in the 1950's for their improved surfactant abilities under the commercial name of "Pluronic". It was after the discovery and popularisation of living anionic polymerisation that the interest in block copolymers had skyrocketed due to availability of large scale controlled synthesis for niche applications such as concrete additives and templating agents for mesoporous structures.^[31]

1.4.3 Liquid crystalline polymers

Liquid Crystalline Polymers (LCPs) are polymers that contain mesogenic groups. There are two main types of LCPs, main chain LCPs (MCLCPs) and side chain LCPs (SCLCPs) (Figure 1.9). Whilst the actual mesogenic groups in LCPs is chemically similar to the ones found in low molecular weight liquid crystals (LMWLCs), additional factors need to be considered. Degree of polymerisation (DP) plays a role in the transition temperatures of the mesophases in the polymer however after a critical DP, the effect levels off. The degree of polymerisation can be defined as the ratio of number-average molecular weight (M_n) over the molecular weight of the monomer unit (M_0)

$$DP = \frac{M_n}{M_0} \quad (1.3)$$

Certain phases are also only observed only in certain N ranges, mostly in the lower range of N of between 5 and 50 units in length. Additionally, certain mesophases can only be observed in polymer samples with very narrow polydispersity (PD). Polydispersity (PD) is a measure of dispersity of molecular mass in a particular polymer sample. Its defined as

$$PD = M_w/M_n \quad (1.4)$$

where M_W is the average molecular weight and M_n is the number average molecular weight. In synthetic polymers, it is usually said that polymer samples with $PD < 1.1$ are monodisperse. Incorporation of a mesogen into a polymer results in formation of higher phases in polymer compared to those observed in the mesogen itself, e.g. an unpolymerised monomer might produce Smectic structures and the polymerised molecule produce a lower ordered phases such as nematic or not form any liquid-crystalline phase. This is usually referred to as the polymer effect.^[32]

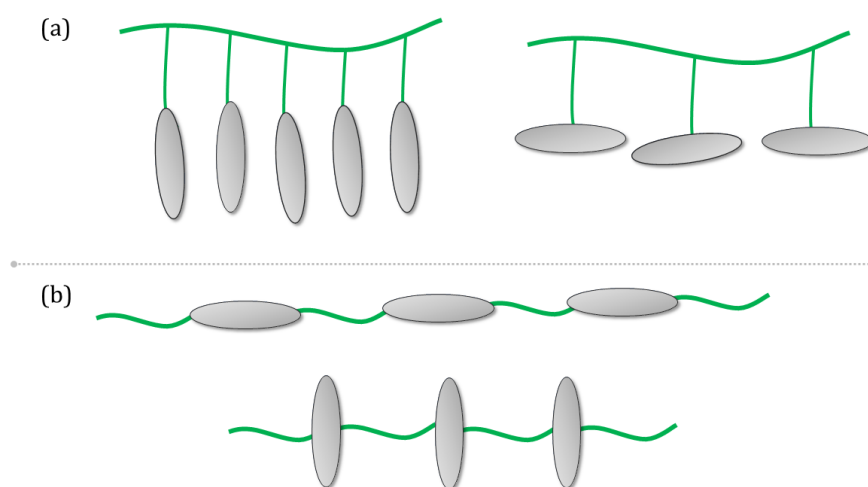


Figure 1.9: Example of liquid crystalline polymers. (a) side chain polymers (b) main chain polymers. The ovals represent the mesogenic groups. The green lines correspond to the chemical linkage between the mesogenic groups.

The polymer backbone plays an important role in the LCBCP system, while it does not have a major influence on the mesophases formed it does however influence the transition temperatures and the mesophase range. This is a result of the difference in stiffness between the backbones, with softer backbones (e.g. acrylate and siloxane) giving lower transition temperatures of both the glass transition (T_g) and increasing the ΔT (the temperature range of the mesophase, $T_{CI} - T_g$). However, this does not necessarily mean that the clearing temperature changes. Another factor which has an impact on the phase transitions as well as the phases formed is the length of the spacer between the polymer backbone and

the mesogenic group. The spacer group decouples the motion of the mesogens from the polymer backbone. Increasing the length of the spacer group decreases viscosity of LC and isotropic phases and tends to improve switching properties. The most common types of spacers used are oligomethylene, usually between 2 and 13 units long however oxyethylene^[33,34] and siloxane^[35,36] spacers are also frequently used. An odd-even effect is also present in the spacer groups, where even number of carbons in the spacer results in higher transition temperatures, for both the mesophases as well as T_{CI} . Usually the linker is attached to the mesogen head-on, however it is possible to have a lateral connection attached to the mesogen through its long axis. Laterally attached mesogens in polymers are often referred to as ‘mesogen jacketed’ polymers.

1.4.4 Perfluorinated LC polymers

Chapter 4 describes, the self-assembly behaviour of perfluorinated block copolymers bearing a liquid crystalline group. Conventional block copolymers such as polystyrene-block-poly(methyl methacrylate) (PS-b-PMMA) do not possess a sufficiently high Flory - Huggins interaction parameter (χ) in order to reliably produce feature sizes in the sub-10nm region. Block copolymers bearing perfluorinated side groups on the other hand result in polymers with exceptionally high Flory - Huggins interaction parameter. On top of that, perfluorinated side groups tend to lead to liquid crystalline properties within the resulting polymers. The liquid crystalline properties can then be exploited for further modifications of the self-assembled structures. Chapter 6 demonstrates some of the self-assembling nature of these polymers, both in thin films and within the context of polymerisation-induced self-assembly (PISA). Polymers bearing semifluorinated polymethacrylates are a well known class of LC macromolecules. These can form smectic phases in thin films^[37,38,39] and in bulk.^[40] Polymers containing perfluorinated side groups have a strong tendency to show LC order, due to their rigidity and ability to tightly pack compared to their alkene equivalents. However, analogues to many fluorinated materials, they tend to be insoluble in most common solvents. Hue et al. described a process where the 2-(perfluorooctyl)

ethyl methacrylate (FOEMA) was polymerised as a third block in the presence of poly(N,N-dimethylaminoethyl methacrylate)- b-poly(benzyl methacrylate) (PDMA-b-PBzMA) 'seeds'. and the resulting structures included spheroids, ellipsoids, cylinders and spherical multi-compartment micelles (MCMs).^[41] Li et al. demonstrated preferential assembly of ellipsoidal nanoparticles fusing head-on-head to form nanotubes.^[42] It has been demonstrated that liquid crystalline order (in particular, smectic phases) lead to ellipsoidal^[38] and various faceted^[43] morphologies, both difficult to achieve with standard PISA.

1.4.5 Cholesterol-based LC polymers

Preparation of chiral block copolymers remains elusive. While chiral nematic phase can be found within the system containing BCPs, systems containing only pure BCPs and forming chiral nematic phases are yet to be documented. Such systems could theoretically be used for precise biocompatible sensors and responsive drug-delivery vehicles when combined with the self-assembling properties of BCPs. As such, in Chapter 5 an experimental attempt is made to prepare such macromolecules. Though the N* phase observed back in 1888 was in low molecular weight liquid crystals (LMWLC) it was hypothesised that this phase could be observed in polymers or other higher-molecular weight liquid crystals (HMWLCs). Early work on liquid crystalline polymers forming N* phase was performed with cholesterol and its derivatives. N* phase forms for chiral molecules as the chirality provides a driving force for the formation of the helix.^[16] The resulting polymers however, did not form the N* phase, unlike their corresponding monomers, instead they formed higher ordered smectic phases.^[44,45] In 1978, Finkelmann et al., prepared the first enantiotropic cholesteric polymer by polymerising mixtures of cholesterol-based monomers with short and long spacers.^[46] Expanding on their earlier work of liquid crystalline polymer synthesis, Finkelmann then proceeded to develop a polymer series with N* phase moving on to describe the first polymer with biaxial N* phase.^[47] The key step in this process was decoupling the motion of the polymer backbone from the mesogenic group via a 'spacer' group in between the two. Work by Shibaev in 1979 showed an ambiguous phase formation in methacrylic copolymers bearing cholesterol and

butylmethacrylate.^[17] While they displayed textures and selective reflection similar to those observed in a N* phase in LMWLCs in bulk, these textures were not observed in thin films. In thin film they instead showed textures similar to those of standard smectics.

Another example of polymer forming higher order structures compared to the corresponding monomers was observed by Xu et al.^[48]. They found that the N* phase was only observed in monomers but not in polymers bearing the same mesogen. The polymers instead formed a smectic A (SmA) phase due to limited flexibility of the backbone and spacer units hindering the formation of the helix of the N* phase. Homopolymers bearing side-chain cholesteryl mesogens tend to form smectic phases (predominantly SmA) over a wide range of temperatures with only a selected few showing both chiral nematic and smectic phases.^[49] Finkelmann et al., prepared an enantiotropic liquid crystalline polymer with a N* phase by mixing different equal parts monomers with short spacers and longer spacers based on alkylbenzene ester.^[50] Whilst this was not a homopolymer, it paved a way for a better understanding of the influence of the spacer group on the resulting mesophases. The influence of the spacer on the properties of the polymer was further demonstrated by Hu et al^[51] where they showed that longer spacer length lead to lower phase transition temperatures and wider LC temperature ranges in polymers bearing cholesteryl side groups. The selective reflection of the polymers was also shown to blue shift as the spacer lengths was increased or the rigidity of the mesogens decreased. This was further explored by Yang et al who showed that the degree of polymerisation does not have a significant effect on the polymers without flexible spacers and with stiffer methacrylic backbone.^[52] It does however, has an effect on the more flexible acrylic backbone where the LC behaviour is observed only upon passing a critical threshold of molecular weight of $12 \times 10^3 \text{ g}\cdot\text{mol}^{-1}$. By switching the spacer from an ether to an equivalent ester, Yang et al demonstrated that the transition temperature to the N* mesophase shifted from -27°C in the ether linker to 72°C in the analogous ester case whilst having little impact on the clearing temperature (Figure 1.10).^[52]

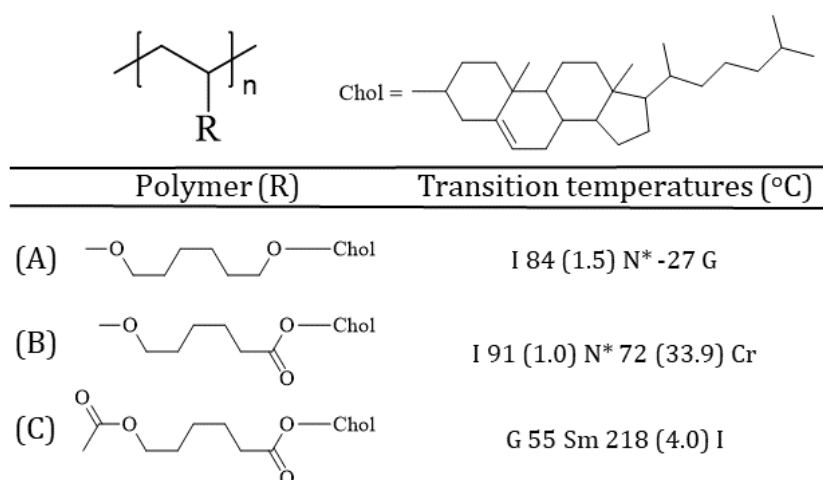


Figure 1.10: An example of the influence of chemical differences in the spacer connecting the backbone and the cholesteryl mesogen, on the liquid crystallinity of the material. The introduction of each of the ester groups (A–C) gradually increases the relative stiffness of the backbone. N*—chiral nematic, I— isotropic, G—glass, Cr—crystal and Sm—smectic.

This switching of the spacer from an ether to an equivalent ester prompted the polymer to display crystallisation rather than a glass transition. A much more dramatic change was observed when the linker second ether group was replaced with another ester group. In this example, the polymer only displayed monotropic transitions and no N* phase was observed. For the N* phase to form, the spacer length had to be increased to $n = 10$. This arises from the relative stiffness of the C=O bond compared to C-O, which hinders the freedom of the mesogen to order itself. Klok et al., showed that covalent incorporation of cholesterol moiety to a low-molecular weight L-lactic acid oligomers resulted in formation of thermotropic liquid crystal smectic phases.^[53] While the mesogen was a small part of the overall molecule, its strong tendency to form the mesophase was expressed in the larger molecule.

1.5 Polymer synthesis

1.5.1 Reversible Deactivation Radical Polymerisation (RDRP)

Reversible Deactivation Radical Polymerisation (RDRP) is a IUPAC term for polymerisation reactions referred to as controlled radical polymerisation (CRP). In general, the techniques involve an equilibrium between active (or 'living') and dormant polymer chains, allowing for a control over the desired molecular weight of polymers with narrow polydispersity (PD). It offers advantages over standard free radical polymerisation (FRP) such as targeting the desired degree of polymerisation and narrow PD. RDRP commonly involves usage of a chain-transfer agent which facilitates the formation of the reaction equilibrium. It also enables preparation of polymers with complex architectures otherwise inaccessible with FRP. While there are many types of RDRP reactions including atom transfer radical polymerisation (ATRP) or nitroxide-mediated polymerisation (NMP), this thesis will focus on Reversible addition-fragmentation chain-transfer polymerization (RAFT) as it is the most well established method for applications within polymerisation-induced self-assembly and works well with acrylic and methacrylic monomers used throughout this thesis.

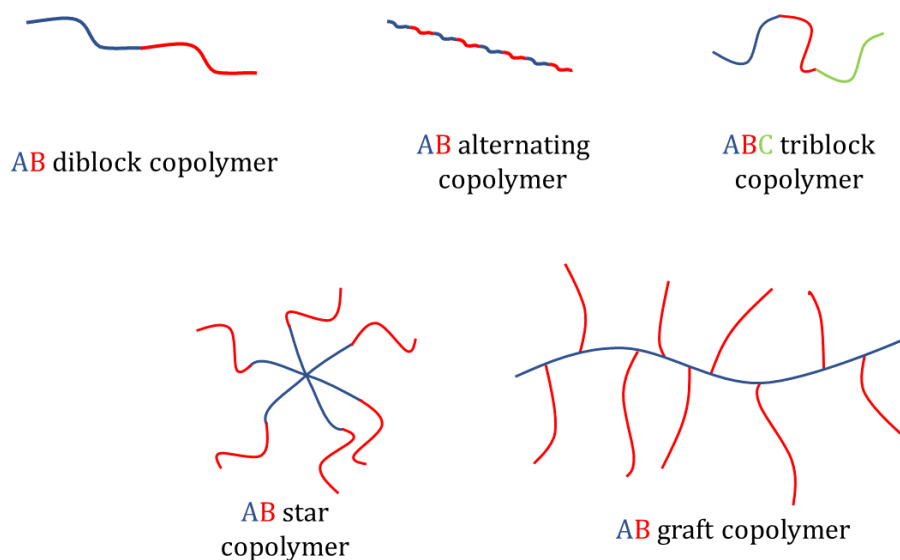


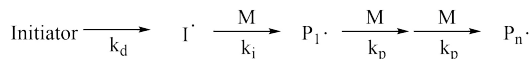
Figure 1.11: Examples of architectures of copolymers which can be synthesised by Reversible Deactivation Radical Polymerisation (RDRP) methods.

1.5.2 Reversible addition-fragmentation chain-transfer polymerization (RAFT)

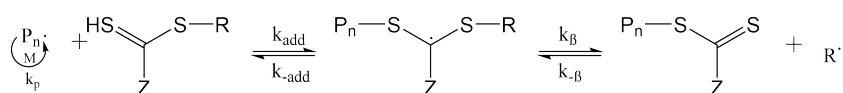
RAFT polymerisation is a type of living radical polymerisation that has been extensively used since its discovery in 1998 as a reliable way of preparing polymers with very narrow polydispersity, high end-group fidelity and predictable molecular weights.^[54,55] This is due to the unique chemical mechanism RAFT follows. A chain transfer agent (CTA), usually dithioesters molecule with two groups, R and Z is required. The R and Z group stabilise both the radical intermediate and the propagating chain and can be fine-tuned to specific systems. The narrow PD is also result of the mechanism of RAFT where the rate of propagation is less than the rate of activation of the living polymer chain, i.e. there is less than one monomer added per activation cycle. Other usual considerations as with standard free radical polymerisation remain, including choice and concentration of initiator, degassing and solvent choice.

1.6 Self-assembly of block copolymers in thin films

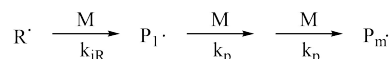
Step 1: Initiation



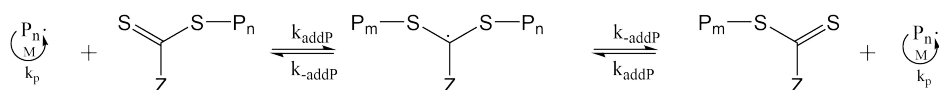
Step 2: Pre-equilibrium



Step 3: Reinitiation



Step 4: Main equilibrium



Step 5: Termination

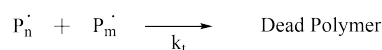


Figure 1.12: Mechanism of Reversible addition-fragmentation chain-transfer (RAFT) polymerisation. Step 1 - A source of free-radicals such as an initiator starts the reaction by forming available radical species. Step 2 - The radical monomer reacts with the RAFT agent forming an early polymer. Step 3 - The leaving group radical reacts with another monomer to form another active chain. Step 4 - The main equilibrium of the RAFT reaction where the present radicals propagate chain growth where the rate of the chain growth is controlled by the available radicals leading to narrow PD in the resulting polymers. Step 5 - Two alive chains undergo a bi-radical termination leading to a 'dead' chain which can not react further.

1.6 Self-assembly of block copolymers in thin films

As microphase separation in thin films takes place on a molecular scale, with the domain sizes of 5-50nm, it was identified as a very powerful way of controlling nanoscale patterning. A domain size this small is difficult or expensive to produce

1.6 Self-assembly of block copolymers in thin films

using conventional lithographic methods. In particular, linear BCPs are known to exhibit lamellar and cylindrical structures which are of high importance for nanoscale patterning (Figure 1.13).

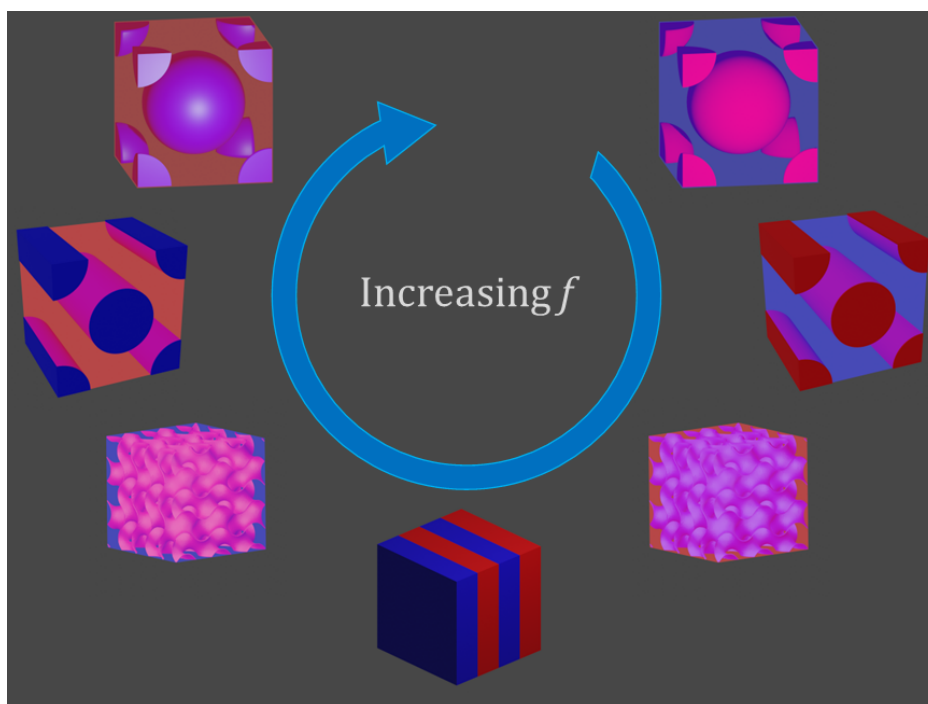


Figure 1.13: Examples of structures formed by the self-assembly mechanism in block copolymers. The f in the block corresponds to the volume fraction of one of the blocks.

Factors which play a role in the self-assembly include the degree of polymerization (N), relative volume fraction of the blocks and the segregation strength. However, in thin films, other factors such as air-polymer and polymer-substrate interactions also have to be considered. The segregation strength is described as a function of Flory-Huggins interaction parameter (χ) and the degree of polymerization (Figure 1.14).

1.7 Polymerisation-induced self-assembly

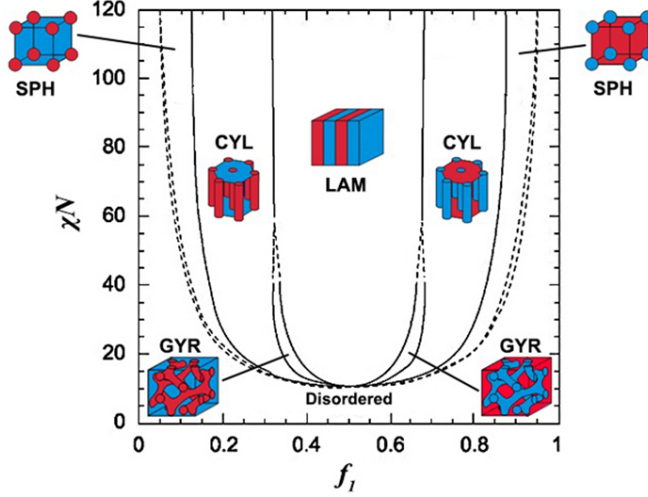


Figure 1.14: Theoretical phase diagram of diblock copolymer melts calculated by the mean-field theory SCFT. χ is interaction parameter, N is the total number of segments, f_a is the volume fraction of block a . The phases are denoted as SPH (spherical), CYL (cylindrical), LAM (lamellar), GYR (gyroid), and DIS (disordered).^[1]

Flory-Huggins interaction parameter (χ) is a thermodynamic description of the free-energy cost, in units of $k_B T$, per monomer unit in a block copolymer.

$$\chi = \frac{Z}{k_B T} \left[\varepsilon_{AB} - \frac{1}{2}(\varepsilon_{AA} + \varepsilon_{BB}) \right] \quad (1.5)$$

Positive χ indicates net repulsion between the blocks and negative χ means free-energy drive towards mixing. It's important to note that the χ is inversely proportional to temperature meaning the mixing is more likely at high temperatures. Strong specific interactions such as hydrogen bonding or charges lead to negative χ parameter so in order to prepare a strongly separating block copolymers it is important to take these criteria into considerations.

1.7 Polymerisation-induced self-assembly

Polymerisation induced self-assembly (PISA) is a technique of preparing polymer assemblies where the polymerisation and self-assembly take place simultaneously

1.7 Polymerisation-induced self-assembly

in situ (Figure 1.15). This method produces highly monodisperse particles with tuneable morphologies including spherical, worm-like and faceted micelles as well as vesicles (Figure 1.16). PISA requires a solvent miscible second block monomer but a solvent immiscible block copolymer. This results in formation of a well-defined nanoparticles which, with the right solvent, form colloidal suspensions. Variables such as degree of polymerisation (N), final solids weight fraction, polydispersity (DP) and the solvent have an impact on the final structure of the nanoparticles. Whilst the self-assembly of block copolymers into ordered nanostructures is not novel, it is usually performed as a post reaction step requiring extra steps. PISA offers a quick way of preparing those in situ avoiding costly and time-consuming experimental steps.

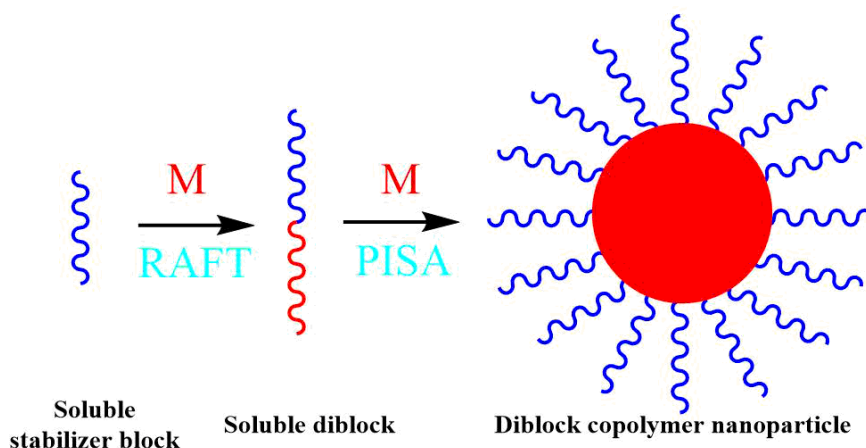


Figure 1.15: Schematic representation of the self-assembly process in polymerisation-induced self-assembly (PISA).

While PISA with groups bearing LC mesogens is a relatively under-explored area of research as a whole, it was in fact reported in one of the earliest known PISA papers by Zhang et al.,^[56] who polymerised CholA monomer ion in the presence of a P(AA-co-PEGA) macromolecular chain transfer agent in an ethanol/water (95:5) solvent to produce poly(acrylic acid-co-poly(ethylene glycol) monomethyl ether acrylate)-b-poly(cholesteryl acryloyloxyethyl carbonate). The result was a dispersion of nanocylinders^[56] with internal smectic-type order over a broad range of solid concentrations and relative block ratios. The radius of the nanocylinders

1.7 Polymerisation-induced self-assembly

increased as a function of the chain length of the hydrophobic block. In this case, the LC order was assumed to play a significant role in the assembly formation alongside the traditional driving forces. The study showed that the LC order was preserved and introduction of it to the system lead to the preferential formation of nanofibers over vesicles observed in an equivalent polystyrene system. An advantage observed upon introduction of a LC group was the reduction of the polymer dispersity (\mathfrak{D}) with higher LC content. Whilst few PISA studies have been performed with steroid-based monomers, the field is starting to gain traction with recent publications focused on the introduction of perfluorinated LC monomers^[38,42,43,57,58,59], biphenyls^[60] and azobenzenes^[61,62,63]. The structures seen within these systems show unique properties such as physical rearrangements upon thermal stimuli. Analogous to systems mentioned earlier, the linker length plays an important role in determining the resulting PISA morphology with a biphenyl mesogen providing insights into the mechanism underpinning the impact of LC groups within PISA.^[60] Longer linkers lead to slower polymerisation kinetics and only the longest (C=11) displayed direct liquid crystalline behaviour with smectic order in the nanorods.

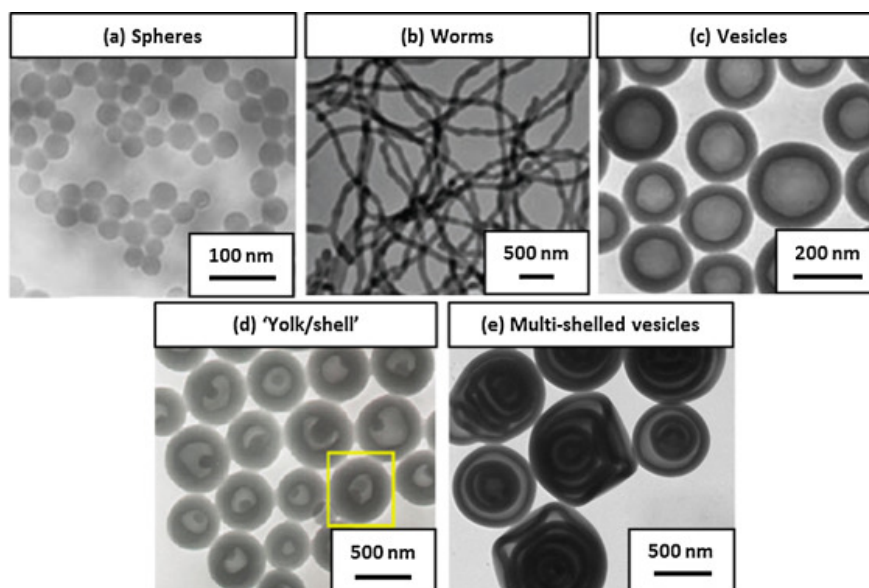


Figure 1.16: Example of complex nanostructures of P2VA obtained via PISA (a) spheres, (b) worms, (c) vesicles, (d) ‘yolk/shell’ and (e) multi-shelled vesicles. Reproduced with permission from^[2]

1.8 Aims and motivation

The central goal for this thesis was to further the understanding of the the influence of liquid crystalline groups on the self-assembly of block copolymers. In particular, the focus was payed on polymerisation-induced self-assembly (PISA) and self-assembly in thin-films.

PISA is a relatively young method however it has already proven to be a significant improvement over previous types of preparing self-assembled structures of BCPs.^[64] Introduction of a liquid crystalline monomers into its arsenal further establishes it as a reliable and potent method for preparation of even more elaborate and responsive nanostructures with potential applications within many field such as drug delivery, sensors and nanoelectronics.

Introducing of liquid crystalline components into a self-assembling system can be exploited to offer further means of controlling the said self-assembly. As such, introducing liquid crystallinity into amphiphilic block copolymers opens new avenues for formation of novel and otherwise inaccessible structures and motives.

The aims of this work undertaken in this thesis was to improve the understanding of the following:

1. To further explain what role liquid crystalline order plays in polymerisation-induced self-assembly of block copolymers.
2. To characterise the self-assembly of block copolymers bearing liquid crystalline side groups in thin films as well as their potential applications for optical or similar liquid crystalline devices.

In order to achieve this, a study of liquid crystalline block copolymer established in literature was furthered by expanding on the knowledge of its fusion mechanism and explaining the role the LC behaviour plays on its self assembly.

Further to this, preparation of a set of novel block copolymers not described in literature was performed. By synthesising custom monomers and combining their unique LC properties to obtain PISA structures with unique morphologies.

1.9 Thesis outline

The thesis is split into 6 chapters. Chapter 1 introduces the key concepts and their fundamentals. Chapter 2 describes the experimental methods and techniques used to obtain data and characterise the materials prepared.

Chapter 3 is a chapter that involves significant amount of organic synthesis in order to prepare custom liquid crystalline monomers bearing cyanobiphenyl and cholesteryl side groups and their subsequent self-assembly in PISA as described in Chapter 5.

Results of the experimental work are split into three chapters. Chapter 4 describes the the polymerisation-induced self-assembly (PISA) of block copolymers bearing mesogenic fluorinated side groups. It focuses on characterisation of the liquid crystalline character of the formed structures and the morphological evolution of the structures formed as a function of the degree of polymerisation of the mesogenic block.

Chapter 5 describes the synthesis of polymers bearing cholesterol and cyanobiphenyl mesogens as well as their liquid crystalline properties. It also covers the liquid crystalline properties of the individual monomers used.

Chapter 6 covers the attempts made to prepare self-assembled thin films and the features measured using atomic force microscopy.

Finally, Chapter 7 summarise the results from all of the other chapters and concludes the thesis and the impact it made.

The appendix will include useful bits of code used for data analysis as well as plots of data used which were not needed in their corresponding chapters yet provide useful glimpse into their corresponding materials.

Bibliography for all of the chapters was included at the end of the thesis.

Chapter 2

Experimental methods

Experimental methods and techniques used throughout the project during materials synthesis and characterisation are described in this chapter. This includes fabrication of liquid crystal devices, structural and optical characterization of liquid crystalline phases

2.1 Liquid crystal sandwich devices

Liquid crystals (LCs) possess long range orientational and often positional order however without controlling the alignment of the director and thickness of the sample it is difficult to fully characterise them. In order to obtain a better control over these features, sandwich LC devices are used. For experiments mentioned in this thesis, both commercial cells (AWAT) and custom made devices/cells were used. The commercial devices were obtained from the Military University of Technology, Warsaw, Poland.

2.1.1 Standard liquid crystal device

A typical liquid crystal device prepared is shown in Figure 2.2. This device consisted glass substrate as glass does not significantly affect optical properties of the device while being robust. An alignment layer was used to control the alignment of the liquid crystals. Different polyimides are used to afford either planar or homeotropic alignment. These can have different pretilt values and

2.1 Liquid crystal sandwich devices

other properties which affect the end result of the alignment. A spacer film or spacer beads are used to control the thickness of the device.

The prepared device is then filled in with the liquid crystal through capillary action and sealed with glue at the open ends where LC was applied.

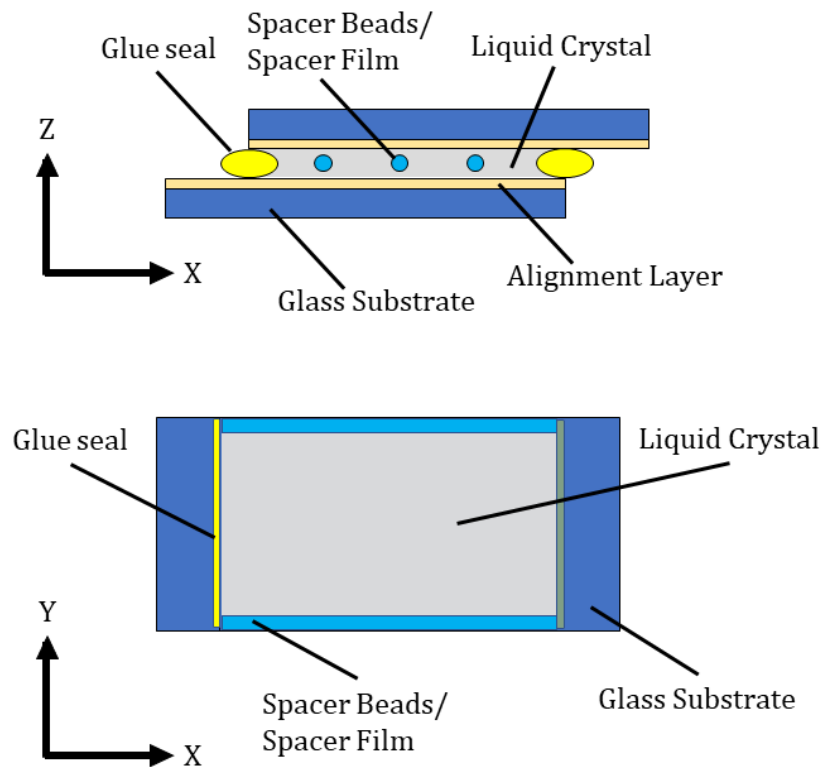


Figure 2.1: (a) Side view of a typical LC sandwich device. (b) Top view of the same device.

2.1.2 Fabrication process

The fabrication of the LC sandwich devices is a multi step process. This section will cover it from the beginning i.e. cutting the glass to the finished product. This process was performed within a clean room to avoid accidental contamination with dust and other debris which might be found in a standard laboratory.

Cutting the glass

In order to prepare sufficiently large cells, glass was cut using a glass scorer. A typical device would use either square or rectangular glass pieces, usually between 1cm and 2cm in width. For typical glass cells, standard microscopy grade glass was used. If a cell was to be used with application of an electric field, glass coated with indium tin oxide (ITO) as it conducts electricity allowing soldering of wires on. Once the glass was scored, the glass was snapped clean by applying a small amount of force to the other side of where the glass was scored.

Cleaning of the glass

The cleaning of the glass was performed by multiple washes with organic solvents and sonication for an extended period of time. A standard procedure was performed as follows:

- 30 minutes sonication in deionised water with 10% decon-90 surfactant followed by drying with compressed air
- 30 minutes sonication in deionised water followed by drying with compressed air
- 30 minutes sonication in methanol followed by drying with compressed air
- 30 minutes sonication in isopropyl alcohol

At this point the clean glass parts were kept in the solvent until needed at which point they were dried with compressed air in clean room in order to avoid contamination from debris in the air.

Alignment layer deposition

In order for the liquid crystals to be aligned within the finish cell in a controlled manner, an alignment layer (referred to as polyimide layer (PI)) had to be deposited and baked onto the glass substrates. The PI layer aligns the LC through weak Van der Waals and steric interactions between the polymer and mesogens. The PI layer has to be of uniform thickness and coat the entire surface of the

2.1 Liquid crystal sandwich devices



Figure 2.2: Clean room in the Sir William Henry Bragg Building. The gold light is used to ensure photosensitive samples are not exposed to light.

Table 2.1: Different polyimides used for the alignment of LCs.

Alignment PI	Alignment Type
SE3510	Planar
SE1211	Homeotropic

glass in order to be effective. This was achieved by using a WS-650-MZ spin coater at 3000rpm for 60s. The type of PI used controlled the alignment of the LCs.^[65] This is briefly summarised in Table 2.1. The PIs had to be developed in order to ensure they bonded to the glass and no residual solvent remained. This was done on a hotplate at 180°C for up to 120 minutes.

For planar cells, the samples had to be rubbed with a velvet cloth in order to give the alignment directionality. In order to ensure consistency between batches of cells, a mechanical rubbing machine using the same custom build software rubbing preset for each sample was used. The preset can be summarised as 20sec rubbing at constant speed and pressure done back and forwards 2 times total.

Spacer film deposition and gluing

The spacer film used was cut to the length of the cell with a width of approx. 0.1cm. The film was then placed on each side of the glass cell. The other side of the glass was then placed on top and glue was deposited on the sides of the

2.1 Liquid crystal sandwich devices

cells where the film was. In order to ensure good contact and uniform thickness of the cell a constant pressure was applied to the cell. This was usually achieved by either placing bulldog clips to the cell or by placing the cells in a vacuum bag and extracting all the air. After this step, the glue cured under UV light. The samples were cured for 30minutes under a UV source with the constant pressure applied to them throughout the procedure.

Cell gap measurements

The way the device cell gap was measured was by measuring the interference pattern of the empty cell with a UV/Vis spectrometer connected to a reflection microscope. After calibrating the UV/Vis spectrometer with a black background and a mirror, the cell was placed in the optical path of the microscope. The conditions for constructive and destructive interference are give by Equation 2.1 and Equation 2.2 interference respectively.

$$n\lambda = 2d \quad (2.1)$$

$$(n + \frac{1}{2})\lambda = 2d \quad (2.2)$$

Here n is an integer. This results in the spectrum appearing as a series of peaks and troughs corresponding to constructive and destructive interference. The distance between the maxima of the peaks is related to the device spacing (d) by Equation 2.3

$$d = \frac{\lambda_1\lambda_2}{2(\lambda_1 - \lambda_2)} \quad (2.3)$$

As the distance between peaks remains constant as long as the d spacing does not change, to get a more accurate value of d multiple distances of spacing can be taken as an average over the number of peaks measured (Equation 2.4).

$$d = \frac{\lambda_1\lambda_m m}{2(\lambda_1 - \lambda_m)} \quad (2.4)$$

Here m is equal to the number of peaks measured.

Filling and sealing the cell

The final steps before the filled cell is ready to use is to fill the cell with the material and seal with glue. The cells were filled using capillary action by placing the cells on a hotstage set to a temperature where the sample was liquid and placing a small amount of the material at the opening of the cell. The sample is then left at the temperature until the material has moved into the device through capillary action. Once the cell is full, the open sides of the cell are glued with UV glue. Once the glue is cured, the cell is ready to use.

2.2 Characterisation of materials

2.2.1 Polarised Optical Microscopy (POM)

A beam of light consists of individual photons which possess a vibrational component perpendicular to the path of the photon. When there is no favored direction of the vibrations, the light is said to be unpolarised. Polarised light on the other hand, resonates only within one particular plane. Polarised Optical Microscopy (POM) is one of the most fundamental techniques employed within the field of liquid crystals (LCs). It allows for the differentiation of isotropic and anisotropic materials and within liquid crystals in particular, it often helps identify mesophases formed and the transition temperatures associated with them. It works by exploiting optical anisotropy, also known as birefringence within LCs where the material possesses two different refractive indexes (Figure 2.3(a)). The birefringence of the material can be described in terms of the phase difference, given by

$$\Gamma = \frac{2\pi}{\lambda} \Delta n d \quad (2.5)$$

where λ is the wavelength of light, Δn is the birefringence and d is the thickness of the material. This is observed by setting the polariser and analyser filters set at 90° to each other and having the light pass through the LC sample on the stage. As the light passes through the material, it becomes elliptically polarised due to the birefringence (Figure 2.3(a)) For materials that do not exhibit birefringent LC phase, the transition from solid to liquid results in an isotropic liquid and appears

2.2 Characterisation of materials

completely dark under POM as no light is polarised in the correct orientation in relation to the analyser. Elliptically polarised light consists of two linearly polarised lights similar to circularly polarised light however the light amplitudes are different while maintaining a the same frequency. This results in a light wave where the electric vectors which rotates as well as changing its amplitude. Figure 2.4 shows an example of an oily streak texture observed under POM of a chiral nematic compound.

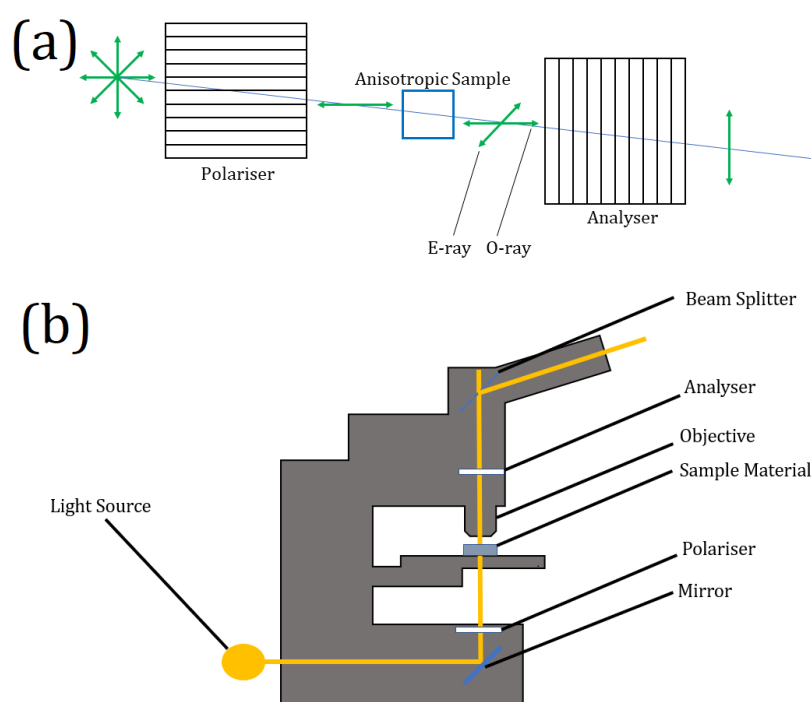


Figure 2.3: (a) Schematic of unpolarised light passing through the polariser becomes linearly polarised, which when passes through the birefringent sample becomes elliptically polarised. (b) Diagram of polarised light microscope setup in transmission mode. The light passing through the liquid crystalline sample material leads changes the lights polarisation from linear to ellipsoidal which is then passed through the analyser and into the detector (i.e. camera) and eye pieces.

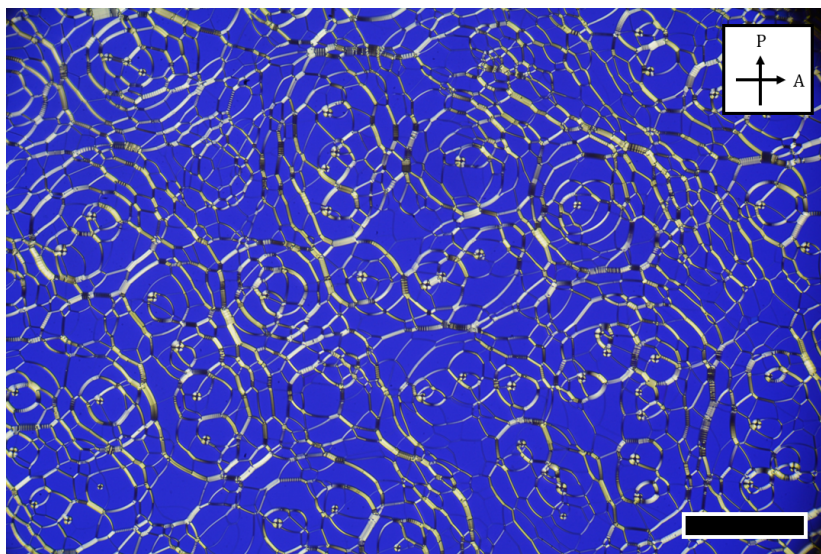


Figure 2.4: Oily streak texture of a chiral nematic material observed under POM at 20x magnification, reflection mode at 40°C. Arrows indicate the directions of polariser (P) and analyser (A). Scale bar = 1 μ m.

In order to identify phase transitions within the LC material, a temperature hot stage was used. Linkam T95-PE temperature controller and Linkam THMS-600 hotstage were used for materials that do not require cooling to below ambient temperature and a peltier hotstage LTSE120 stage is used for samples that require cooling at a controlled rate to below ambient temperature.

2.2.2 Differential Scanning Calorimetry (DSC)

Differential Scanning Calorimetry (DSC) is a method used to measure and quantify thermodynamic transitions within materials as a function of temperature (or heat flow). Enthalpy is a measurement for the energy in a thermodynamic system. Enthalpy (H) is the sum of internal energy (U) and the product of pressure and volume (P and V respectively)

$$H = U + P \cdot V \quad (2.6)$$

When a process occurs at constant pressure, the heat evolved is equal to the change in enthalpy. The heat flow of the sample is measured from the difference

2.2 Characterisation of materials

in heat flow between a pan with the sample and a reference pan, usually an empty pan (Fig. 2.5). As the sample pan and reference pans are kept at the same pressure, the heat flow can be measured as a function of enthalpy change only. In order to calculate the heat flow for the material, the reference pan heat flow is subtracted from the total heat flow giving the value for the sample material, providing the sample is not interacting with the pan or gasses in the pan. The reference pan is sealed with nitrogen gas as it is inert and will not react with the pan.

$$\Delta \frac{dH}{dT} = \frac{dH}{dT}_{sample} - \frac{dH}{dT}_{reference} \quad (2.7)$$

In endothermic phase transitions such as melting, the heat is absorbed and the heat flow is positive. In contrast, within exothermic phase changes such as crystallisation, the heat flow is negative as the energy is being released by the sample.

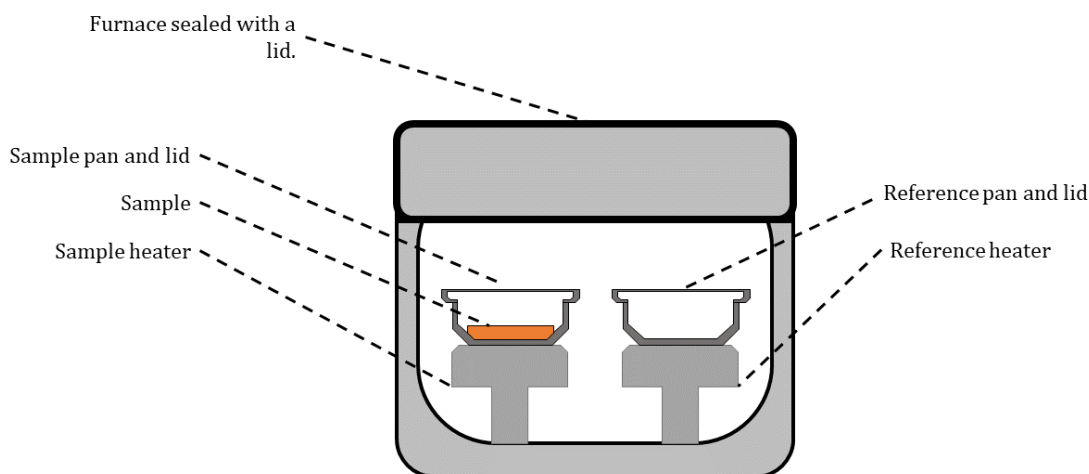


Figure 2.5: A schematic representation of the DSC setup showing the difference between the sample and the reference pan. Both of the pans are sealed airtight. The furnace chamber is filled with nitrogen during the run.

This is a valuable method frequently used within both liquid crystal and polymer fields. Within liquid crystals, it can reveal transition temperatures and nature of phase transitions and whether they are first order or second order.

2.2 Characterisation of materials

Unlike POM, DSC cannot differentiate what mesophases are present and what the transitions correspond to, making POM and DSC complimentary. A first order transition is described as a transition where the discontinuity is in the first derivative of Gibbs free energy and involve latent heat, meaning under DSC they appear as sharp transitions. LC transitions tend to be partially first order and therefore display an observable peak in the trace. Figure 2.6 is an example plot of a DSC curve. In this example, the material looked at is a nematic LC 5CB. On heating the sample, a negative heat flow was observed as the sample was taking in energy in order to increase its temperature. First peak observed corresponds to the melting of the crystal into its LC state, the second peak corresponds to the nematic-isotropic transition and is much less endothermic. On cooling, an exothermic event is observed as the sample transitions from isotropic to nematic. No crystallisation was observed on this cooling run due to super cooling of the 5CB.

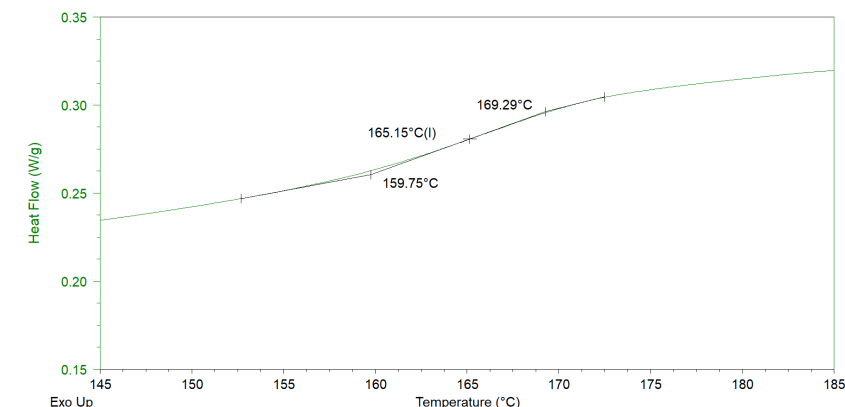


Figure 2.6: DSC heat flow trace for 5CB measured at 10K min^{-1} . A significant endothermic event is observed at phase transition from crystal (K) to nematic (N) and a smaller one for the nematic (N) to isotropic (I). On cooling, an exothermic event was observed where the sample shows negative heat flow as it transitions from I to N. The top and bottom traces correspond to cooling and heating respectively. The crystallisation was not observed on cooling due to super cooling of 5CB.

All of the DSC experiments were performed on the DSC Q20. The heating and cooling cycles were performed at a constant temperature rate. All of

2.2 Characterisation of materials

the analysis was performed using the manufacturer supplied software, Universal Analysis 2000. The phase transitions onset and enthalpy of change for first order transitions were obtained through integration via "Integrate Peak Sig Horizontal" and "Integrate Peak Linear" function build in the software. The values for second order transitions were obtained through "Glass/Step Transition" build in the software. This function works by extrapolating the pre and post transition baselines and identifying the point at which the change in heat capacity is 50% complete. The glass transition temperature is then reported at the 50% mark. An example of values obtained for first order transitions can be seen in Figure 2.6 where 5CB was scanned at a constant rate. Example second order transition values can be see in Figure 2.7 where an example polymer was scanned.

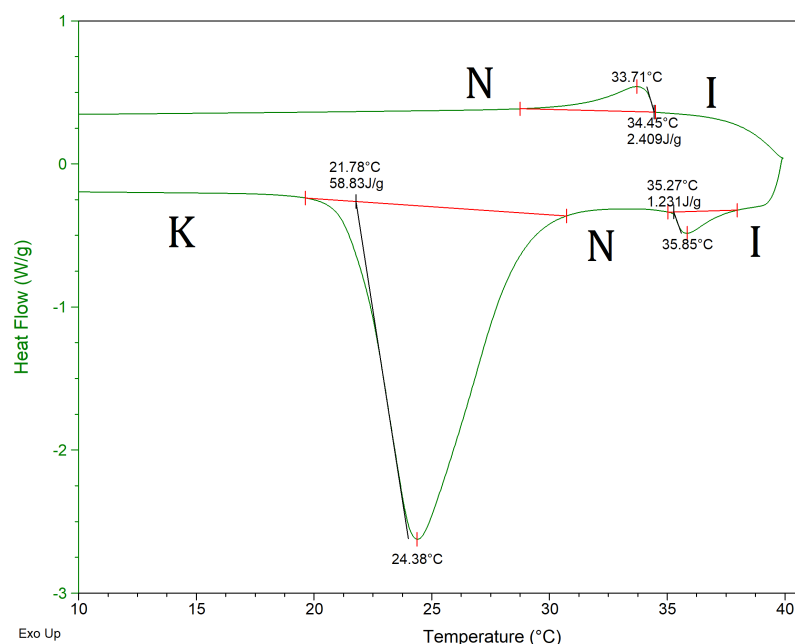


Figure 2.7: DSC heat flow trace for a glass transition of a pure FOEMA polymer (DP = 50) blockcopolymer.

2.2.3 X-ray scattering

X-ray scattering is a family of analytical, non-destructive methods used in the study of structural properties and liquid crystalline properties. This experimental

method was used in Chapters 4 and 5 to study the nano-objects formed through PISA as well as to identify liquid crystalline order within the materials.

Small-angle X-ray scattering (SAXS)

Small-angle X-ray scattering (SAXS) is a powerful method for measuring size, distribution and shapes of particles as well as macromolecules in colloidal suspension.^[66] It offers a unique insight into morphology of the colloidal structure *in situ*, unlike imaging methods such as transmission electron microscopy (TEM) where the sample is in its dried state and frequently stained with other chemicals in order to highlight features. The method relies on exploiting the reciprocity law which gives inverse relationship between measured feature size and scattering angle. Colloidal structures are significantly bigger compare to the X-rays used and therefore gives small observable scattering range. SAXS involves focusing of an X-ray beam onto a sample which then scatters, absorbs or reflects the x-ray or does not interact with it at all (Figure 2.8). The scattered X-rays can be then observed and recorded by a detector. The detector absorbs the X-rays and is usually either a gas-filled detector, solid-state detector or a scintillating detector. The detectors are often used in combinations to ensure better resolution. A beam stop is needed to catch any X-rays which were not scattered by the sample in order to avoid damaging and over-saturating the detector. There are three different types of beamstops usually employed: a full beamstop which catches all X-rays coming through it leading to no detection behind it, a PIN photodiode stop which measures the flux directly or a semi-transparent beamstop which controls how much of the x-rays pass through onto the detector to avoid oversaturation. The beamstop serves two purposes, first to prevent the detector from being damaged by the high intensity unscattered X-ray beam and second to capture any 'parasitic' scattering.^[67] The source of the X-rays is an important factor for the quality of the results. A typical lab-grade SAXS apparatus possesses X-rays sources which emit approx. 10^7 photons per second. This is good enough for standard experiments with well scattering samples. However, for dynamic or position-resolved experiments, synchrotron sources are needed. These provide a much higher X-ray flux at between 10^{11} and 10^{13} photons per second. This also has an added advantage

2.2 Characterisation of materials

of much faster experimental time where the samples only need to be exposed for a fraction of the time they would need at a lab-grade equipment. Synchrotrons also tend to have a much longer paths which leads to higher resolution especially at low q . The *small* in SAXS refers to the angle at which the scattered beams are observed relative to the sample, usually between 0.1 and 10° . As SAXS is frequently performed in solution, the solvent needs to have a different electron density in order to create contrast between the sample. This is described as a difference in the scattering density (ξ) in Equation 2.8.

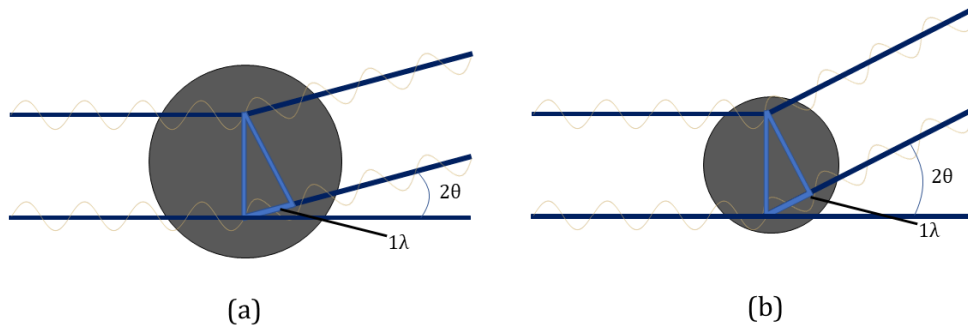


Figure 2.8: Diagram demonstrating small-angle X-ray scattering (SAXS) within two spherical particles with different diameters. (a) Larger particle diameter leads to smaller scattering (b) Small particle diameter leads to wider scattering

$$\xi = \frac{b_e \rho_m N_A}{M_W} \sum_i n_i z_i \quad (2.8)$$

where b_e is the scattering length, ρ_m is the density of the molecule, N_A is the Avogadro's constant, M_W is the weight-average of the molecules, n_i is the number of atoms within the molecule with atomic number z_i . In order to resolve the structure, the q values are converted into d spacing, the two are related by the equation 2.9.^[68]

$$q = \frac{2\pi}{d} \quad (2.9)$$

Electron Dispersive X-ray spectroscopy

Electron Dispersive X-ray spectroscopy (EDS) is a spectroscopic method used for chemical and elemental characterisation. It is similar in nature to X-ray photoelectron spectroscopy (XPS) however it measures the electron instead of the x-rays. EDS offers insight into which elements are present within a part of a sample. EDS can be combined with TEM in order to identify the elements present within a certain area. An example EDS is seen in Figure 2.9. In this example, particular elements can be used in order to identify e.g. parts of blocks of a block copolymer being investigated via TEM rich in a certain part of element.

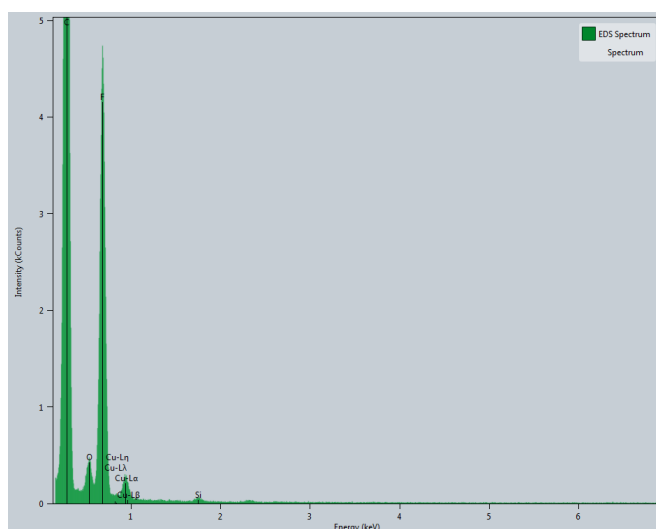


Figure 2.9: An example EDS spectrum collected for a block copolymer of PStMA-b-PFOEMA. The spectrum indicates high relative presence of fluorine group, indicating high abundance of the group within the region scanned in TEM.

Wide-angle X-ray scattering (WAXS)

A method complimentary to SAXS is wide-angle X-ray scattering (WAXS) which is based on a similar principle but the scattering angle measured is higher (i.e. higher Q values are observed). As smaller features, relative to the beam wavelength of X-ray used, scatter more, they can be observed at higher 2θ . While SAXS offers information about structures morphology, WAXS offers insight into the structure at the sub-nanometer scale. At this scale, the samples crystalline

order is probed and important information such as degree of crystallinity, phase composition or crystallite size can be measured.

2.2.4 Data analysis

Data analysis for both SAXS and WAXS was performed using well established tools such as SASView and IgorPRO for fitting as well as manually with Origin scientific data graphing and analysis software and personally written python scripts and code.

Data fitting for SAXS is a non-trivial task. Certain approximations and estimates can be made for general shapes of particles. One example of that is the Guinier fit which relies on providing the diameter (or more specifically speaking, the radius of gyration) of the particle based on the slope of the gradient in the very low q region. This is given in the Guinier approximation (Equation 2.10).

$$\ln I(q) = \ln I(0) - \frac{R_g^2 q^2}{3} \quad (2.10)$$

where $I(q)$ is the intensity of radiation detected, $I(0)$ is the intensity at $q = 0$, usually obtained by extrapolation, R_g is the radius of gyration.

2.2.5 Equipment used

SAXS experiments were performed at Diamond Light Source in Oxfordshire, UK at the I22 beamline. WAXS experiments were performed at University of Leeds, UK in the School of Food Science and Nutrition.

2.2.6 Transmission electron microscopy (TEM)

Transmission electron microscopy (TEM) is a method of imaging nanoscaled objects by transmitting electrons through a thin sample of material and measuring the electrons passing through (Figure 2.10).^[69] Due to electrons much shorter de Broglie wavelength relative to visible light, TEM images are obtained at a much higher resolution compared to standard optical microscopy, allowing to physically

2.2 Characterisation of materials

observe nanostructures. The theoretical limit of optical resolution is described by Abbe diffraction limit (Equation 2.11).

$$d = \frac{\lambda}{2NA} = \frac{\lambda}{2n\sin\theta} \quad (2.11)$$

Here, d is optical resolution, λ is the wavelength of light and NA is the numerical aperture of the lens. The numerical aperture can be described in terms of refractive index of the material the lens is made with. As the wavelength of electrons is much smaller compared to visible light, smaller objects can be resolved in TEM compared to POM.

As electrons are scattered more as a function of the density of the material, stains such as uranyl acetate or ruthenium tetroxide which can interact with the sample and lead to observable artifacts.

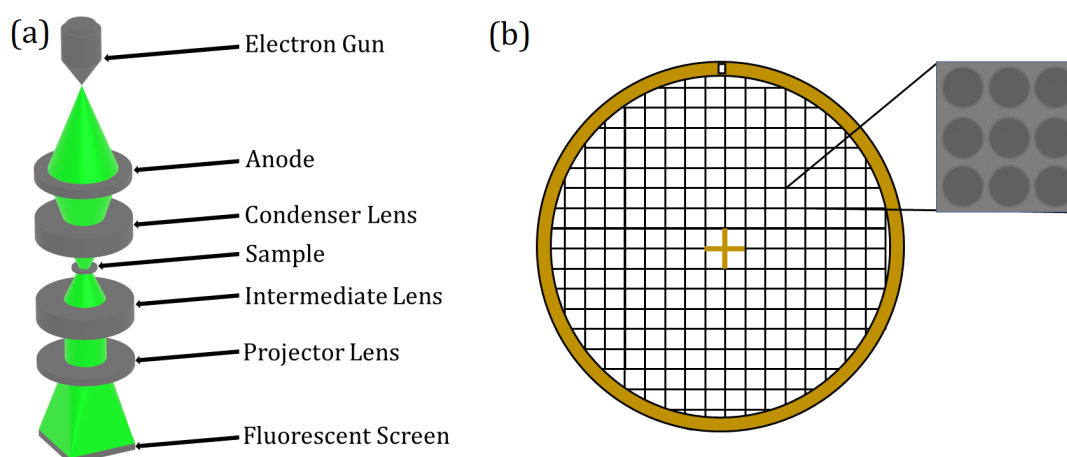


Figure 2.10: (a) Diagram of transmission electron microscopy (TEM) setup. The green indicates electron beam path. (b) A typical copper TEM grid. Within each segment of the grid, multiple periodic holes can be found. The grid is suspended on a Polyvinyl formal and holey carbon support films.

An example image from the TEM can be seen in Figure 2.11. One of the major limitations of this technique is the absence of colour in the collected images. The image is false coloured to appear black and white as the detector collects charge instead of visible light such as in POM.

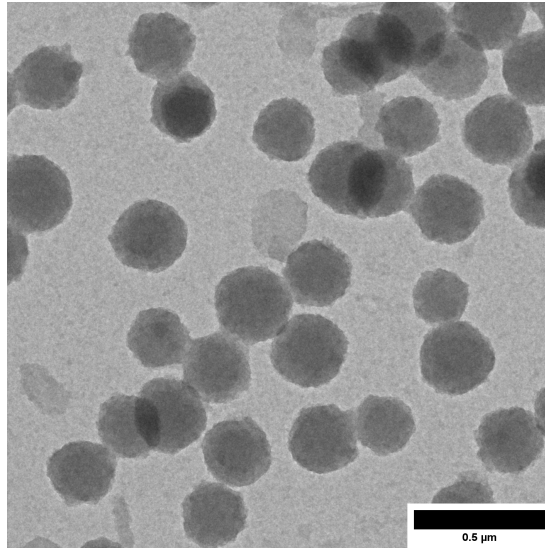


Figure 2.11: An example TEM image of a block copolymer nanoparticle prepared via polymerisation-induced self-assembly. Scale bar = 500nm

2.2.7 Atomic force microscopy (AFM)

Atomic force microscopy (AFM) is a technique that involves scanning a probe across a sample surface and measuring the deflection of the probe with a laser reflection and a photodiode (Figure 2.12) AFM has enabled characterisation of materials at a nanoscale in order not just to image and describe the morphological features of materials but also in order to among other things; probe their mechanical properties, study adhesive properties and characterise their interactions with other materials. AFM is a versatile method which poses multiple different types of operation mode 2.2.

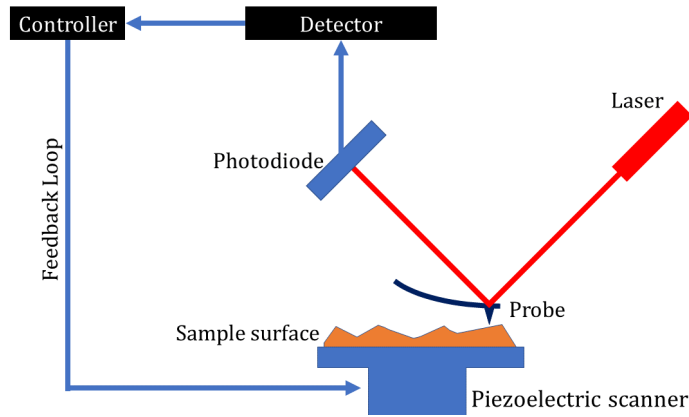


Figure 2.12: A schematic representation of how Atomic Force Microscope works. The laser is constantly scanning the probe which deflects as it interacts with the surface. The reflection of the laser is then measured by the photodiode which passes the data to the detector and controller. Controller then adjusts the position of the scanner based on the setting of the feedback loop.

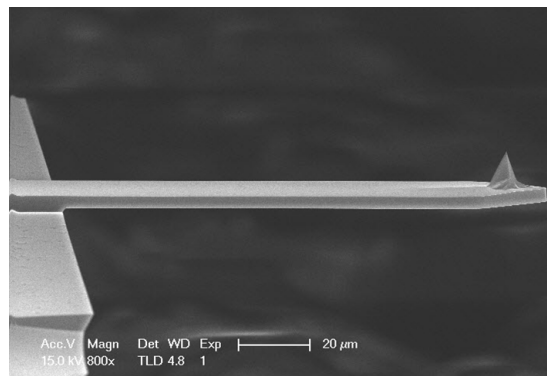


Figure 2.13: An example of a cantilever used for AFM experiments.

2.2 Characterisation of materials

Table 2.2: Different types of AFM modes of operation.

Mode	Feedback	Principle	Uses
Contact	Cantilever deflection	Cantilever is used to scan the surface of the sample at a constant deflection of the cantilever.	Surface structural characterisation
Tapping mode	Oscillation amplitude of the cantilever	Cantilever is made to oscillate at the surface of the sample making contact with the sample only at the lowest point of the oscillation. The oscillation is modulated as a function of its interaction with the surface	Phase resolution and mechanical characterisations
Non-contact	Oscillation amplitude of the cantilever	Cantilever is made to oscillate above the surface of the sample not coming to contact with it. The cantilevers oscillation is affected by the samples surface.	Non-destructive probe

Each of the modes has its advantages. In this thesis, predominantly tapping mode was used for phase characterisation and topological features was used. In order to afford nanoscale resolution, AFM requires the use of a cantilever with a very fine tip which is then used for the actual measurements. There are many different types of cantilevers available, depending on the required application. For soft polymers such as the ones studied in this thesis, the cantilever RTESPA tips from Bruker were used. These cantilevers were designed for use within softer materials such as polymers for experiments performed in air for both contact and intermittent contact modes. The fine control over the movement of the sample is afforded by the piezoelectric stage which relies on a Proportional-Integral-Derivative (PID) feedback loop which is used to control the movement of the stage in response to the signal detected at the photo detector from the cantilever.

2.2.8 Ellipsometry

Ellipsometry is an optical method for measuring thin film properties such as refractive index or thickness. It involves illuminating the sample film with an elliptically polarised light and analysing the reflected beam with an analyser and a photodetector. It can be used to calculate complex refractive index of the material and the thickness of the sample film. It is most commonly in the semiconductor industry to calculate the thickness of SiO₂ on the surface of silicon wafers.

The complete mode of operation for a typical ellipsometer can be seen in Figure 2.14. A monochromatic light linearly polarised light is elliptically polarised through the polariser. The light then proceeds to hit the sample surface at a known angle (usually between 45° and 90°). The reflected light then passes through the analyser which can rotate to measure the polarisation of the light.

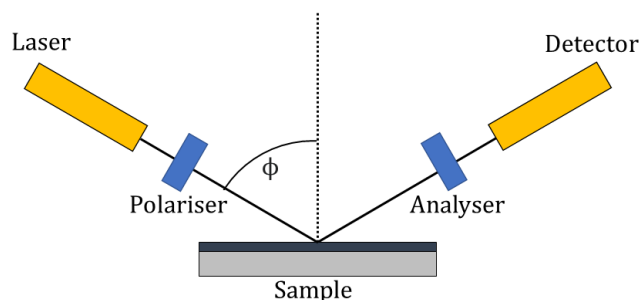


Figure 2.14: A schematic representation of how a typical ellipsometer operates. ϕ is the angle between the detector/light source and the sample surface normal.

As ellipsometry is an indirect method, the calculated values for the optical properties are then calculated through fitting to known models and extracting the fitted values from those.

2.3 Synthetic characterisation

A brief example of methods used for characterisation and track keeping in synthesis are described below.

2.3.1 Solvents and materials

All solvents and reagents were used as provided from the supplier without any further purification or distillation. All materials were used as were delivered from the various suppliers.

2.3.2 Thin layer chromatography

Thin layer chromatography (TLC) is an experimental technique which identifies the number of compounds found within a sample as well as allows to identify purity of the final product. It relies on exploiting the fact that different chemical compounds have different affinity for solvents and therefore diffuse differently within a thin layer of tightly packed silica or alumina. The method is closely related to column chromatography which relies on the same principle to separate the individual components within a sample. The TLC plates were prepared by cutting large sheets into small (approx. 5cm x 10cm) strips, marking the baseline with a pencil and depositing a small amount of the sample material. The strip was then placed in a TLC development jar with a small amount of liquid solvent which does not reach above the marked bottom line. The solvent was then allowed to move up the plate through diffusion and once the solvent has almost reached the top of the strip, the strip is removed and the solvent front is marked with a pencil. The sample is then developed, this is commonly done under UV lamp and by marking the sample spots with a pencil, however not all compounds are UV active and require other methods such as exposure to iodine in order to be developed.

2.3.3 Column chromatography

As mentioned in the section above, column chromatography is a method of purifying crude reaction mixtures into pure individual components. This is done by passing the sample through a column of tightly packed silica or alumina and collecting aliquots, running TLC on each of the aliquots, combining aliquots with the same components and then removing the solvent in order to afford pure product.

2.3.4 NMR spectroscopy

Nuclear magnetic resonance (NMR) spectroscopy was used to characterise the products and byproducts within the samples. The spectra were collected on a Magritek Spinsolve 60 NMR spectrometer and Bruker AV3HD 9.4T NMR spectrometer. Deuterated and hydrogen free solvents were used including deuterated chloroform (CDCl_3), hexafluorobenzene and 1,1,2-Trichloro-1,2,2-trifluoroethane (CFC-113).

Chapter 3

Synthesis of liquid-crystalline methacrylic monomers bearing cholesteryl and cyanobiphenyl mesogens.

3.1 Introduction

In this chapter, methacrylic monomers bearing cholesteryl and cyanobiphenyl mesogens will be synthesised for use in preparation of block copolymers in Chapter 5. These molecules possess methacrylic groups making them suitable to use in polymerisation reactions and laterally attached mesogenic side groups giving them and their corresponding polymers liquid crystalline properties.

3.2 Methacrylic monomers bearing mesogenic groups.

Liquid crystalline polymers offer advantageous mixture of anisotropic properties of liquid crystals with processing and bulk properties of polymers. In particular, side chain liquid-crystalline polymers (SCLP) are noteworthy due to their potential applications based on the mesogens being decoupled from the backbone

3.2 Methacrylic monomers bearing mesogenic groups.

allowing for applications within among other fields optical data storage, nonlinear optics and ferroelectric devices.^[70,71]

Methacrylic LC monomers especially are a well established type of monomers for preparation of SCLPs as they can be readily polymerised using RDRP methods as well as being fictionalised and modified with side groups and spacers.^[46,72] As mentioned in section , the spacers and the mesogenic groups play an important role in the final properties of the resulting polymers and had to be considered when designing new molecules. In this project, monomers were prepared with a spacer consisting of 6 carbon atoms between the backbone and the mesogens. This length was chosen as an optimal length as it is approximately when the glass temperature tends to plateau as a function of spacer length in methacrylic systems allowing for wider LC ranges as well as affording the side groups enough flexibility to freely form wider range of LC phases.^[73] The mesogenic side groups investigated were cyanobiphenyl and cholesterol. Both are well established mesogenic groups used both in SMWLCs and LMWLCs such as polymers.

This chapter will focus on chemical synthesis and characterisation of the above molecules. Their liquid crystalline properties, of intermediates, monomers and polymers, will be discussed in Chapter 5.

3.3 Synthesis of 6-(Methacryloyloxy)hexanoic acid 3-cholesteryl ester (Chol-6-MA)

3.3 Synthesis of 6-(Methacryloyloxy)hexanoic acid 3-cholesteryl ester (Chol-6-MA)

This section will describe the novel synthesis of 6-(Methacryloyloxy)hexanoic acid 3-cholesteryl ester, from here on referred to as Chol-6-MA. The successful synthetic pathway that afforded the pure monomers was done in three steps: firstly preparation of acyl chloride followed by addition of cholesterol to an acyl chloride followed by addition of a methacrylic group via nucleophilic substitution reaction via removal of a bromo group. An overview of the reaction can be seen in Figure 3.1

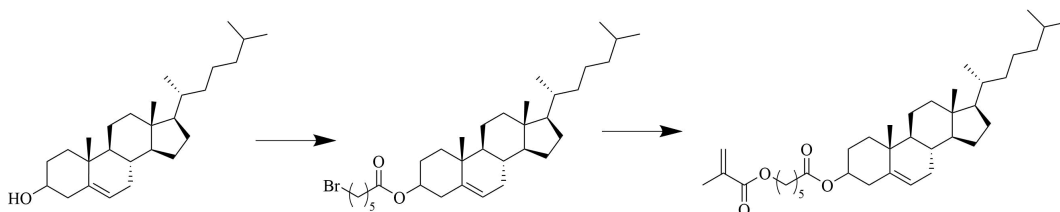


Figure 3.1: Molecular structures of the starting material, intermediate and the end product of Chol-6-MA

3.3 Synthesis of 6-(Methacryloyloxy)hexanoic acid 3-cholesteryl ester (Chol-6-MA)

3.3.1 Step 1: Preparation of acyl chloride

The first step in the reaction was preparation of acyl chloride from a corresponding carboxylic acid with thionyl chloride ($SOCl_2$). This reaction was highly sensitive to moisture so had to be performed in absence of any moisture. The acid was reacted with excess thionyl chloride and then distilled under reduced pressure. The experimental method was adapted from Zuffanti et. al.^[74]

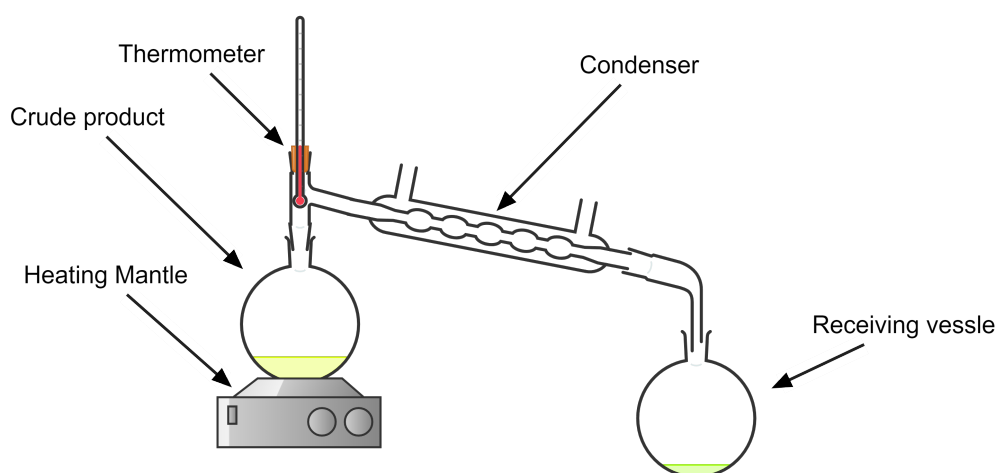


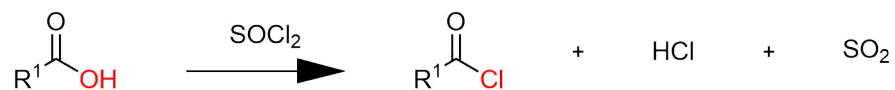
Figure 3.2: Experimental setup for the preparation of acyl chloride through reaction of thionyl chloride with a carboxylic acid.

A typical reaction was performed as follows: To a round bottom flask loaded with carboxylic acid (1 eq.) in a water bath at ambient, excess thionyl chloride (2 eq.) is slowly added from a dropping funnel. After approx. 30minutes, the excess thionyl chloride is removed by distillation, followed by the acyl chloride, discarding the first few drops collected. Yield: 72%.

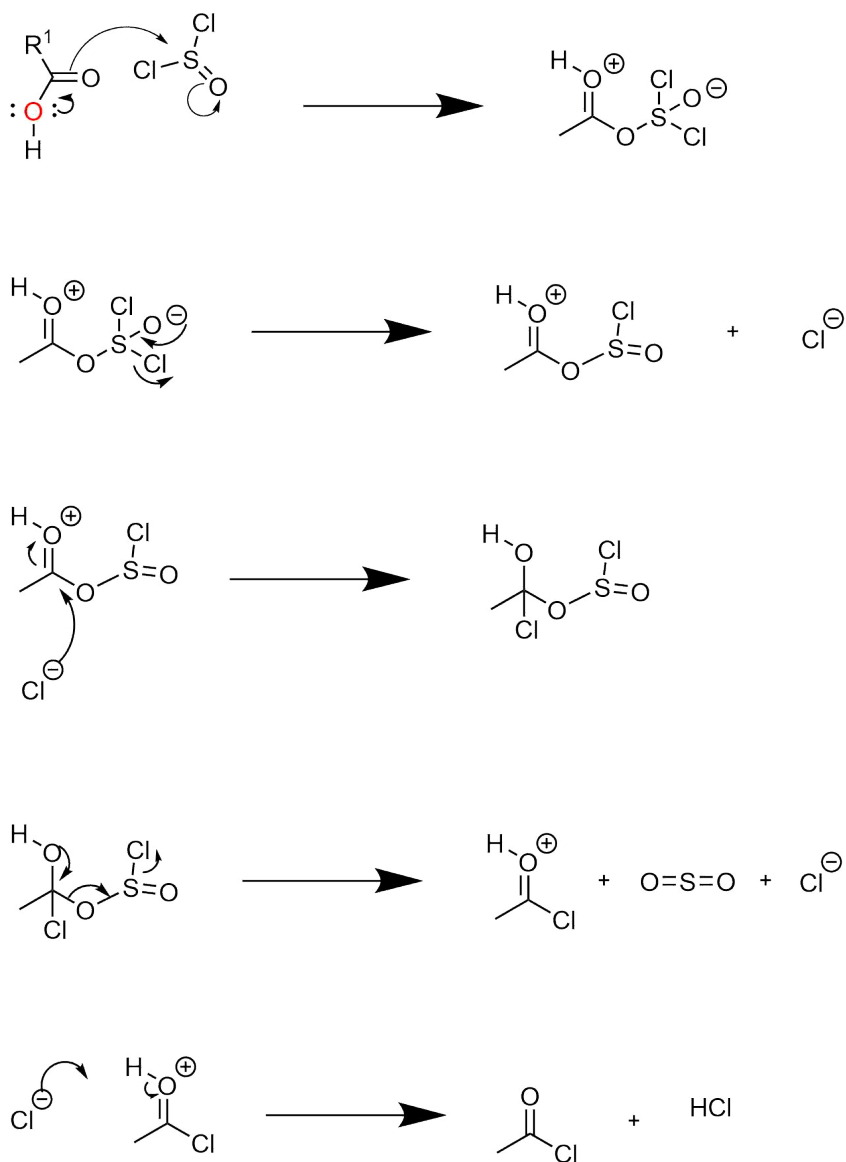
NMR: 1H NMR ($CDCl_3$): 1.2 - 2.0 (6H, m, CH₂), 2.33 (2H, t, CH₂), 3.20 (2H, t, CH₂)

3.3 Synthesis of 6-(Methacryloyloxy)hexanoic acid 3-cholesteryl ester (Chol-6-MA)

Scheme:



Mechanism:



3.3 Synthesis of 6-(Methacryloyloxy)hexanoic acid 3-cholesteryl ester (Chol-6-MA)

Step 2: Esterification of acyl chloride and cholesterol

The next step in the reaction is the formation of an ester bond via condensation reaction between acyl chloride molecule (6-Bromohexanoic acid) and an alcohol (cholesterol). As acyl chlorides react instantly with water (even with moisture in the air), the reaction had to be performed under dry conditions. In order to afford, a dropper funnel was setup connected to a two necked round bottom flask. The system was then sealed with septums and glass stoppers and was placed under vacuum in order to reduce the boiling point of residual water found in the glassware. The entire system was then flame dried with a butane torch. Once the system was completely void of water, the vacuum was removed and the system was filled with nitrogen gas. The reactants were then dissolved in dry solvents and added to the apparatus. The alcohol was dissolved in dry dichloromethane (DCM) with a small volume (approx. 2cm^{-3}) of dry pyridine and transferred to the round bottom flask. The acyl chloride was a pale yellow liquid and was used as was without dilution in any solvent. It was transferred to the dropping funnel. The RBF was placed on a magnetic stirrer plate with an ice-bath. The acyl chloride was then slowly added dropwise over approx. 30min to the stirring solution of alcohol. As the reaction of acyl chlorides are very exothermic, the reaction had to be performed in an ice-bath initially and was later kept at ambient overnight temperature to ensure complete reaction. The setup can be seen in Figure 3.4. The reaction was then worked up and purified.

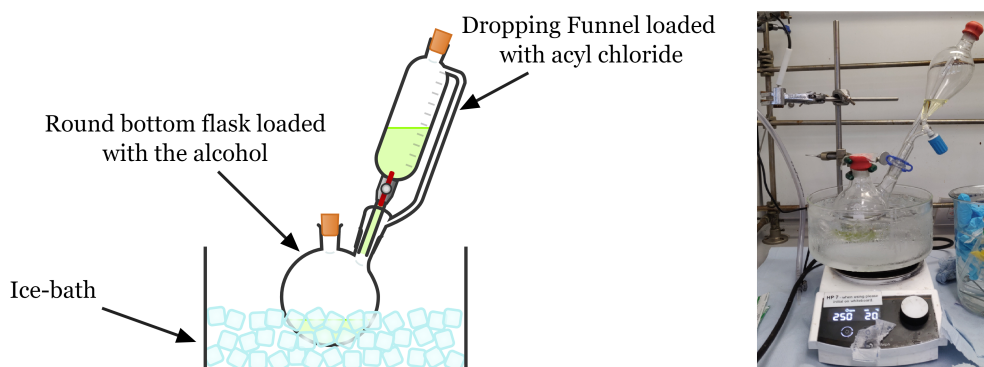


Figure 3.3: Experimental setup for the reaction of acyl chloride and an alcohol.

3.3 Synthesis of 6-(Methacryloyloxy)hexanoic acid 3-cholesteryl ester (Chol-6-MA)

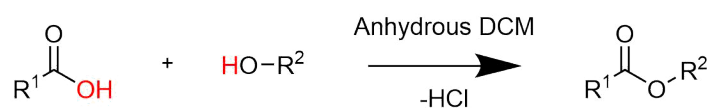
A typical synthesis of Chol-6-Br was performed as follows:

Cholesterol (1 eq.) was dissolved in dry dichloromethane and 2ml of dry pyridine and added via syringe to two necked, dried round bottom flask with a magnetic stirrer bar and a dropping funnel attached. The apparatus was placed in an ice-bath. To the closed dropping funnel, 6-bromohexanoyl chloride was added via syringe. With stirring, the dropping funnel was slowly opened until a steady, slow addition of acyl chloride was achieved. The acyl chloride was added over approx. 30 minutes. After complete addition, the reaction was let to mix overnight at ambient temperature. On the following day, the organic layer was washed with water, dilute sodium carbonate and water. The organic layer was then dried with brine and anhydrous magnesium sulfate. Product was purified by recrystallisation from ethanol and methanol. Yield: 97%.

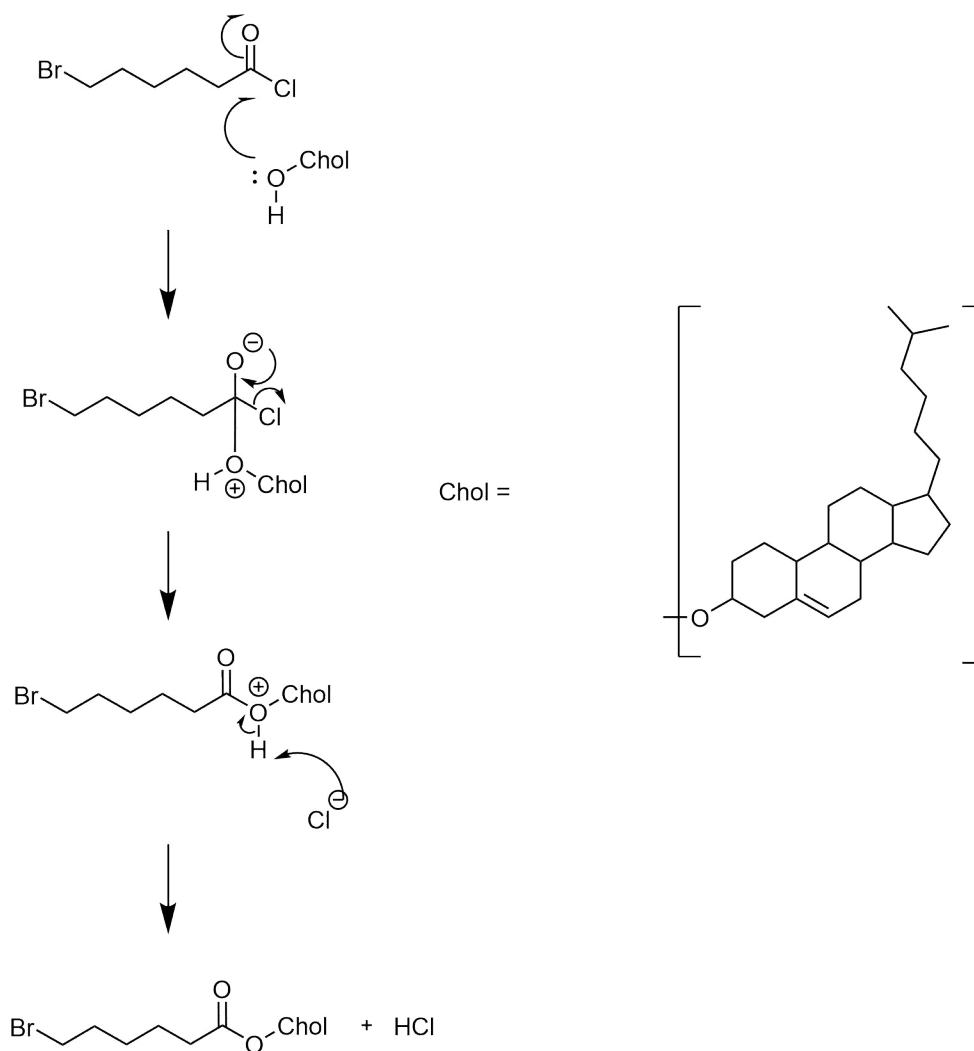
NMR: ^1H NMR (CDCl_3): 0.6–2.1 (50H, m, CH,CH₂,CH₃), 2.33(4H, m, CH₂), 3.42 (2H, t, CH₂), 4.61 (1H, m, CH), 5.37 (1H, m)

3.3 Synthesis of 6-(Methacryloyloxy)hexanoic acid 3-cholesteryl ester (Chol-6-MA)

Scheme:



Mechanism:



3.3 Synthesis of 6-(Methacryloyloxy)hexanoic acid 3-cholesteryl ester (Chol-6-MA)

3.3.2 Step 3: Addition of methacrylic group

The addition of methacrylic group was performed by nucleophilic substitution of the bromo group with a methacrylate group. The methacrylate group was prepared by neutralisation of methacrylic acid with a weak base, potassium hydrogen carbonate. The salt was then reacted with the intermediate prepared above at 90°C over 24 hours. As the reaction involved heating monomers, precautions had to be taken in order to ensure no polymerisation takes place during the reaction. This was done by addition of small amount of 2,6-Di-tert-butyl-4-methylphenol (BHT). This antioxidant captures any radical species that might form during the reaction and prevents them from starting a free radical polymerisation reaction.

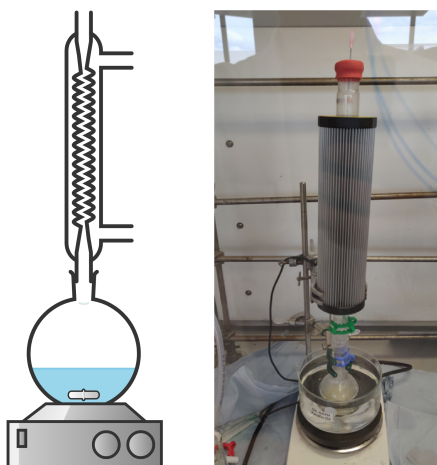
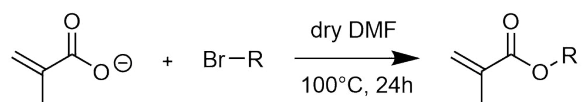


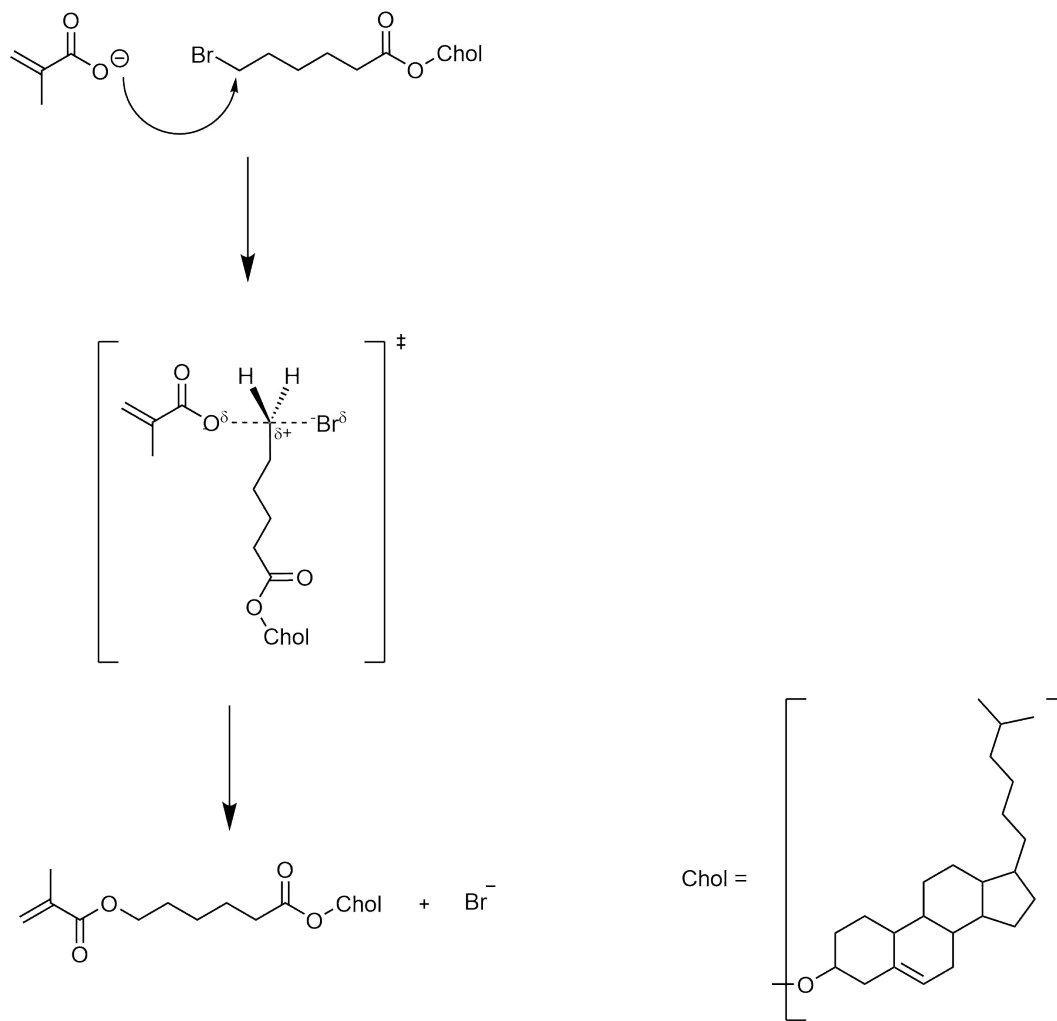
Figure 3.4: Experimental setup for the reaction of acyl chloride and an alcohol.

3.3 Synthesis of 6-(Methacryloyloxy)hexanoic acid 3-cholesteryl ester (Chol-6-MA)

Scheme:



Mechanism:



3.3 Synthesis of 6-(Methacryloyloxy)hexanoic acid 3-cholesteryl ester (Chol-6-MA)

A typical synthesis of Chol-6-MA was performed as follows:

Methacrylic acid (1.1 eq.) and potassium hydrogen carbonate (1.1 eq.) were added to a round bottom flask with a magnetic stirrer bar and mixed at room temperature for 5 minutes to form potassium methacrylate salt. Cholesteryl 6-bromohexanoate (1 eq.) and 2,6-Di-tert-butyl-4-methylphenol (BHT, 0.1 eq.) was dissolved in N,N'-dimethylformamide (DMF) and added to the reaction mixture. The reaction mixture was heated to 100°C and stirred over 24 hours. On the following day, the solution was allowed to cool. Dichloromethane (DCM) and water were added to the cold solution. The organic layer was washed with water, dilute sodium carbonate, water and brine. The organic layer was then dried over anhydrous magnesium sulfate and solvent was removed under reduced pressure. The product was then purified through column chromatography (pure DCM, silica gel) and recrystallised from ethanol. Yield: 65% ¹H NMR in *CDCl*₃ 1.3-2.2 (9H, m, CH₂,CH₃), 2.6 (2H, s), 4.2 (2H, s), 5.58 (1H, m), 6.12 (1H, m), 7.0 - 8.0 (8H, m)

3.3 Synthesis of 6-(Methacryloyloxy)hexanoic acid 3-cholesteryl ester (Chol-6-MA)

3.3.3 Synthesis of 6-(4-Cyano-biphenyl-4'-yloxy)hexyl methacrylate (CB-6-MA)

Synthesis of 6-(4-Cyano-biphenyl-4'-yloxy)hexyl methacrylate (CB-6-MA) was performed by a similar process as for Chol-6-MA. The same acid chloride was used in preparation of both of the monomers.

Step 2: Esterification of acyl chloride and CB-OH

The process of preparation CB-6-Br was almost identical as in the case of Chol-6-Br. A typical synthesis of CB-6-Br was performed as follows:

4-Cyano-4'-hydroxybiphenyl (CB-OH) (1 eq.) was dissolved in dry dichloromethane and 2ml of dry pyridine and added via syringe to two necked, dried round bottom flask with a magnetic stirrer bar and a dropping funnel attached. The apparatus was placed in an ice-bath. To the closed dropping funnel, 6-bromohexanoyl chloride was added via syringe. With stirring, the dropping funnel was slowly opened until a steady, slow addition of acyl chloride was achieved. The acyl chloride was added over approx. 30 minutes. After complete addition, the reaction was let to mix overnight at ambient temperature. On the following day, the organic layer was washed with water, dilute sodium carbonate and water. The organic layer was then dried with brine and anhydrous magnesium sulfate. Product was purified by recrystallisation from ethanol twice. Yield: 92%.

NMR: 1H NMR ($CDCl_3$): 1.4–2.3 (6H, m, CH₂), 2.67(2H, m, CH₂), 3.51 (2H, t, CH₂), 7-8 (8H, m, aromatic)

Step 3: Addition of methacrylic group

A typical synthesis of CB-6-MA was performed as follows:

Methacrylic acid (1.1 eq.) and potassium hydrogen carbonate (1.1 eq.) were added to a round bottom flask with a magnetic stirrer bar and mixed at room temperature for 5 minutes to form potassium methacrylate salt. 4'-cyanobiphenyl-6-bromohexanoate (1 eq.) and 2,6-Di-tert-butyl-4-methylphenol (BHT, 0.1 eq.) was dissolved in N,N'-dimethylformamid (DMF) and added to the reaction mixture. The reaction mixture was heated to 100°C and stirred over 24 hours. On the following day, the solution was allowed to cool. Dichloromethane (DCM)

3.3 Synthesis of 6-(Methacryloyloxy)hexanoic acid 3-cholesteryl ester (Chol-6-MA)

and water were added to the cold solution. The organic layer was washed with water, dilute sodium carbonate, water and brine. The organic layer was then dried over anhydrous magnesium sulfate and solvent was removed under reduced pressure. The product was then purified through column chromatography (pure DCM, silica gel) and recrystallised from ethanol twice. Yield: 62%

¹H NMR in *CDCl*₃ 1.4-2.3 (6H, m, CH₂), 2.61 (2H, s), 4.23 (2H, s), 5.52 (1H, m), 6.09 (1H, m), 7.0 - 8.0 (8H, m)

3.3 Synthesis of 6-(Methacryloyloxy)hexanoic acid 3-cholesteryl ester (Chol-6-MA)

3.3.4 Notes and unsuccessful attempts at preparing the monomers

Organic chemistry can be tricky and occasionally do unexpected things for reasons not entirely clear to the chemist at the time. The above synthetic pathway is the most successful and most straightforward one given the facilities. The first attempts at preparing the Chol-6-MA were made using a phase transfer catalysed reaction as adapted from Shannon et. al.^[75]. This method involved two immiscible phases (water and chloroform) each with a different reactant dissolved in it being boiled under reflux and 'emulsifying' the reagents with the phase transfer catalyst. This method was abandoned as the yield collected from it was in single digits (occasionally 0%). The reaction was also extremely slow, taking over 48 hours.

Acyl chlorides are well known to react vigorously with water and any alcohol. This makes them relatively dangerous to synthesis and use in the labs. There are many different ester forming reactions and one of the most common one used nowadays is Steglich esterification. This reaction involves using a carbodiimide activating agent (usually DCC or EDC.HCL). This reaction has an advantage over other common esterification reactions as it is quick and does not involve using elevated temperatures. The downside of this reaction however is the convoluted workup involving difficult to remove byproducts as well as the hygroscopic nature of DCC which resulted in lower yields. As such, the monomers were prepared via preparation of acyl chlorides.

During the workup in step 2, emulsions would form readily in the separating funnel. In order to 'break' the emulsions, brine was used during the wash in order to increase the ionic strength of the aqueous phase. Alternatively, a small amount of pure sodium chloride was added. A small volume of acetone (approx. 10ml) was also occasionally used up to break the emulsion.

Chapter 4

Self-assembly of liquid crystalline block copolymers bearing mesogenic perfluorinated side groups

4.1 Introduction

Preparation of well-defined nanoobjects is an important field of research with applications in fields such as biomedicine^[76,77], biomaterials^[78], microelectronics^[79,80] and photoelectric materials^[81,82,83]. One of the most common forms of preparing such nanoobjects is through self-assembly of block copolymers (BCP) in solution. Traditional way of producing BCP nanoparticles however, involves multi-step procedures with severe limitations such as the requirement to conduct the process at low concentrations (usually around 1-2% w/w solids), often with a requirement for undesirable solvent^{[84][85]}. It is often achieved through methods such as solvent, pH switching or thin film re-hydration^[86]. Polymerisation-induced self-assembly (PISA) via reversible addition fragmentation chain transfer (RAFT) polymerisation^[87,88,89] is an efficient and reliable strategy for producing well-defined nanoobjects where size and morphology can be fine-tuned by controlling variables such as degree of polymerisation (DP) of each of the block, solvent, solids concentration and the relative amphiphilicity of the blocks. Furthermore, a

significant advantage over conventional methods is the ability to perform syntheses at high % solids concentrations (up to 50% w/w).^[84,90,91] Liquid crystalline (LC) monomers have also been incorporated into PISA systems where the LC order provides a competing force driving the self-assembly on the mesoscale. This results in a significant additional contributing factor to the overall PISA process and the resulting nanoobject morphology. Liquid crystalline order is a competing force driving the self-assembly on the microscale. For example, Charleux and co-workers demonstrated that polymerizing a cholesterol-containing monomer by RAFT dispersion polymerisation in the presence of poly((meth)acrylic acid-co(poly(ethylene glycol) (meth) acrylate) macromolecular chain transfer agent (macro-CTA) in ethanol/water mixtures produced solely nano-fibres in the presence at wide range of concentrations. SAXS, SANS and cryo-TEM revealed that the cholesterol groups reside inside the nanoobjects with a constant layer spacing, typical of a smectic order. Azobenzene bearing monomers have also been shown as suitable candidates for use in PISA, whereby a methacrylic azobenzene based monomers is polymerised in the presence of a poly(methacrylic acid) macro-CTA in ethanol. In this case rare morphologies such as cubes and belts were observed.^[61] Additionally, by exploiting the ability to photoisomerise the azobenzene group it was possible to induce a transition to an isotropic morphology by irradiating with UV light. LC order was also shown to help stabilise and lock in place 1D nanowires through cross-linking under UV exposure.^[92]

Polymers bearing semifluorinated polymethacrylates are a well known class of LC forming macromolecules. These can form smectic phases in thin films^[37,38,39] and in bulk.^[40] Polymers containing perfluorinated side groups have a strong tendency to form LC order, being more rigid and more tightly packing compare to their alkene equivalents. Unfortunately, analogues to many fluorinated materials, they tend to be insoluble in most common solvents.

Hue et al. has described a process where the 2-(perfluorooctyl) ethyl methacrylate (FOEMA) was polymerised as a third block in the presenece of poly(N,N-dimethylaminoethyl methacrylate)-b-poly(benzyl methacrylate) (PDMA-b-PBzMA) 'seeds'. resulting structures included spheroids, ellipsoids, cylinders and spherical multi compartment micelles (MCMs).^[41] Li et al. has demonstrated preferential assembly of ellipsoidal nanoparticles fusing head-on-head to form nanotubes.^[42]

It has been demonstrated that liquid crystalline order (in particular, smectic phases) lead to an ellipsoidal^[38] and various faceted^[43] morphologies, both difficult to achieve with standard PISA.

The aim of this experimental work was to build up on this knowledge by expanding the type range of achievable structures prepared via PISA with 2-(Perfluorohexyl)ethyl methacrylate (FOEMA) and to investigate the evolution of the morphology of the resulting structures

Herein we report the preparation of amphiphilic diblock copolymer nanoparticles bearing liquid crystalline side groups in non-polar solvent. A series of poly(stearly (meth)acrylate)-*b*-poly(perfluorooctyl ethyl (meth)acrylate) (PStMA-*b*-PFOEMA) nanoobjects was prepared through PISA in *n*-dodecane at various degrees of polymerisation of the PFOEMA block. This gave us insight into the influence of the liquid crystal order within PISA self-assembly and the resulting structures. We demonstrate the morphology of the nanoparticles formed is a function of the fraction of the solvophobic block. We also probe the liquid crystalline order found within the resulting structures and its responsiveness to temperature. The resulting nanoobjects were characterised via DLS, TEM, SAXS and WAXS.

4.2 Background

In a typical PISA process, the chain extension of the core-forming block leads to larger structures which tend to fuse together to form worms and lamellar structures.^[93] This makes formation of rigid 1D structures such as nanorods and nanotubes difficult to achieve. While certain methods of preparing these structures through PISA exist^[94,95,96,97] the arsenal for preparing these structures remains limited. A potential solution to this problem is using a liquid-crystalline forming monomers. LC BCPs have been shown to form 1D structures in PISA, for example Wang al. reported the formation of rod-like micelles within a wide range of BCP composition windows containing a polyferrocenyldisilane block.^[98] Li et al. reported preferential formation of 1D nanorods in systems bearing Cholesteryl LC forming groups.^[25] Perfluorinated groups are an atypical mesogenic groups. These calamitic LCs form smectic phases due to their bulky and

rigid nature.^[99,100] This class of monomers has also been used in PISA; short per-fluorinated chains do not display LC properties however still self-assemble.^[101,102] Only longer side groups (usually >7 carbons long) form LC phase.^[42] The structures formed displayed responsive nature with programmable shape transitions as a function of temperature.^[58] They have also been shown to fuse in a directional way to form nanotubes.^[42] In recent years, there have been significant developments in the field of self-assembly of semi-fluorinated liquid-crystalline BCPs. Originally a field studied in the 80s and 90s but mostly abandoned due to limited solubility of the polymers, lack of variety between available monomers and the necessity to use fluorinated solvents, initiators and ligands. The field has seen resurgence thanks to developments of new polymerisation techniques that overcame limitations presented in the early polymerisation techniques.^[38,103] In particular, developments withing the RDRP polymerisation techniques have allowed for synthesis of well defined perfluorinated polymers of longer lengths and with well defined features. The unique strengths of the semi-fluorinated BCPs lie in their strong tendency to self-assemble due to strong phase segregation between the fluorinated and nonfluorinated blocks. Their strong hydrophobic nature and natural low refractive indices have made them find use within optics, interfaces and energy devices.^[104,105,106] .

4.3 Synthesis

A series of PStMA-b-PFOEMA polymers were prepared through reversible addition-fragmentation chain transfer polymerisation (RAFT) at fixed concentration and solvent with various degrees of polymerisation of each of the FOEMA block. The degree of polymerisation was controlled by the feed ratio and measured with 1H NMR. The preparation of PISA particles was performed at a fixed weight concentration of 15% w/w. Initial studies with higher degrees of polymerisation of the fluorinated block were not successful as the polymerisation stopped at degree of polymerisation (DP) approximately 100. This is an improvement over conventional synthesis of polymers with long fluorinated side chains, which display a limited solubility in conventional solvents.

4.3.1 Synthesis of macro chain-transfer agent

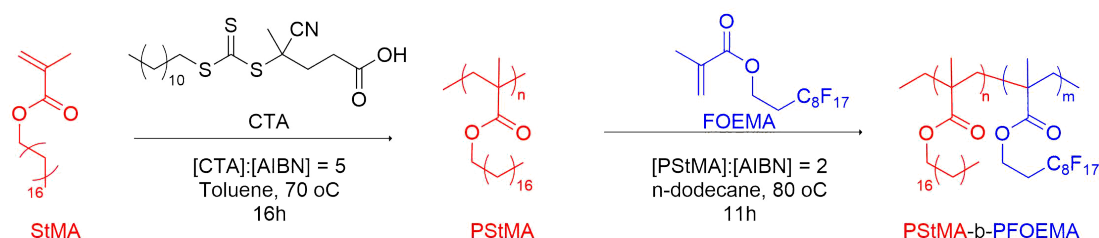


Figure 4.1: Synthetic pathway for preparing PStMA-b-PFOEMA block copolymer via PISA

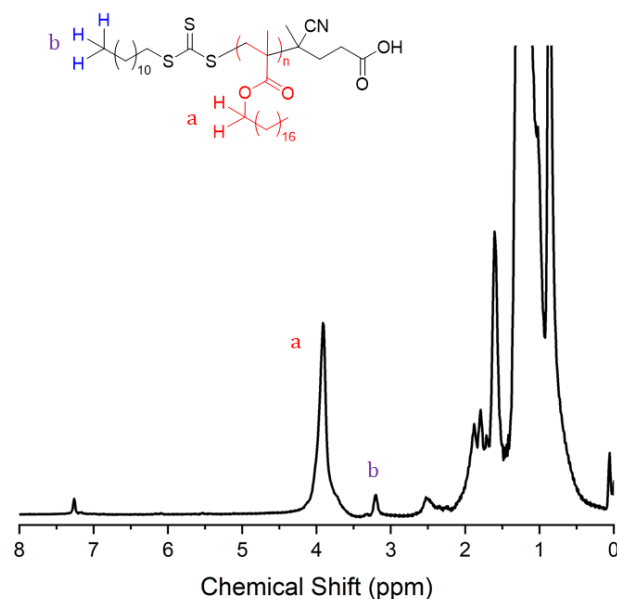


Figure 4.2: Assigned ^1H NMR spectra for the PStMA mCTA prepared via RAFT synthesis.

PStMA homopolymers were synthesised via homogeneous RAFT polymerisation in solution in toluene (Figure 4.1). StMA, CTA, AIBN and toluene were added to a reaction flask. The flask was sealed with a septum and the solution was degassed by sparging with dry N_2 . The flask was heated to 90 °C for 8 hours. The reaction mixture was then quenched and precipitated twice in methanol. The

mean degree of polymerisation was calculated from the ^1H NMR by comparing the relative signals from the CTA:monomer signal. The NMR spectra used can be seen in Figure 4.2. The mean degree of polymerisation of the macro-CTA was calculated to 11 by comparing the ^1H NMR signals of the CH_3 group on the CTA and the CH_2 group on the StMA (Equation 4.1).

$$\begin{aligned}
 I_{CTA} &= 3H \\
 I_{StMA} &= 2H \\
 DP &= \frac{3I_{StMA}}{2I_{CTA}} \\
 DP &= \frac{22.3}{2} = 11
 \end{aligned}
 \tag{4.1}$$

The reaction kinetics were measured and used to determine optimal reaction time.^[107]

4.3.2 Preparation of $S_{11} - F_x$ (S = PStMA, B = PFOEMA, subscript represents DPs) assemblies by PISA.

A kinetic study of synthesis of $S_{11} - F_{100}$ vesicles was performed at 80°C in order to determine appropriate reaction conditions (Figure 4.3). This was performed through ^1H NMR only as the samples were not suitable for SEC (GPC) due to poor solubility of the polymer in the GPC solvents. The kinetic study showed steady conversion of the monomer over a course of approx. 660minutes. As a result, all RAFT polymerisations used to prepare the $S_{11} - F_x$ particles were performed at 80°C for 11 hours to maximise the monomer conversion.

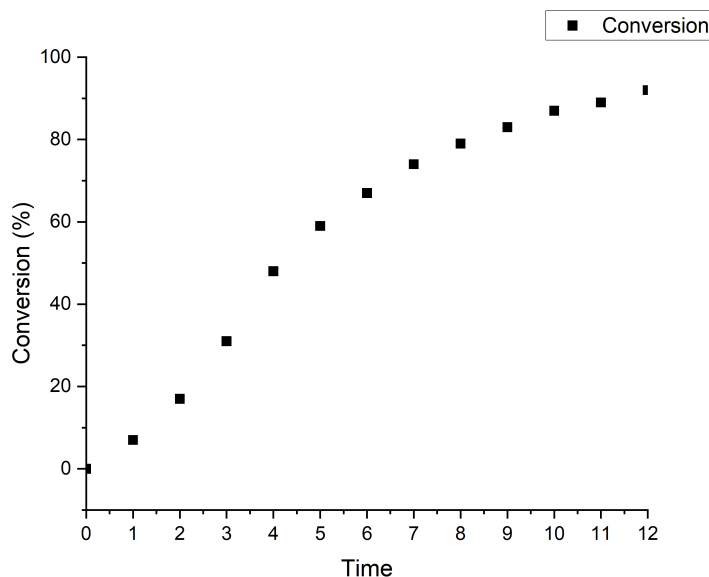


Figure 4.3: Conversion of FOEMA vs. polymerisation time, calculated by ^1H NMR performed at 80°C in n-dodecane using the StMA_{11} mCTA and AIBN at 15%, $[\text{mCTA}]:[\text{AIBN}] = 2$.

$S_{11} - F_x$ assemblies were prepared by RAFT polymerisations of FOEMA in n-dodecane utilising $P\text{StMA}_{11}$ as a macro-CTA. The feed ratio was varied between 10 and 100. In a typical RAFT dispersion polymerization at 15% solids (Figure 4.1), PStMA macro-CTA, AIBN and FEOMA were dissolved in n-dodecane in a reaction flask. The reaction flask was degassed by sparging with dry N_2 gas and heated at 80°C for 11 hours. The reaction was quenched by exposure to air. A small aliquot was taken for conversion measurements to ensure the polymerisation has finished. The conversion was calculated by observing the monomer vinyl peaks integral area relative to the polymer backbone in ^1H NMR and by calculating the DP.

4.4 Results and discussion

4.4.1 Characterisation of $S_{11} - F_x$ diblock copolymers

The $PStMA_{11}$ macro-CTA was chain-extended with FOEMA monomer targeting a range of degrees of polymerisation (DPs) between 10 and 100 at a fixed solids concentration of 15%. The conversion was calculated through ^1H NMR.

The size of the nanoobjects prepared was investigated using DLS, TEM and SAXS. The DLS size distribution is summarised in Table 4.1. Due to lack of solubility of the diblock in either DMF or THF, GPC traces could not be collected and therefor the polydispersity had to be obtained from DLS. This has also limited meaningful analysis of the molecular weights of the BCPs through SEC.

Table 4.1: Summary of the dispersion polymerisations of FEOMA in n-dodecane at 80°C at 15% weight solids.

Feed ratio ^a	Conv ^b %	D_h ^c (nm)	PDI ^c
1/10/0.5	99	146	0.12
1/20/0.5	99	213	0.16
1/35/0.5	99	318	0.14
1/50/0.5	99	385	0.04
1/75/0.5	99	301	0.02
1/100/0.5	99	535	0.05

^aMolar ratio ($PStMA_{11}$ -CTA/FOEMA/AIBN). ^b Monomer conversion determined by ^1H NMR spectroscopy. ^cThe hydrodynamic diameter and polydispersity index (PDI) of the nanoparticles characterised by DLS at 1% concentration.

DSC experiments on all of the precipitated bulk $S_{11} - F_x$ BCPs exhibited two transition, one corresponding to the melting of Stearyl block and one corresponding to the melting of the FOEMA block. Both of these transitions were first-order transitions. The transition temperature of the FOEMA block was found to increase as a function of DP, from 80°C at DP = 10 to 81.4°C at DP = 100, suggesting increased stability of the LC phase found in the membrane (Figure 4.5). Thermal stability of the BCPs was probed with TGA experiment. The material was found to degrade in two individual steps, corresponding to the breakdown of each of the blocks (Figure 4.4). The breakdown of each of the

4.4 Results and discussion

block was identified by the relative fraction mass lost of the polymer as well as correlating with literature values.^[108,109] The first step in TGA found to onset at 170.4°C corresponds to the breakdown of steryl methacrylate block where as the second step corresponds to FOEMA block. The relative low thermal stability of the polymers makes it difficult to thoroughly study under POM as seen in section 4.4.2.

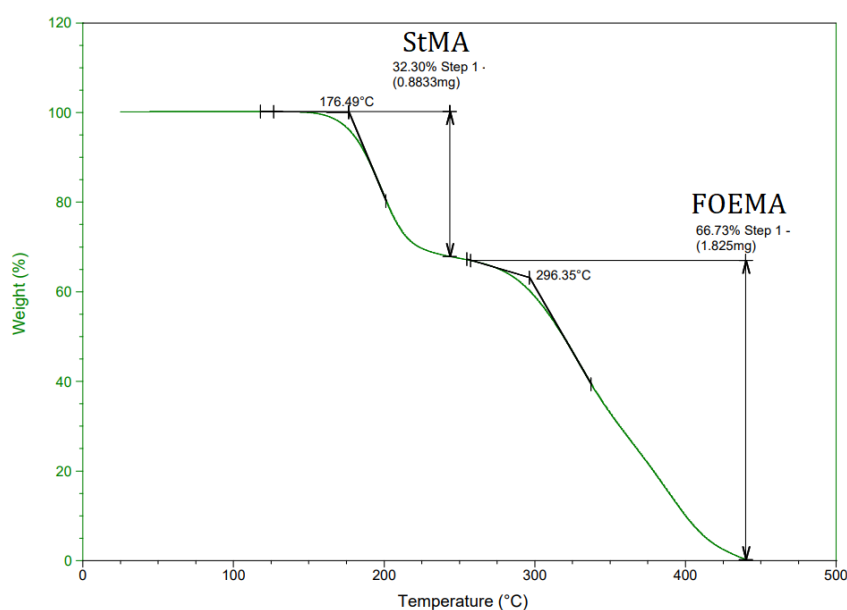


Figure 4.4: Thermogravimetric analysis (TGA) of $S_{11} - F_{25}$. Two discrete steps were observed for the material. The blocks were assigned based on the relative mass of each of the fragments based on the degree of polymerisation.

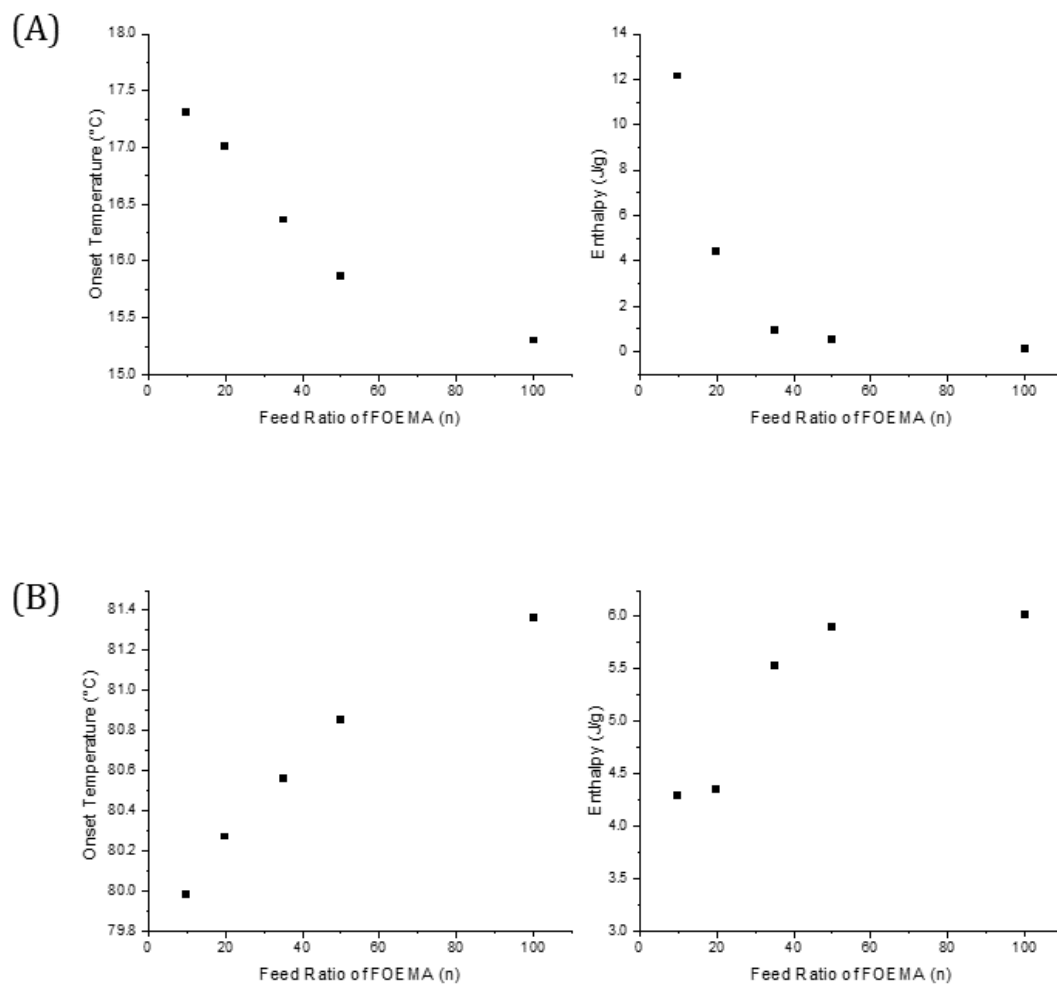


Figure 4.5: DSC onset temperature of transition (left) and enthalpy of change (right) of melting of (A) StMA block and (B) FOEMA block.

4.4.2 Morphology of PStMA-b-PFOEMA nanoobjects

TEM and DLS were utilised to study the size and morphology of the assemblies. The $S_{11} - F_{10}$ seeds were found to be elliptical micelles with major axis of 202nm and minor axis of 146nm. These particles appeared uniform throughout with

no identifiable features observed inside of them. Upon chain extension of the F block, the $S_{11} - F_{20}$ particles formed 1D nanowires (Figure 4.6b). The tubular micelles were inconsistent in length but uniform in thickness at 70nm. A small amount of these was found to be opening up at ends of the rods. Further chain extension in $S_{11} - F_{35}$ showed a change in the morphology of the particles where some of them appeared to be rods similar in width to the ones seen in $S_{11} - F_{35}$ while some of the particles were found to be opening up to form more ellipsoidal particles. The open particles possessed a well defined membrane with a lighter internal layer. The width of the particle wall was found to be constant at 35 ± 1 nm through the wall, with the exception of the pinch points at each end of the opening where the membrane was thicker, up to 75nm in width. Further chain extension lead to formation of poorly defined amorphous particles from $S_{11} - F_{50}$. While they did not posses reproducible structure, they did show vesicular walls similar in thickness to those found in the shorter BCPs. $S_{11} - F_{75}$ formed spherical large compound vesicles (LCVs). These were uniform in size at 250nm under the TEM. The particles showed a tendency to cluster together (Figure 4.6e, inset). $S_{11} - F_{100}$, the largest particles formed spherical LCVs with internal order being observed under the TEM(4.6f, inset). These particles were significantly bigger compared to the previous ones, being found up to 555nm in size. Partial fusion of the compartments was observed to form interconnected internal structure due to dense packing.

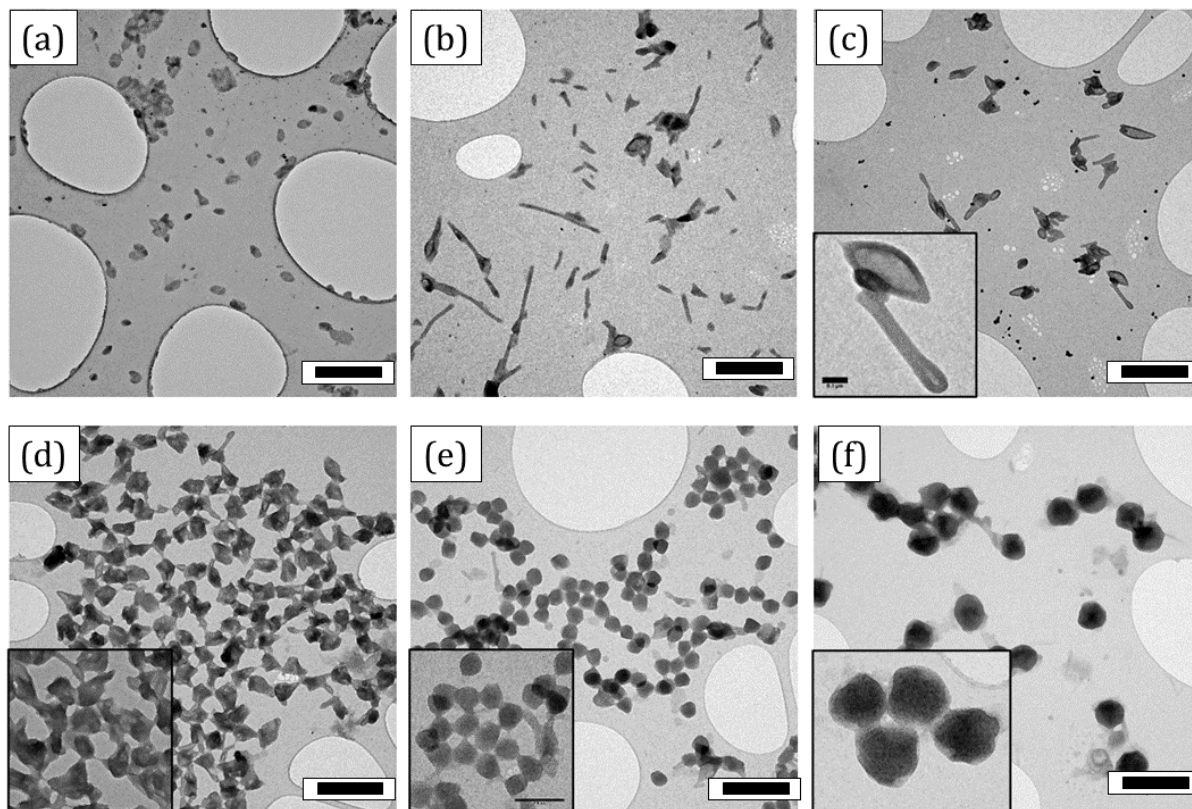


Figure 4.6: Transmission electron microscopy (TEM) micrographs of PStMA10-b-PFEOMAn nanoparticles prepared via RAFT mediated PISA stained with ruthenium tetroxide. (a) $n = 10$, spherical micelles, (b) $n = 20$, cylindrical micelles, (c) $n = 35$, ellipsoidal vesicles, (d) $n = 50$, ellipsoidal vesicles, (e) $b = 75$, large compound vesicles (f) $n = 100$, large compound vesicles. Insets show zoomed in sections. Black scale bar corresponds to $1\mu\text{m}$.

The 1D structures of $S_{11} - F_{20}$ nanoobjects were investigated further to determine their fusion mechanism. These 1D cylindrical micelles demonstrated preferential directional fusion along the long axis of the tubes (Figure 4.7). The average length of the individual rods was found to be $290 \pm 25\text{nm}$ with width of $67 \pm 6.4\text{nm}$. After fusion of the particles, the resulting cylindrical micelles were of varying lengths, from the length of two particles fused together at approx. 550nm up to multiple lengths of the base rod at approx. 2000nm .

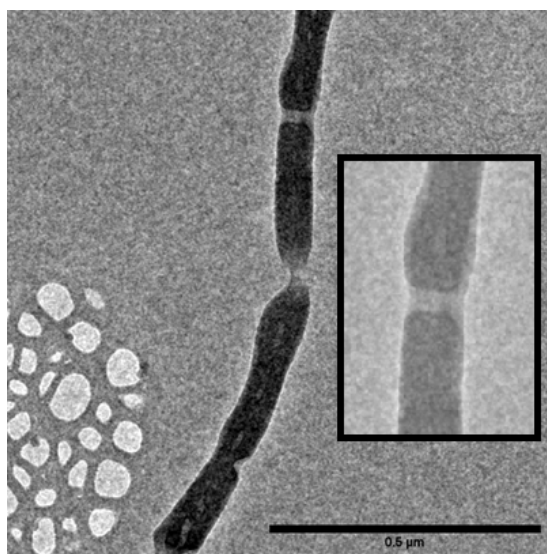


Figure 4.7: TEM micrographs of $S_{11} - F_{20}$ showing the fusion of the ellipsoidal particles to form 1D cylindrical micelles. Inset shows the fusion overlap between the outer walls of the particles. Scale bar = $0.5 \mu\text{m}$

Upon further chain extension, the cylinders were observed to open up, forming ellipsoidal micelles. This process was captured under TEM with certain particles being found in the 'closed' state, some in their 'opening' state and some in the fully 'open' state (Figure 4.8).

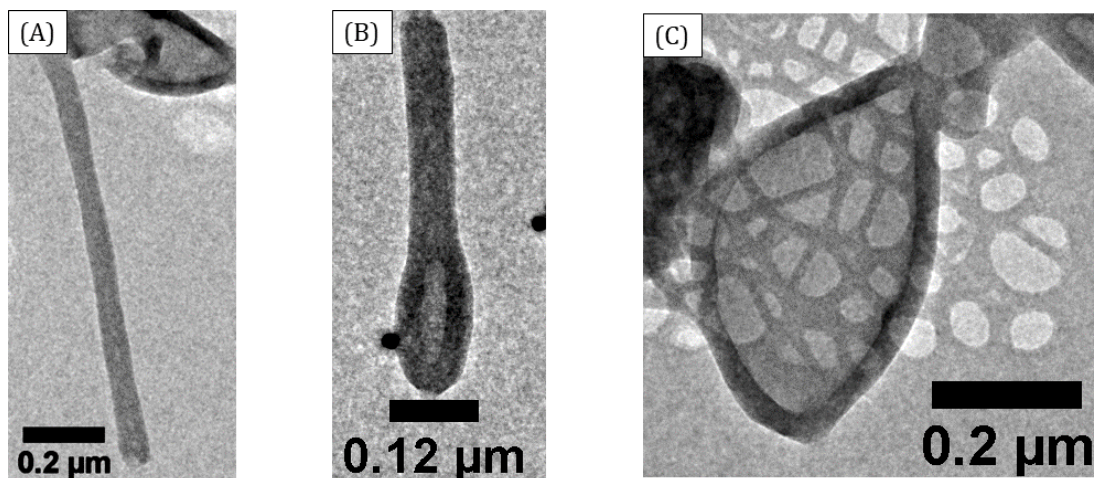


Figure 4.8: TEM micrographs of $S_{11} - F_{35}$ particles at different stages of the opening progress. (A) Fully closed cylinder. (B) Partially open cylinder ('needle eye'), (C) Fully open ellipsoidal vesicles (note, the holes in the background are from the holey carbon film the particles were suspended on).

Further chain extension of the fluorinated block leads to formation of amorphous vesicles in $S_{11} - F_{50}$. These particles present intermediate morphology between the simple vesicles and micelles to large compound vesicles (LCVs) found in $S_{11} - F_{75}$ and $S_{11} - F_{100}$. This intermediate structure was found to possess membrane of constant thickness at $35 \pm 1\text{nm}$, the same as in the case of shorter BCPs.

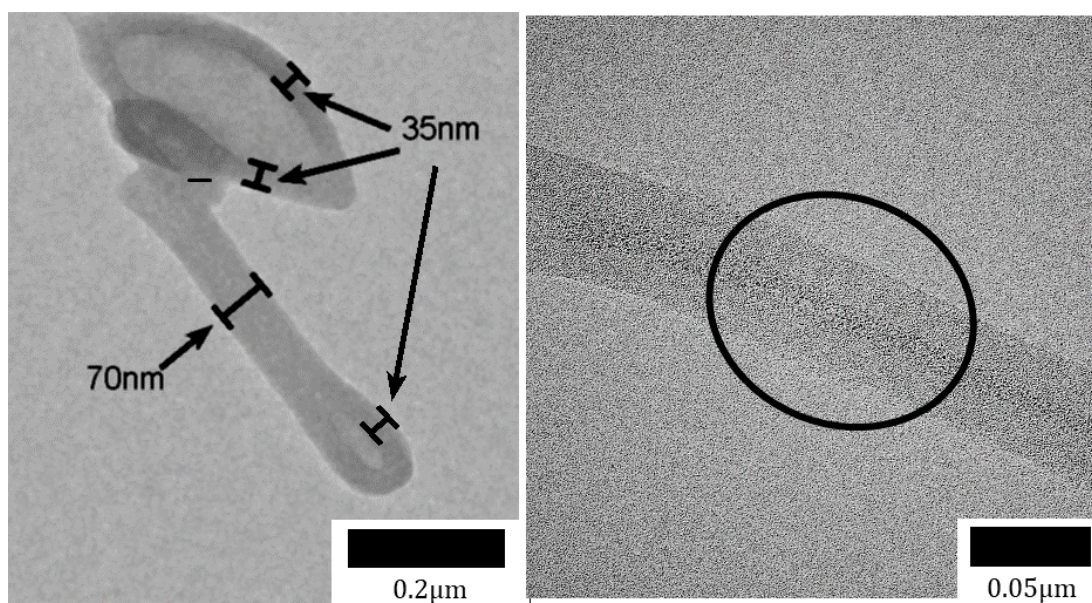


Figure 4.9: A TEM micrograph of (A) the $S_{11} - F_{50}$ nanoobjects with highlighted membrane thickness. (B) The membrane with its internal layer visible.

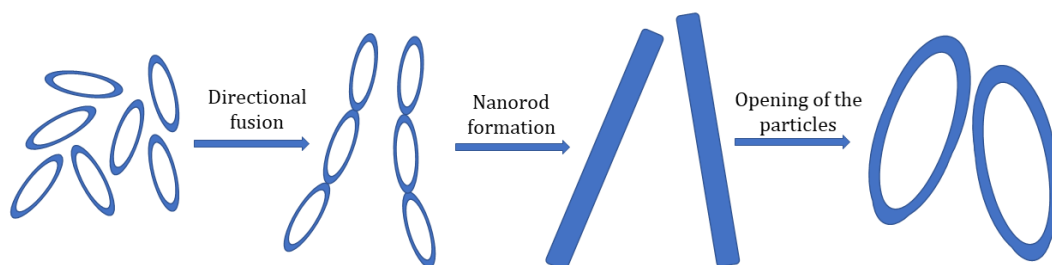


Figure 4.10: A schematic representation of the morphology evolution of $S_{11} - F_x$ block copolymer series.

Size and polydispersity evolution

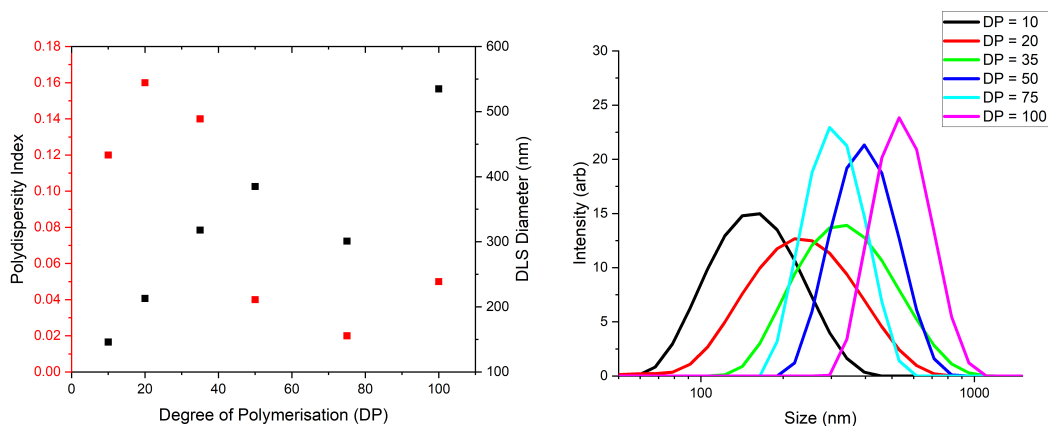


Figure 4.11: (a) Hydrodynamic radius (D_h) calculated for PStMA₁₀- FEOMA_x in n-dodecane at approx. 1% w/w. (b) The polydispersity index and the size distribution from DLS of the nanoobjects in n-dodecane at approx. 1% w/w. The DP corresponds to the degree of polymerisation of the FOEMA block.

The size and polydispersity of the particles were measured through dynamic light scattering (DLS) experiments. The diameter and the polydispersity index (PDI) of the particles was measured (Figure 4.11). PDI was found to remain relatively constant between 0.12 and 0.16 for BCPs at low DP (≤ 50). This relatively high BP indicates partial aggregation of the molecules and their non-spherical morphology, as indicated by TEM. The tendency of the molecules to aggregate can be ascribed to their non-minimal energy conformation given the ratios of the solvophilic to solvophobic blocks. This is further evident by the TEM images where the molecules are seen coming together in a linear manner. For longer BCPs, the PDI was found to have decreased significantly to between 0.05 and 0.02 at $DP \geq 50$. The size, as measured by DLS, was also found to increase steadily from 146nm for $S_{11} - F_{10}$ up to 535nm for $S_{11} - F_{100}$. The PDI drop is in part due to the change of the morphology of the particles to spherical. This change in the particle morphology from elliptical and linear to mostly spherical indicates the packing of the FOEMA group has changed.

Identifying liquid crystalline order in the PISA nanoobjects

The internal order of the membrane of $S_{11} - F_{35}$ was probed using wide-angle x-ray scattering (WAXS) experiments. All the samples were prepared at 1% w/w concentration by dilution with n-dodecane. An example of calculation of d-spacing is as follows:

$$q_{Bragg} = 2\text{\AA}^{-1} \quad (4.2)$$

$$d = \frac{2\pi}{q_{Bragg}} \quad (4.3)$$

$$d = \frac{2\pi}{2} \quad (4.4)$$

$$d = 3.14nm^{-1} \quad (4.5)$$

This calculation was used to determine the thickness and internal order of the membrane found in the nanoobjects. Two significant peaks were observed; one at $1.93nm^{-1}$ and one at $3.86nm^{-1}$. Their corresponding d-spacing was calculated to be 3.26nm and 1.63nm (Figure 4.12). The fully extended FOEMA group was modelled by GAMESS modelling package using STO-3G basis set.(Appendix A)^[110] The length of the mesogenic FOEMA molecule was found to be 1.59nm. Therefore the two peaks observed were assigned to the first and second order diffraction of smectic A phase.

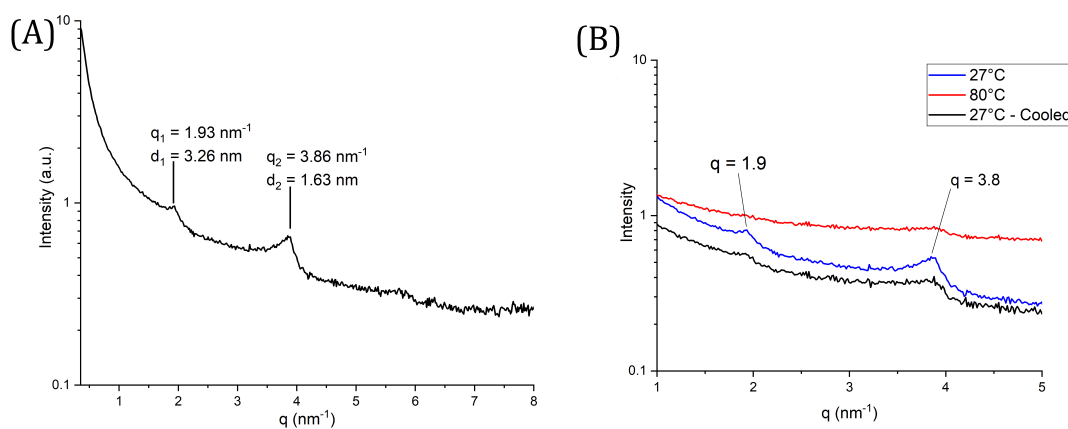


Figure 4.12: (A) A WAXS scattering pattern of $S_{11} - F_{35}$ measured at 1% in n-dodecane at room temperature. The d-spacing and q values of the peaks highlighted. (B) WAXS scattering pattern of $S_{11} - F_{35}$ measured at 27°C, 80°C and at 27°C again after cooling down. The peaks at $q = 1.8 \text{ nm}^{-1}$ and $q = 3.8 \text{ nm}^{-1}$ were found to disappear on heating past transition temperature and reappear on cool although more broad and weaker in intensity.

This indicates that the order of FOEMA side groups in the membrane is stacking side on in a linear fashion (Figure 4.13).

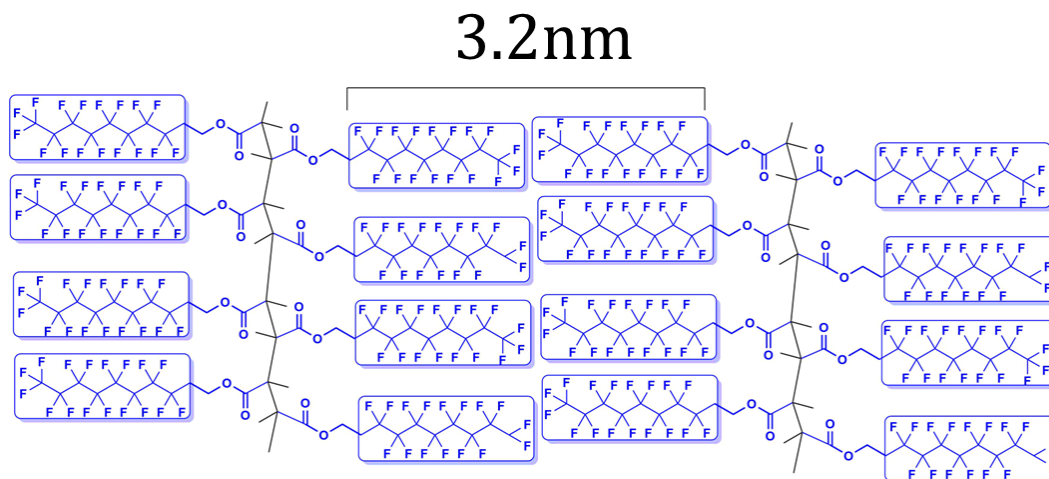


Figure 4.13: A schematic representation of the Smectic A order of PFOEMA side groups in the vesicular walls as indicated by the WAXS results.

Small-angle X-ray scattering

SAXS patterns were collected at synchrotron sources at ESRF, station ID02, Grenoble, France and Diamond Light Source, station I22, Didcot, UK using monochromatic X-ray radiation (wavelength, $\lambda = 0.124$ nm, with q ranging between 0.015nm^{-1} to 1.3nm^{-1}). The samples were diluted to 1% in n-dodecane and placed in 1.5mm quartz capillaries. The capillaries were then sealed with wax or epoxy to minimise contamination and exposure to the atmosphere. The data collected in Diamond was then reduced and background subtracted using DAWN software provided by Diamond Light Source^[111]. The data collected at ESRF was reduced using SAXSutilities2^[112] and subsequently fitted with Irena package for Igor Pro^[113].

The gradient in the low q region was calculated in order to identify the morphology of the particles based on the Guinier approximation (Equation 2.10). All of the measured particles had a gradient of approximately -1. This gradient corresponds to rods or first approximation to wormlike nanoparticles. The TEM images of $S_{11} - F_{10}$, $S_{11} - F_{20}$ and $S_{11} - F_{35}$ support these morphologies however for the longer molecules, these gradients appear to correspond to different than

observed morphologies. While this determination is at odds with the nanoparticles observed under TEM, these particles were observed in solution potentially avoiding the drying artifacts in the TEM where the molecules tend to settle on the surface due to more favorable interactions between the blocks.

The fitting of appropriate models to the nanoobjects was only successful for some of the particles. This is due to either a mixture of morphologies being present in the sample or no appropriate models being available for the structures.

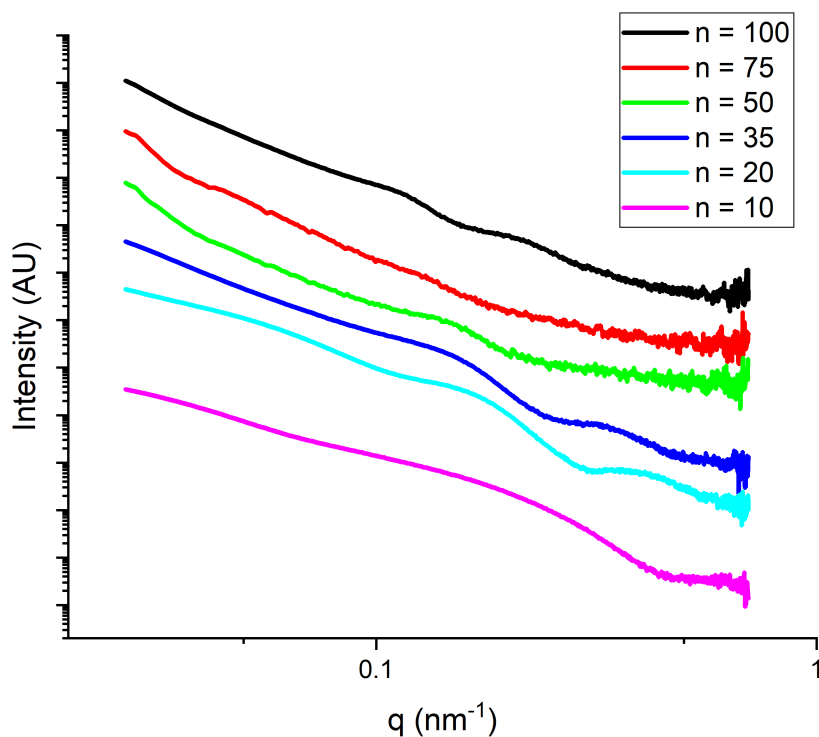


Figure 4.14: Small-angle X-ray scattering (SAXS) patterns recorded for a 1.0% w/w dispersion of $S_{11} - F_n$ nanoparticles in n-dodecane. The individual spectra have been offset in the intensity y-axis in order to not overlap.

For vesicles the degree of polymerisation of the membrane-forming block is related to the membrane thickness (T_m) by a scaling relationship $T_m = kx^a$

where x is the degree of polymerisation, k is a constant related to Flory-Huggins interaction parameter and a is a scaling exponent that is determined by the conformation of the membrane-forming chains.^[88,114] Plotting this for the low DP of PStMA₁₀-b-PFEOMA _{n} systems which possess vesicular walls (Figure 4.15) gives the x value at 0.49 which indicates the chains are tightly packed inside the membrane. A similar result is observed for the nanoobjects sizes as a function of degree of polymerisation of FEOMA block in DLS experiments. While the x value is higher at 0.62, the value still indicates tightly packed core block.

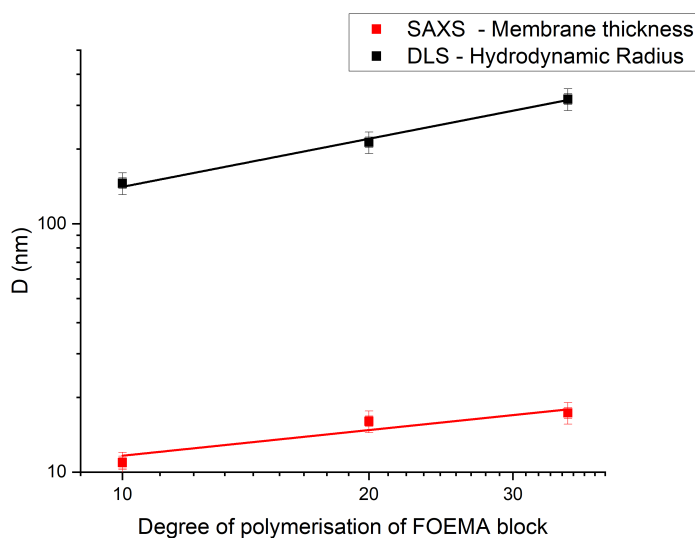


Figure 4.15: Fitting of $T_m = kx^a$ to the membrane thickness calculated from SAXS for the $S_{11} - F_n$ series and the hydrodynamic radius (D_h) calculated from DLS.

Optical characterisation of the LC properties of $S_{11} - F_n$ nanoobjects.

In order to further characterise the liquid crystalline order within $S_{11} - F_n$ nanoobjects, polarised optical microscopy experiments were performed on the samples. The experiments were performed on both, the bulk BCPs as well as the nanoobjects in solution.

The nanoobjects in solution were fully isotropic regardless of temperature. No discernible features were observed upon either heating or cooling past the

transition temperatures identified in DSC experiments (Figure 4.16).

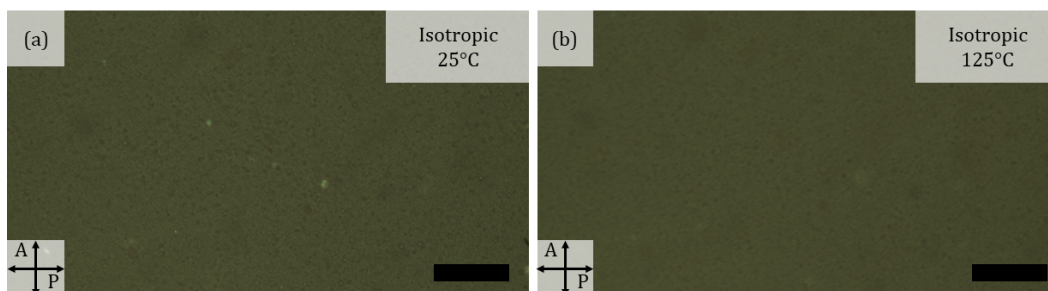


Figure 4.16: Polarised optical microscopy (POM) images of the $S_{11} - F_{35}$ in 15% w/w in n-dodecane at (A) 25°C and (B) 125°C. Samples were held in between cover slips with no alignment layers. Magnification = 20x The solution remained isotropic and no textures or otherwise were observed. Black scale bar = 500 μm .

The bulk material was found to form birefringent textures under POM. As is often the case with polymers, the samples were difficult to align. Using multiple different PIs and cell thickness resulted in unaligned textures making it difficult to identify the phases present. A partially successful attempt at aligning the sample was made and the textures observed under POM were identified as Smectic A textures (Figure 4.17(B)). The textures only occasionally formed upon rapid heating of 10 km^{-1} making it difficult to pinpoint exact transition temperature which varied based on the thermal history of the sample.

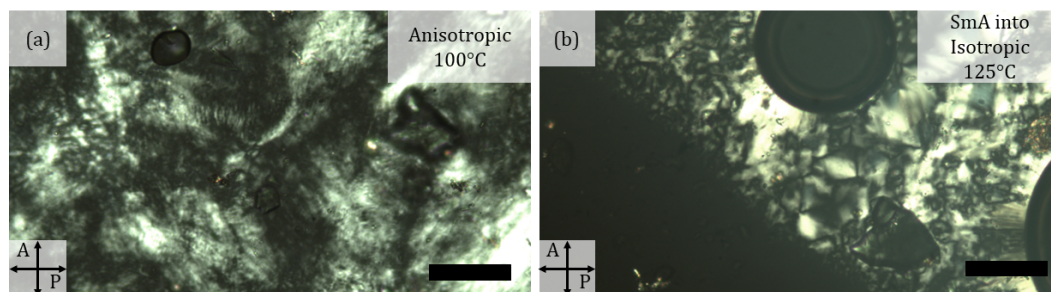


Figure 4.17: Polarised optical microscopy (POM) images of bulk $S_{11} - F_{35}$ at (A) 100°C and (B) 150°C. Samples were held in between cover slips with no alignment layers. Magnification = 20x. The texture of Smectic A observed in (B) was short lived only forming on rapid heating at a rate of 10 kmin^{-1} . Black scale bar = $500 \mu\text{m}$.

4.4.3 Summary of results

This chapter provides an examination of the self-assembly behaviour of $S_{11} - F_n$ block copolymer series. In this study, a clear morphological evolution was described. A unique linear fusion of particles was observed with individual building rods coming together to form 1D nanocylinders. The 1D nanocylinders were then observed to be further opening up into ellipsoidal vesicles with uniform membranes across different chain lengths. Large compound vesicles were identified present in the longest BCPs, feature not seen before in similar systems. This investigation verifies findings reported for the perfluorinated mesogens in literature. It also expands on self-assembly evolution reported by identifying and explaining the key interactions that drive said processes. X-ray scattering studies have confirmed liquid crystalline order in the membranes. The LC phase was identified as Smectic A phase based on the d-spacing values calculated from WAXS data and by correlating with it data modelled using chemical simulation package. SAXS data indicates formation of ellipsoidal and one dimensional structures across the different chain lengths. POM images confirm presence of LC phase in bulk material albeit difficult to align using common alignment methods. While no birefringent textures were observed for the nanoobjects suspensions, this was to be expected as the volume of the actual liquid-crystal groups within the system were too low to be observed even for some of the best lyotropic LCs.

Chapter 5

Liquid-crystalline behaviour of the polymethacrylate block copolymers bearing cholesterol and cyanobiphenyl side chains

5.1 Introduction

In this chapter, the liquid crystalline properties of a series of methacrylic monomers, homopolymers and copolymers bearing a side chain cholesteryl and/or cyanobiphenyl mesogens will be discussed. The polymerisation-induced self-assembly (PISA) behaviour will be discussed.

5.2 Cholesteryl and cyanobiphenyl liquid crystals

As mentioned in section 1, liquid crystals bearing cyanobiphenyl mesogens are some of the most academically and industrially relevant. Cholesteryl-based liquid crystals are some of the oldest known liquid crystals that possess a chiral nematic phase. They possess many unique properties such as biocompatibility and selective reflection within the visible range making them suitable for applications within

biomedicine and related fields.

5.3 Synthesis

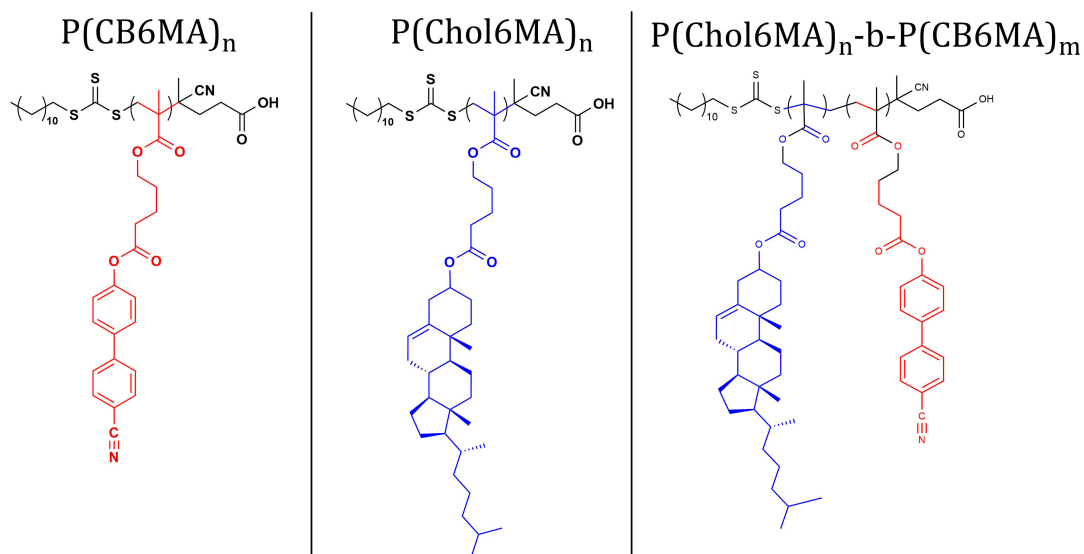


Figure 5.1: Molecular structures of homopolymers of PChol6MA, PCB6MA and block copolymer of PChol6MA-b-PCB6MA.

In this section, the synthetic pathways for the preparation of the monomers and polymers will be described in brief to describe the conditions and issues associated with these particular reactions. An in depth explanation of the synthetic pathways can be found in section 3.3. All of the synthesis was performed with materials as described in section 2.3.1.

5.3.1 Synthesis of monomers

Monomers were synthesised through methods described in section 3.3.

Synthesis of Chol-6-MA

This synthesis involved two steps, firstly Cholesterol was reacted with hexanoyl chloride to afford an intermediate, Chol-6-Br. This material was then used to prepare Chol-6-MA through esterification with potassium methacrylate.

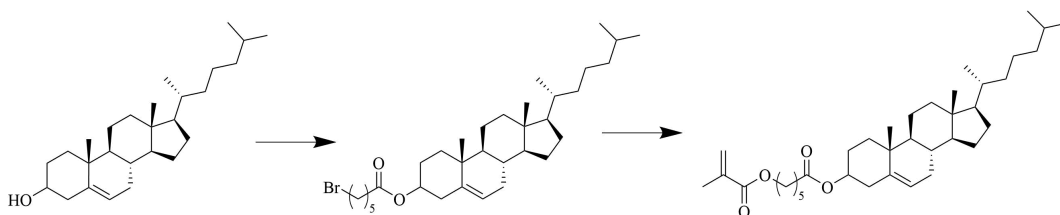


Figure 5.2: Molecular structures of the starting material, intermediate and the end product of Chol-6-MA

5.3.2 Synthesis of homopolymers

A typical synthesis for homopolymers went as follows: a 10ml round-bottom flask was charged with 6-CB-MA (500mg, 1.32mmol), 4-Cyano-4-[(dodecylsulfanylthiocarbonyl)sulfanyl]pentanoic acid (CTA, 10.7mg, 0.026mmol), (target degree of polymerisation = 50), 2,2'-azobisisobutyronitrile (AIBN, 0.9mg, 0.006mmol added from a freshly prepared stock solution prepared in anisole, [AIBN]:[CTA] = 2) and anisole (2000mg). The flask was sealed with a septum and purged with N_2 gas for 30 minutes. Sample was then placed in a hot-oil bath at 80°C for 5 hours. The resulting PCB-6-MA was precipitated against excess methanol. The mean DP was calculated to be 45 by comparing the integral signals of the CTA and CB-6-MA in ^1H NMR.

This method was used for preparation of all of the homopolymers. Summarised results can be seen in table 5.1.

Table 5.1: Summary for the synthesis of homopolymers of CB-6-MA. The target DP, calculated DP and GPC molecular weights for the two polymers prepared by RAFT polymerisations of CB-6-MA in anisole at 80°C using AIBN and CTA. Solids % = 15%, [AIBN]:[CTA] = 2

Target DP	Calculated DP ^a	$M_n/gmol^{-1b}$	$M_w/gmol^{-1b}$	M_w/M_n^b
PCB6MA ₅₀	45	18.8k	22.1k	1.17
PCB-6MA ₁₀₀	101	40.1k	52.5k	1.31
PChol6MA ₅₀	49	27.5k	32.7k	1.19

hline ^a - Calculated using ¹H NMR, ^b - Determined from THF GPC.

hline

5.3.3 Synthesis of copolymers

In order to prepare the copolymers and afford a good self-assembly of the polymers via PISA, multiple different solvents and concentrations as well as the order of synthesis of each of the blocks was tested. The key parameter for a successful PISA synthesis is the transition of the reaction solution from clear (i.e. fully dissolved) to opaque. This visual indicator was used to identify quickly which reaction conditions resulted in successful PISA procedure. Multiple solvents were used; including ethanol, anisole, n-dodecane and methanol. For reactions of chain extending the PChol-mCTA with CB-6-MA, only n-dodecane was shown to be effective. Reactions with the other three solvents showed little to none opaqueness, even after prolonged polymerisation reactions. The completeness of the polymerisation were confirmed through ¹H NMR where the vinyl peaks at approx. 5.5 and 6.0ppm were found to have disappeared, indicating full consumption of the monomers and complete polymerisation. Anisole was found to be an effective solvent for polymerisation of homopolymer mCTAs but of little use for PISA as it would completely dissolve both of the blocks. Resulting polymers and their DP are summarised in Table 5.2. Due to limited solubility of the BCPs in GPC solvents, the PDI and molecular weights could not be obtained.

5.4 Liquid crystalline behaviour

Table 5.2: Summary for the synthesis of copolymers of Chol6MA and CB-6-MA. The target DP, calculated DP and GPC molecular weights for the two polymers prepared by RAFT polymerisation of CB-6-MA in anisole at 80°C using AIBN and CTA. Solids % = 15%, [AIBN]:[CTA] = 2

Target DP	Calculated DP ^a
PChol6MA ₅₀ -b-PCB6MA ₅₀	55
PChol6MA ₅₀ -b-PCB6MA ₁₀₀	100
PChol6MA ₅₀ -b-PCB6MA ₁₅₀	122

^a - Calculated using ¹H NMR.

5.4 Liquid crystalline behaviour

5.4.1 Intermediates

The liquid crystalline properties of the intermediate materials were characterised using DSC and POM.

CB-6-Br

CB-6-Br was prepared by reacting 6-hexanoyl chloride with 4'-Hydroxy-4-biphenylcarbonitrile in anhydrous conditions. CB-6-Br was purified by recrystallisation. CB-6-Br was found to possess an enantiotropic nematic phase that was supercooled to room temperature (Figure 5.3).

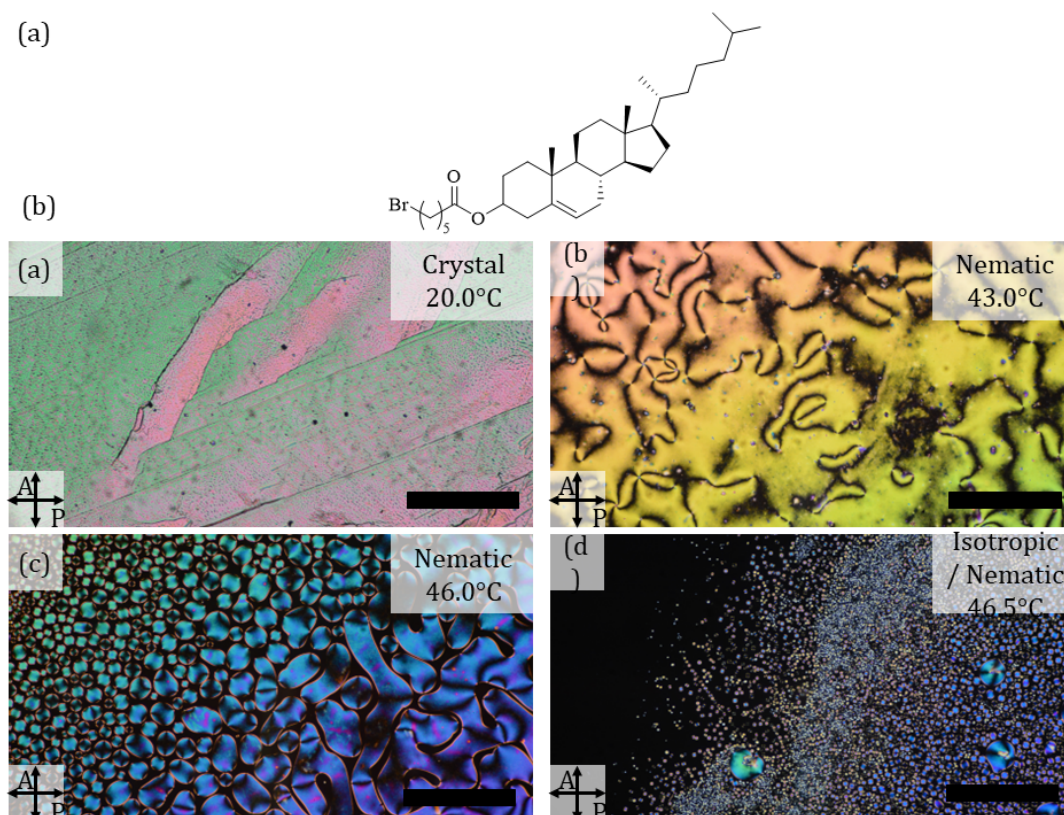


Figure 5.3: (a) Chemical structure of Chol-6-Br. (b) POM image of Chol-6-Br taken in a cover slip with no alignment layer on heating. Transmission mode, 20x magnification. Black scale bar = 500 μ m.

5.4.2 Monomers

Chol-6-MA

The DSC scans of the pure cholesterol monomers were performed at various temperature rates (Table 5.3). Just as before, two transitions were observed in the cooling runs. There was a higher energy transition, corresponding to the clearing temperature. The temperature is slightly lower than observed under POM (57°C) however it is common for the POM and DSC transition temperatures to be offset relatively to each other. The lower temperature transition, under POM corresponds to transition from LC to solid state. The temperature is close to

5.4 Liquid crystalline behaviour

Table 5.3: Table summarising the DSC transition temperatures and enthalpies for cooling runs of Chol-6-MA

		Transition 1		Transition 2	
	Repeat	Onset Temp (°C)	Enthalpy of Change (J/g)	Onset Temp (°C)	Enthalpy of Change (J/g)
10K min ⁻¹	1	55.09	1.1950	25.64	0.0808
10K min ⁻¹	2	55.07	1.2080	25.66	0.0797
10K min ⁻¹	3	55.08	1.1970	25.70	0.0782
10K min ⁻¹	4	55.08	1.2140	25.62	0.8276
10K min ⁻¹	5	55.07	1.2080	25.64	0.8233
5K min ⁻¹	1	55.10	1.4010	26.59	0.1515
5K min ⁻¹	2	55.10	1.3620	26.31	0.1502
5K min ⁻¹	3	54.67	1.4220	26.11	0.1385
5K min ⁻¹	4	55.08	1.3040	26.36	0.1373
5K min ⁻¹	5	55.08	1.3400	26.42	0.1525
1K min ⁻¹	1	55.10	1.2050	28.13	0.2346
1K min ⁻¹	2	55.09	0.9644	25.81	0.1394
1K min ⁻¹	3	55.08	0.9213	27.18	0.1543
1K min ⁻¹	4	55.06	0.7253	28.47	0.1112
1K min ⁻¹	5	55.04	0.7114	28.90	0.0151

the one observed under POM at 25°C. Both enthalpies and temperatures do not appear to be influenced by the cooling rate at the 10Kmin⁻¹ and 5Kmin⁻¹ rates as it does not appear to be changing significantly. However, at 2Kmin⁻¹, there appears to be a significant change in the sample. The high temperature peak appears to be decreasing in intensity with the enthalpy of change dropping significantly, going from 1.2J/g down to 0.71J/g (41% decrease). The lower temperature transition also experiences a significant decrease in the enthalpy of change, decreasing by 94% from 0.23J/g to 0.01J/g. As the peak appears to weaken in intensity, it also appears to split into two individual peaks. This could imply that there are two individual transitions which are not being resolved at higher cooling rates and could be resolved at lower ones (e.g 1Kmin⁻¹ or less). A more likely explanation for this is that during the slower cooling rates, the sample is provided with enough energy and enough time to start polymerising. The polymerisation reaction is usually associated with a release of energy (exothermic) which should be observable under the DSC. This appears to be the case as a third peak was observed forming at approximately 80°C. This peak cannot be fully resolved as it is close to the end of the run and therefore a baseline before and after cannot be established however it appears only in the slower cooling

5.4 Liquid crystalline behaviour

runs (2Kmin^{-1}) and would likely correspond to the dimerisation and eventually complete polymerisation of the sample.

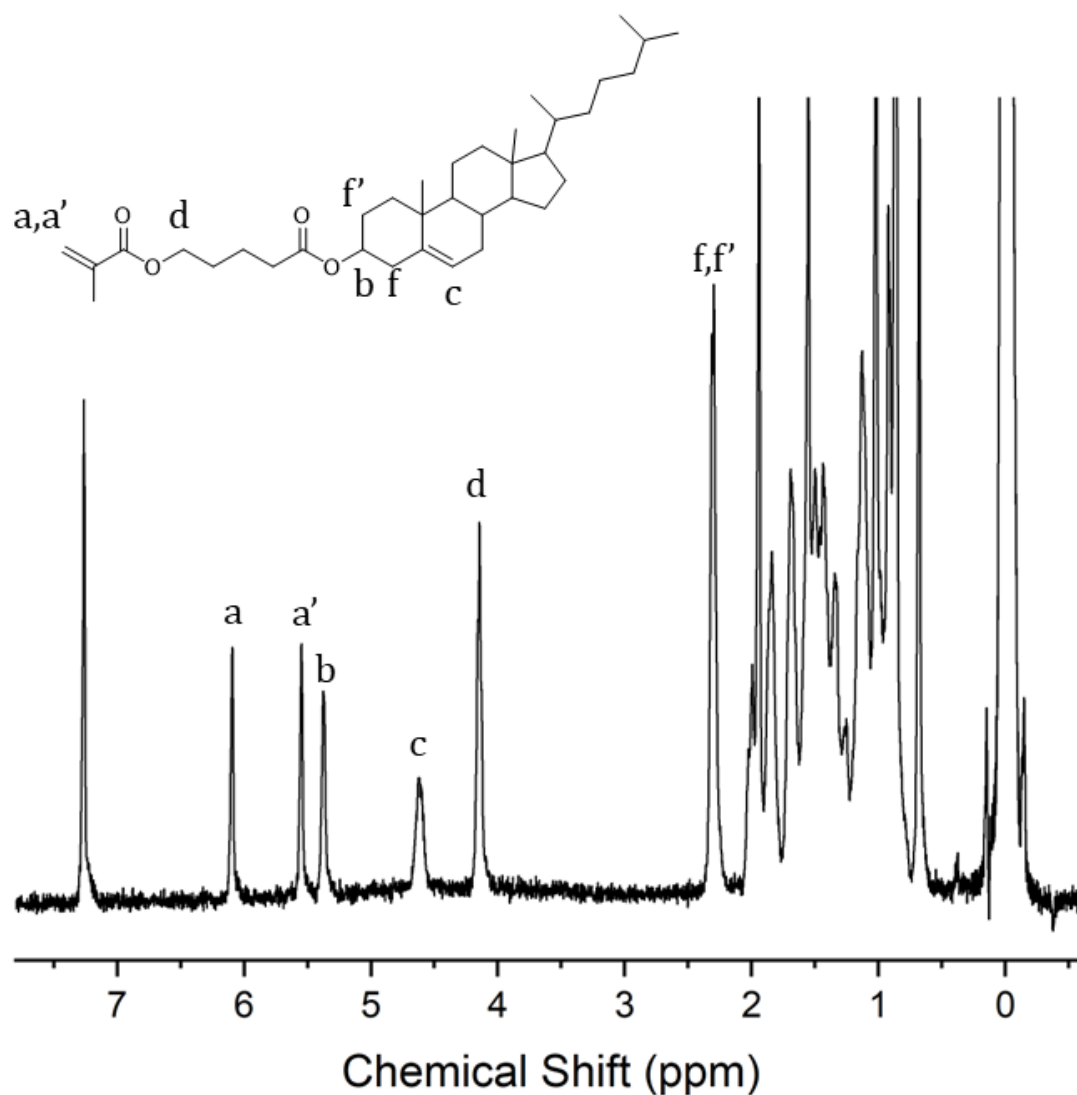
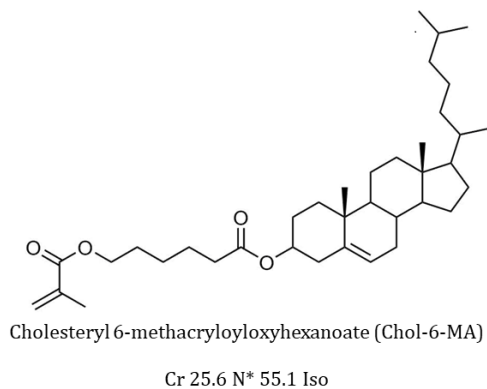


Figure 5.4: ^1H NMR spectrum of Chol-6-MA with chemical structure and atom assignment. Values: ^1H NMR (CDCl_3): 0.65–2.1 (50H, m, CH,CH₂,CH₃), 2.30 (4H, m, CH₂), 4.13 (2H, t, J 5 6.7 Hz, CH₂), 4.60 (1H, m, CH), 5.37 (1H, m), 5.53 (1H, m), 6.08 (1H, bs)

5.4 Liquid crystalline behaviour

Birefringent textures of the sample were observed under POM under cover slips. On first heating in transmission mode, two clear transitions were observed. (Figure 5.5) The sample was first melted on a cover slip and allowed to cool down overnight. The texture observed in the solid on the cover slip was of a highly birefringent. The first transition was observed at 26.0°C (Figure 5.5(b)) where sample melted into a liquid crystalline phase. The texture observed appears to be a tightly packed oily streak texture which at higher temperature diffuses slightly before the clearing point. This phase was observed between 26.0°C and 57°C and it was largely unchanged, except for the colour change. At approx. 46°C the colour in between the oily streak texture was mostly gone, suggesting the pitch was now outside the visible spectrum.

(a)



(b)

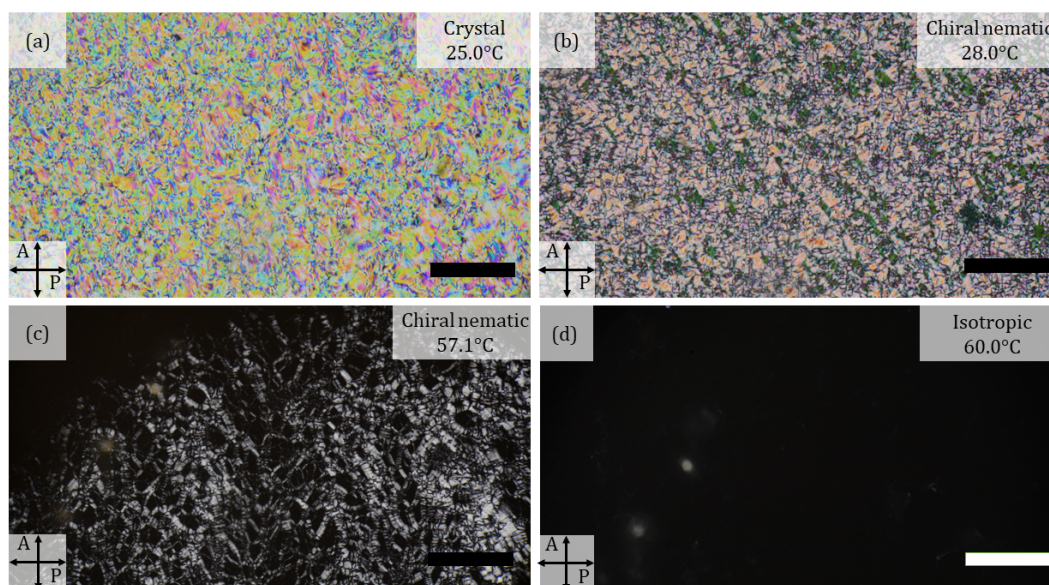


Figure 5.5: (a) Chemical structure and phase sequence of Chol-6-MA. (b) POM image of Chol-6-MA taken in a cover slip with no alignment layer on heating. Transmission mode, 20x magnification, scale bar = 500 μ m

On cooling, there was a significant difference in the transition temperatures. Starting at 60°C, the sample was gradually cooled down until a change in the texture was observed. No change was observed until 44.8°C where small clusters of

5.4 Liquid crystalline behaviour

birefringence were observed. These were allowed to grow until entirely filling the camera screen. This process took approx. 6 minutes at a constant temperature of 44.8°C (Figure 5.6). This roughly corresponds with the disappearance of the colour observed on heating. On further cooling, a change in the birefringence was observed at 24.4°C. Below this transition, the sample was solid and did not flow. The texture was largely unchanged below this temperature except for minor changes in the colour intensity under the POM. These values are in line with the values obtained from the DSC experiments. In both sets of experiments, only two transitions are observed. From the DSC both transitions appear 1st order indicating formation of a crystalline phase below 25°C, LC phase below 55°C and isotropic above (using DSC values). The slight difference between values observed in POM vs DSC is to be expected the DSC values in this case are more likely to be accurate on cooling as the chiral nematic phase pitch does not enter the visible regime until approx. 44°C making it difficult to pinpoint using simple POM techniques.

5.4 Liquid crystalline behaviour

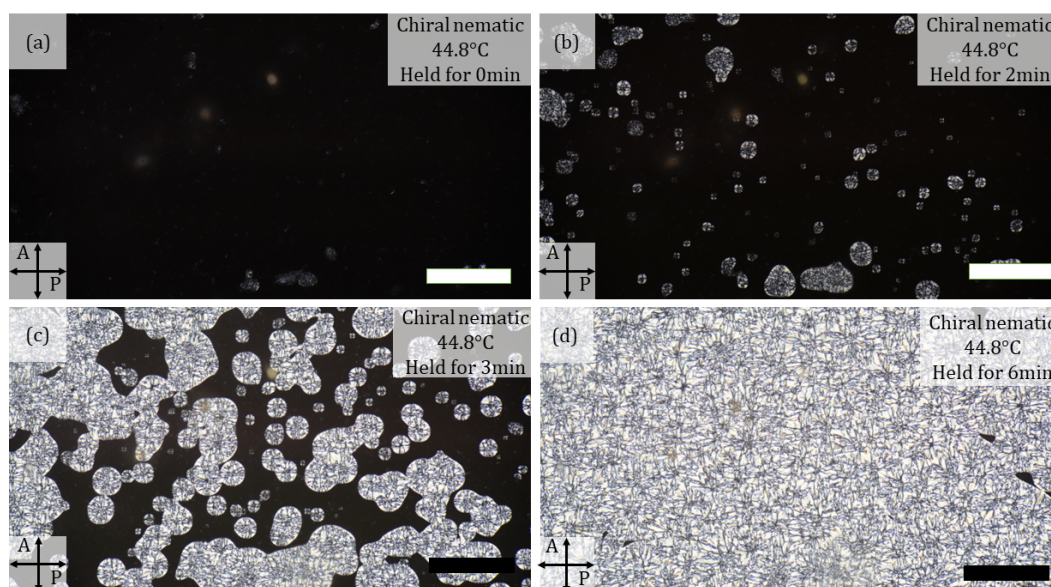


Figure 5.6: POM image of gradual phase transition of 6-(Methacryloyloxy)hexanoic acid 3-cholesteryl ester (Chol-6-MA) taken in a cover slip with no alignment layer held at 44.8°C for (a) 0 min, (b) 2min (c) 3min and (d) 6min after cooling from isotropic at rate of 5Kmin^{-1} . Transmission mode, 20x magnification. Scale bar = $500\mu\text{m}$.

A 5 μm HG and HT cells were filled with Chol-6-MA. Both were then investigated using POM. The planer cell showed clear oil streak textures associated with chiral nematic phase. The colour observed also changed depending on temperature (Figure 5.7). As previously observed with samples under a cover slip the colour disappears at approx. 44°C on heating however the oily streaks remain until clearing point at 56°C. On cooling, the birefringence appears to form at 54°C however it is a slow process. Holding the sample at a constant temperature for an hour at 54°C results in a very slight formation of birefringent texture. In general the transition temperatures were similar to those observed under the cover slips and in the DSC.

5.4 Liquid crystalline behaviour

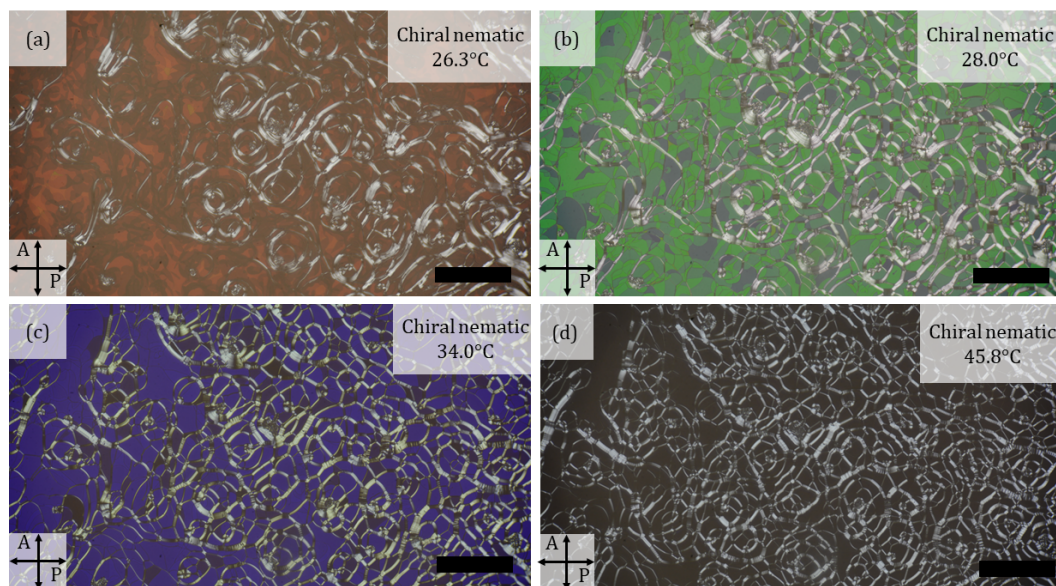


Figure 5.7: POM image of gradual colour changed of Chol-6-MA taken in a $5\mu\text{m}$ cell with planar alignment (a) 26.3°C , (b) 28.0°C (c) 34°C and (d) 45.8°C after cooling from isotropic at rate of 5Kmin^{-1} . Transmission mode, 20x magnification. Scale bar = $500\mu\text{m}$.

A UV-VIS spectroscopy measurements were taken to quantify the wavelength of the selective reflection as a function of temperature of Chol-6-MA (Figure 5.8) The measurements were taken at a constant cooling rate of 1Kmin^{-1} .

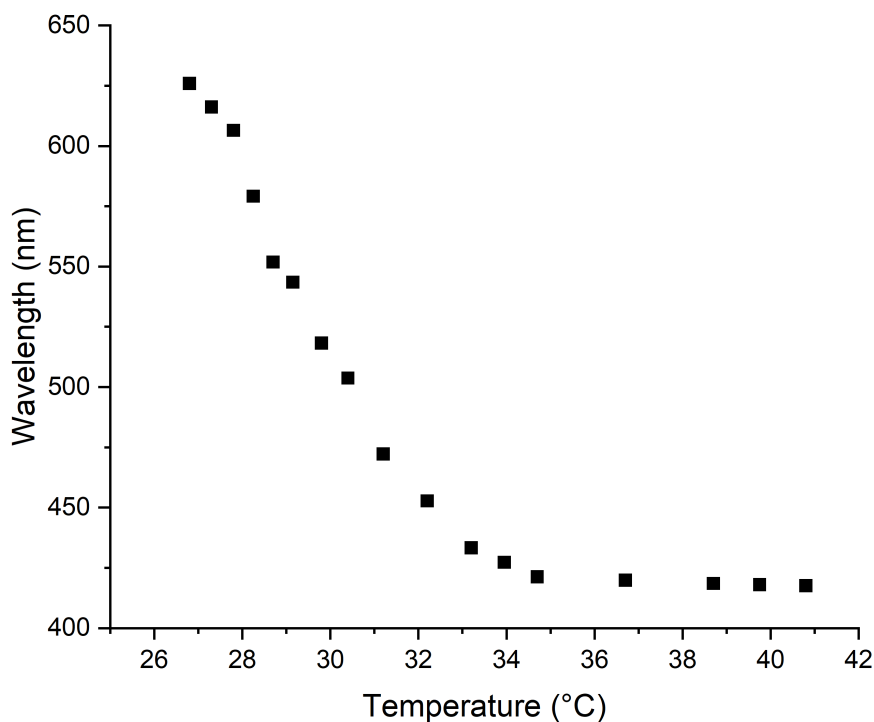


Figure 5.8: Peak selective reflection wavelength of Chol-6-MA monomer as a function of temperature recorder with a UV-Vis Spectrometer connected to a reflection microscope in a $5\mu\text{m}$ cell with planar alignment.

CB-6-MA

6-(4-Cyano-biphenyl-4'-yloxy)hexyl methacrylate (CB-6-MA) was synthesised in the same way as Chol-6-MA. This material did not display any liquid crystalline behaviour. DSC confirmed a single first order transition at 62.8°C on cooling. This corresponded to the isotropic to crystalline transition as further confirmed under POM. This was unexpected as both the intermediate before the addition of methacrylic group and the homopolymer of this material possess liquid crystalline phase.

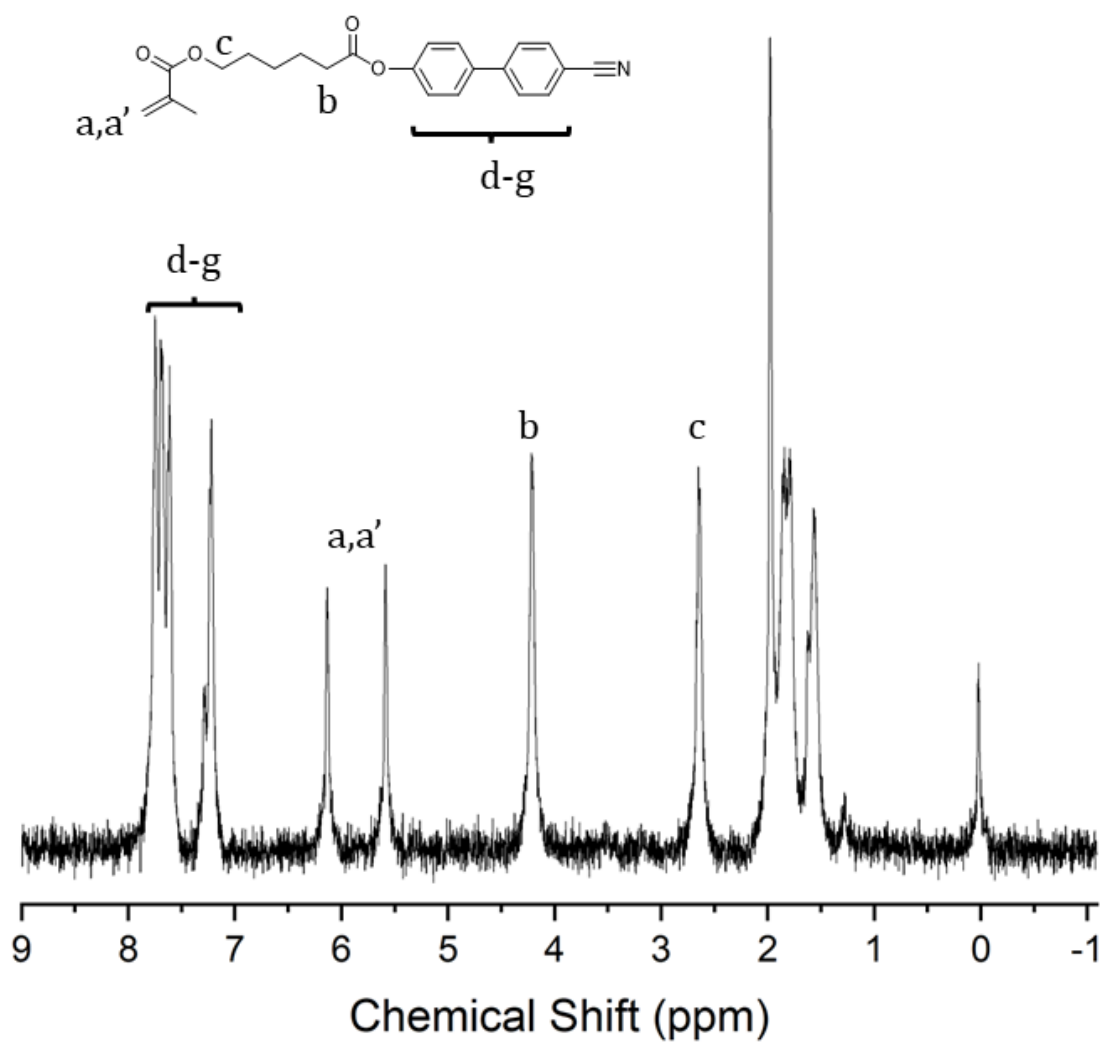


Figure 5.9: ¹H NMR spectrum of CB-6-MA with chemical structure and atom assignment. Values: ¹H NMR (CDCl₃): 1.4-2.1 (9H, m, CH, CH₂, CH₃), 2.6 (2H, t, CH₂), 4.2 (2H, t, CH₂), 5.6 (1H, m), 6.1 (1H, m), 7.0 - 8.0 (8H, m, aromatic)

5.4.3 Homopolymers

Homopolymers of the CB-6-MA and Chol-6-MA were prepared based on different DPs (5.1). The homopolymers of CB-6-MA

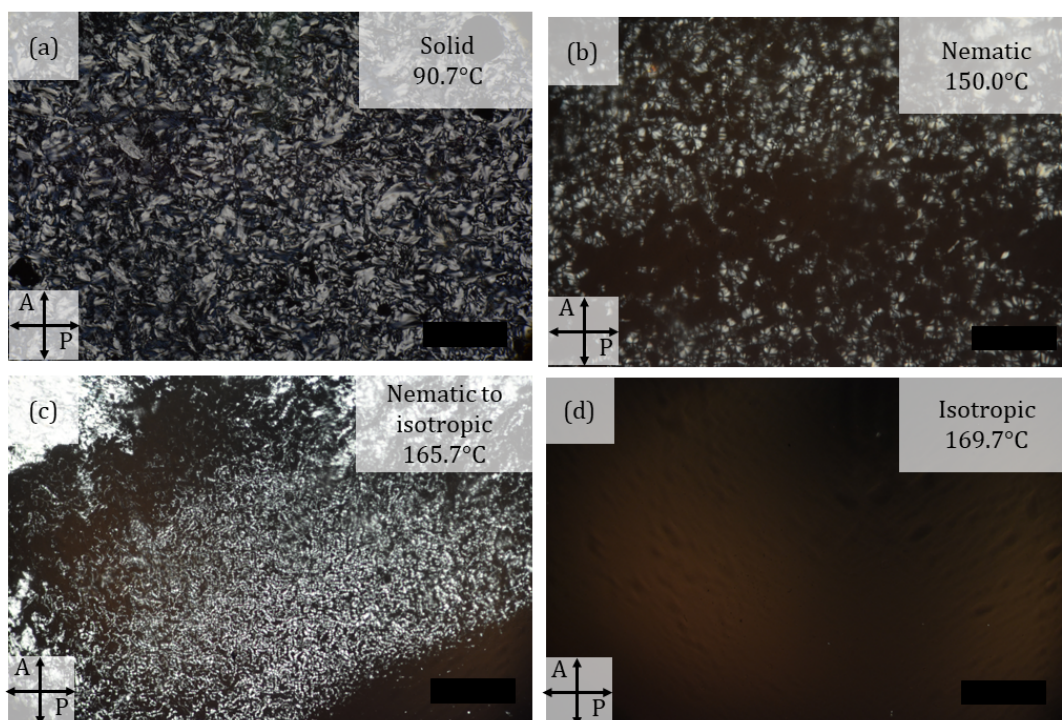


Figure 5.10: POM images of $PChol_{50}$ taken in between unaligned cover slips (a) 90.7°C , (b) 150.0°C (c) 165.7°C and (d) 169.7°C after cooling from isotropic at rate of $5\text{km}\text{in}^{-1}$. Transmission mode, 20x magnification. Scale bar = $500\mu\text{m}$.

5.4 Liquid crystalline behaviour

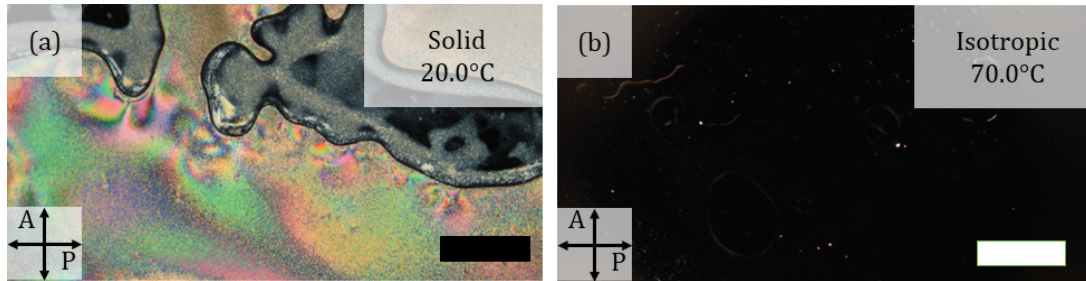


Figure 5.11: POM images of $PCB - 6 - MA_{50}$ taken in between unaligned cover slips (a) 20°C , (b) 70°C after cooling from isotropic at rate of 10kmin^{-1} . Transmission mode, 20x magnification. Scale bar = $500\mu\text{m}$.

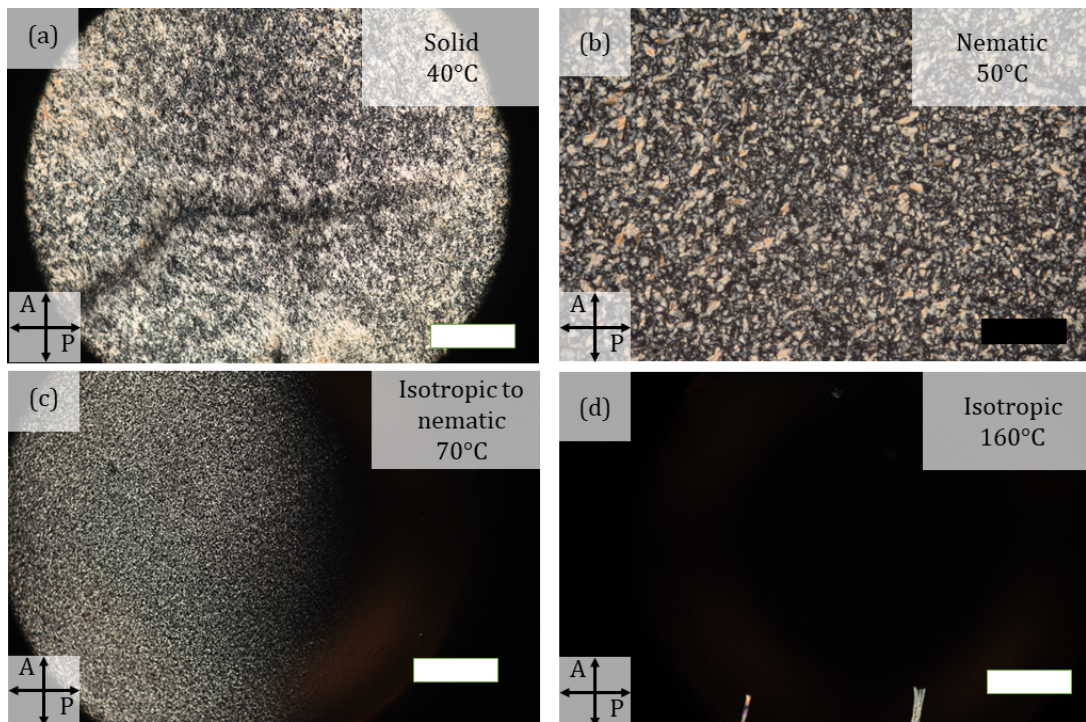


Figure 5.12: POM images of $PCB - 6 - MA_{100}$ taken in between unaligned cover slips (a) 40°C , (b) 50°C , (c) 70°C and (d) 160°C after cooling from isotropic at rate of 10kmin^{-1} . Transmission mode, 20x magnification. Scale bar (b) = $500\mu\text{m}$, (a)(c)(d) = $1000\mu\text{m}$.

5.4 Liquid crystalline behaviour

Table 5.4: A list of copolymers of P(Chol-6-MA)-b-P(CB-6-MA) prepared via RAFT polymerisation in n-dodecane. Values for transition temperatures and enthalpy of change obtained from DSC performed at 5Kmin^{-1} . T_{N-I} - Nematic to isotropic phase transition, T_{N-C} - nematic to solid phase transition.

Polymer	Target degree of polymerisation of 6-CB-MA	T_{N-I}	ΔH	T_{N-C}	ΔH
P1	50	148.18	2.82	No Peak	No Peak
P2	100	144.03	1.22	98.38	1.81
P3	150	159.93	1.25	98.17	1.50

5.4.4 Copolymers

Three copolymers of P(Chol-6-MA)-b-P(CB-6-MA) moiety were synthesised. These are summarised in Table 5.4. All three copolymers displayed liquid crystalline properties under POM (Figures 5.13-5.15). The liquid crystalline order was probed using POM and DSC in custom made cells. The cells were made using ITO glass aligned with SE130 PI with $30\mu\text{m}$ spacer film. Polymeric LCs tend to have viscosity orders of magnitude higher compared to LMWLCs, making alignment more difficult.^[115] As such, extra measures were taken to improve the alignment of the materials within the cells. First, the samples were drop filled into cells as the material was too viscous to capillary fill over an acceptable time frame. Once filled, the materials were heated above and below the isotropic transition temperature multiple times over a course of approx. 2h for each of the cells. This was done in order to release any kinetically trapped sections of the sample in the cell. Lastly, the materials kept at isotropic for 20minutes before any images were taken in order to ensure samples had enough time to reach an equilibrium. Even with these precautions full alignment was not achieved.

5.4 Liquid crystalline behaviour

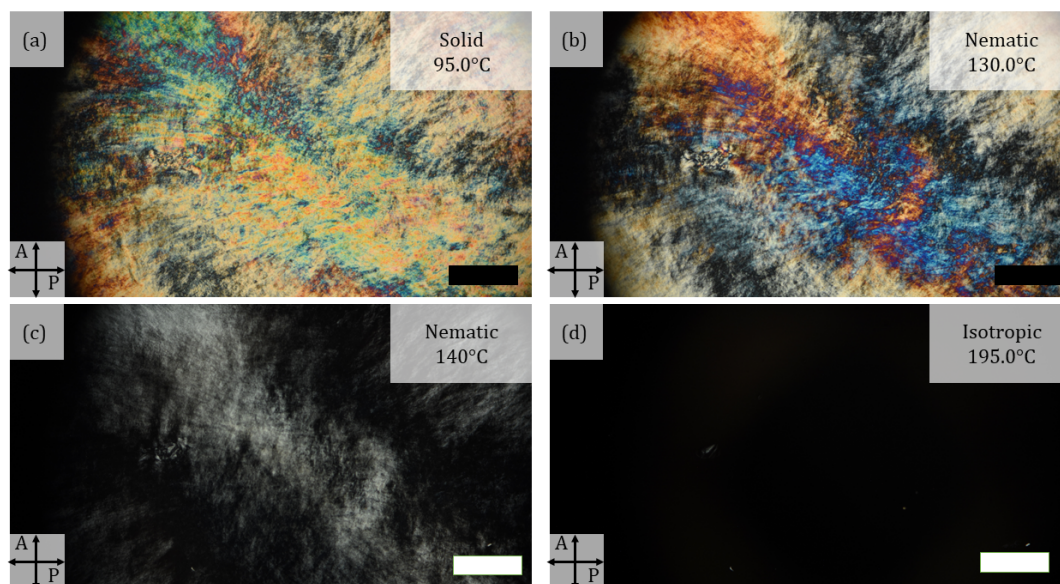


Figure 5.13: POM images of $PChol_{50} - b - PCB_{50}$ taken in a $27.9\mu\text{m}$ cell with planar alignment (a) 95.0°C , (b) 130.0°C (c) 140.0°C and (d) 195.0°C after cooling from isotropic at rate of $2.5\text{km}\text{in}^{-1}$. Transmission mode, 20x magnification. Scale bar = $500\mu\text{m}$.

5.4 Liquid crystalline behaviour

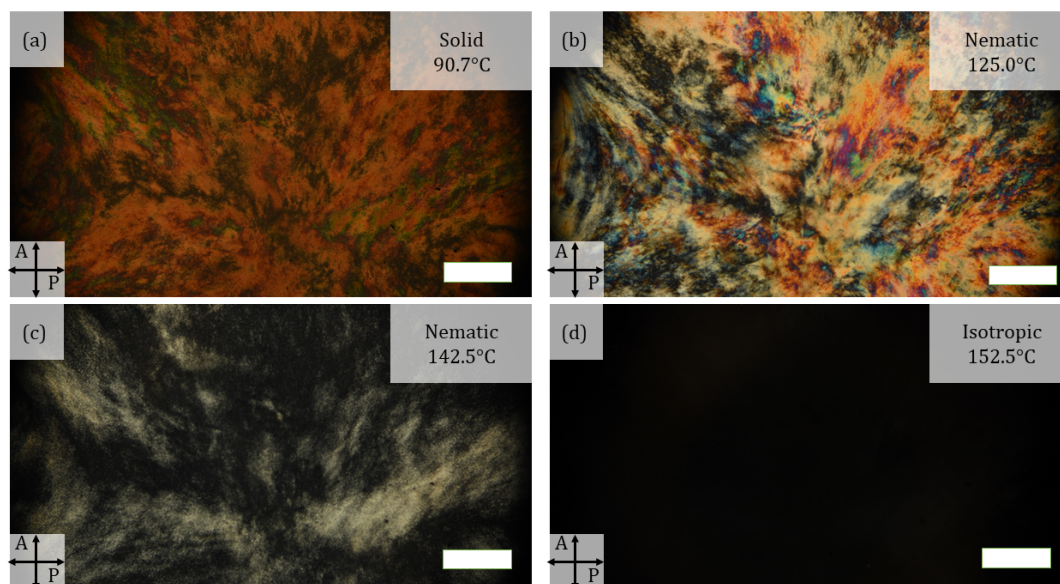


Figure 5.14: POM images of $PChol_{50} - b - PCB_{100}$ taken in a $33.9\mu\text{m}$ cell with planar alignment (a) 90.7°C , (b) 125.0°C (c) 142.5°C and (d) 152.5°C after cooling from isotropic at rate of $2.5\text{km}\text{in}^{-1}$. Transmission mode, 20x magnification. Scale bar = $500\mu\text{m}$.

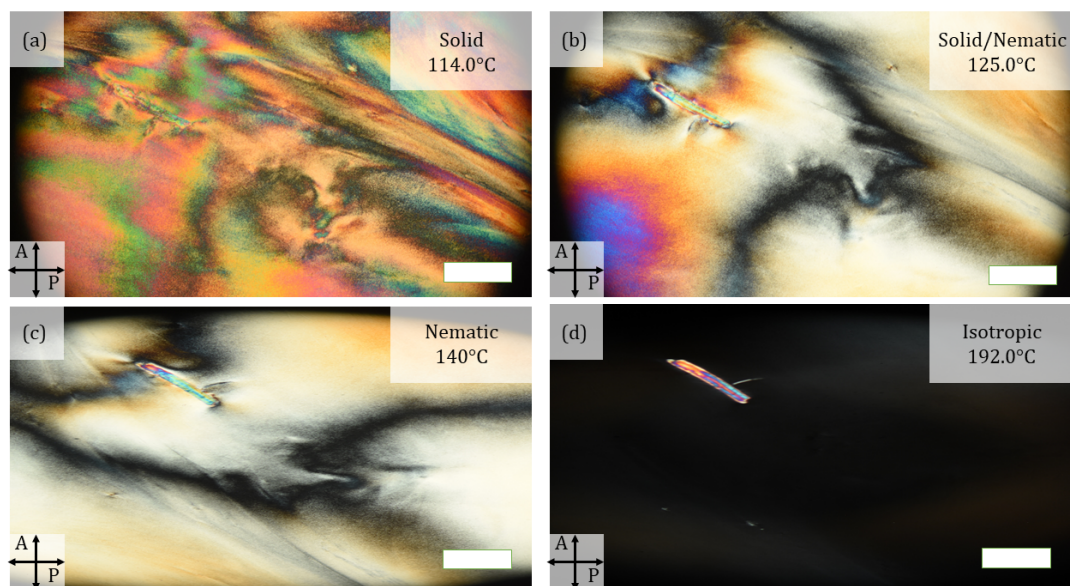


Figure 5.15: POM images of $PChol_{50} - b - PCB_{150}$ taken in a 30.4 μm cell with planar alignment (a) 114.0°C, (b) 125.0°C (c) 140.0°C and (d) 192.0°C after cooling from isotropic at rate of 2.5 Kmin^{-1} . Transmission mode, 20x magnification. Scale bar = 500 μm .

5.5 PISA nanostructures

During the synthesis of diblock copolymers, the solution started turning opaque, a good indicator of successful PISA. In order to confirm the morphology of the resulting particles, AFM studies were undertaken to characterise the resulting nanoobjects. TEM studies could not be undertaken at the time due to limited availability of suitable electron microscopes. Nonetheless, AFM micrographs confirm successful self-assembly of the copolymers (Figure 5.16).

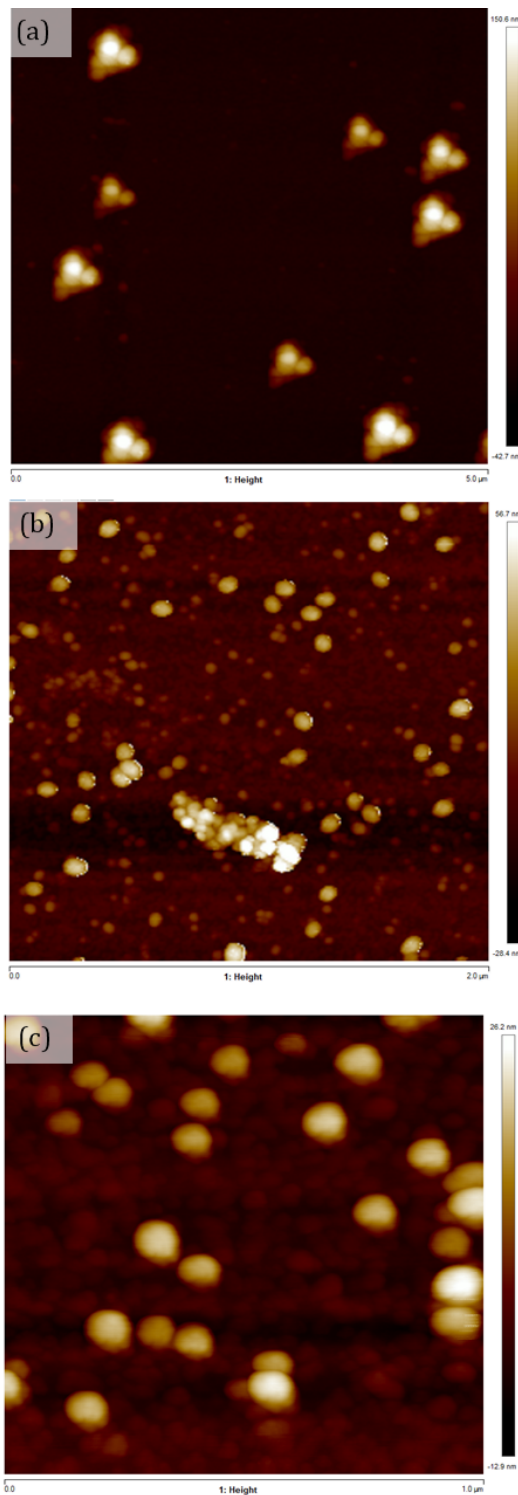


Figure 5.16: AFM micrographs for height profiles for (a) $PChol_{50} - b - PCB_{50}$, (b) $PChol_{50} - b - PCB_{100}$ and (c) $PChol_{50} - b - PCB_{150}$. Samples were prepared by spin casting 1% solution of the stock solution onto cleaned silicon wafers at 3000RPM for 20 seconds.

All three of the polymers self-assembled into spherical nanoparticles. Spheres of $PChol_{50} - b - PCB_{50}$ appear to cluster together, forming larger aggregates. $PChol_{50} - b - PCB_{100}$ and $PChol_{50} - b - PCB_{150}$ do not cluster together, instead forming singular particles. The spheres of $PChol_{50} - b - PCB_{100}$ have an average diameter of 80 ± 20 nm as calculated by AFM. The average radius increases in $PChol_{50} - b - PCB_{150}$ up to 100 ± 10 nm. The size dispersity appears to increase as a function of DP however, without appropriate control for the dispersity of the polymer molecules its not possible to specifically say if the change is due to increase in size or the dispersity of polymer.

5.6 Conclusions

Successful synthetic preparations of liquid crystalline block copolymers was achieved. The liquid crystalline properties of these polymers were than characterised. All of the block copolymers prepared show strong liquid crystalline properties however obstacles such as alignment remain. AFM studies were able to confirm successful preparation nanoobjects via PISA. The impact of the chain length in the context of LC properties was shown where increase in the DP of the cyanobiphenyl block leads to widening of the T_{N-I} gap. The impact of the chain extension was also studied in the context of PISA nanoobjects prepared where the size of the spheres was increasing as a function of the DP of the cyanobiphenyl block.

Chapter 6

Self-assembly and applications of block copolymers in thin films

6.1 Overview

Self-assembly of supramolecular nanostructures from amphiphilic particles is ubiquitous in the organic as well as in the synthetic world. The constant shrinkage of semi-conductor for smaller and smaller electronics has slowly been approaching the theoretical limits available with the well established methods and materials. Fears that 'Moore's Law' has come to a premature slowdown have been present within industry for a while. New materials and templates are needed in order to fulfill the needs of next generation electronic devices and chips. The popular target feature size for chip manufacturers are sub-10 nm size periodic structures.^[116,117] Block copolymers are well known to self-assemble into periodic structures which can be used as templates for lithographic processes however even with those obtaining a sub-10nm features has been proven to be difficult. New methods and processes created in the last decade have enabled preparation of more defined and more diverse copolymers which can reliably achieve the desired nanoscales. One of the methods that enabled the achievement of such tiny scales is incorporation of liquid-crystalline components. Liquid crystals are well known to self-assemble and when incorporated into BCPs, they create another way of controlling and fine tuning the self-assembly process. In recent years, sizes as small as 5nm were effectively prepared using LCBCPs.^[118]

6.2 Materials and sample preparation

Within this chapter are the results of preparing self-assembled films from commercially available BCPs as well as film prepared from the materials prepared in Chapters 4 and 5. Styrene-ethylene-butylene-styrene (SEBS) and Styrene-isoprene-styrene (SIS) block copolymers were selected as suitable candidates for self-assembly studies based on their well defined amphiphilicity.

6.2 Materials and sample preparation

Styrene-ethylene-butylene-styrene (SEBS) block copolymer was purchased from Sigma Aldrich and used without any further purification. Styrene-isoprene-styrene (SIS) block copolymer was purchased from Sigma Aldrich and used without any further purification. PStMA-b-PFOEMA block copolymers were prepared as described in Chapter 4. PChol-b-PCB block copolymers were prepared as described in Chapter 5. Both of these were used as is.

General sample preparation for the films went as follows: The dry BCP was weighed out into a clean vial. Set volume of solvent was added to the vial. The sample was vortex mixed if the material was struggling to dissolve. Silicon wafers were cut into approx. 1x1cm sized squares and stuck onto a magnetic AFM stub with epoxy. They were then prepared for spin casting by cleaning in solvents (solution of Decon 90, Methanol, Acetone, IPA and water) for 30 minutes in each solvent in a sonicator. Once the substrates were clean, they were placed onto the spin coater where a set volume of the dissolved BCP was added and spun at set speed. Once the substrates were coated with the BCP, the polymers were annealed via thermal annealing or solvent annealing. Once annealed, samples were studied using the AFM and Ellipsometry.

6.3 Self-assembly in thin films

The comprehensive theory of the self-assembly process is described in Chapter 1.

Table 6.1: Thickness of the SEBS layer prepared from the 0.4% and 0.8% solutions of SEBS in toluene as measured by Ellipsometry after spincoating for 20seconds at given RPM.

	2000RPM	3000RPM
0.4%	13.5 nm	12.2 nm
0.8%	32.5 nm	26.3 nm

6.3.1 Self-assembly of SEBS

In order to identify correct annealing temperatures for thermal annealing, a sample of SEBS was studied using DSC (Fig. A). 0.4% and 0.8% solutions of SEBS block copolymer in toluene were prepared. Thin films were prepared by spin casting the solutions on to the cleaned wafers. Wafers were accelerated to 2000/3000RPM and three drops of the solutions were dropped onto the wafers. Samples were spun for 20 seconds. Thermal annealing was performed at 150°C under vacuum for a set amount of time. The samples were placed in closed glass Petri dishes to minimise exposure to dust and other debris during venting of the oven. Solvent annealing, was performed at room temperature set to 22°C. A glass petri dish was lined with a filter paper and the filter paper was saturated with the solvent, cyclohexane. A sample was placed directly onto the filter paper, film facing away from the filter paper. The petri dish was closed and a dead weight was placed on top to tighten the seal to avoid lose of vapours. The first set of samples was studied to investigate the optimal conditions to form films from SEBS in toluene solution at 0.4% and 0.8% w/w solutions. Four samples were prepared, two different concentrations and two different speeds of spin casting were investigated. The films were than studied using ellipsometry to calculate the thickness of the layers formed. The wafers used for the samples was also investigated to find the thickness of the SiO₂ layer on top. The thickness of the SiO₂ was calculated to be 6.7nm. As seen in table 6.1, the film thickness increases as the concentration increases and decreases as a speed increased. The films were studied again after the annealing process. The control sample after 22h at ambient was found to be 27.87nm thick, the thickness not being influenced by the process. The thermally annealed sample was found to be 29.45nm thick,

6.3 Self-assembly in thin films

approx. 2nm thicker than control. The sample annealed using solvent vapour was also investigated however was unsuitable for ellipsometry measurements as the surface was not sufficiently flat for the ellipsometry. The solvent annealed sample was instead studied using Dektak stylus profiler (Figure 6.1). The scan of the surface confirmed the surface was creased making it unsuitable for ellipsometry measurements.

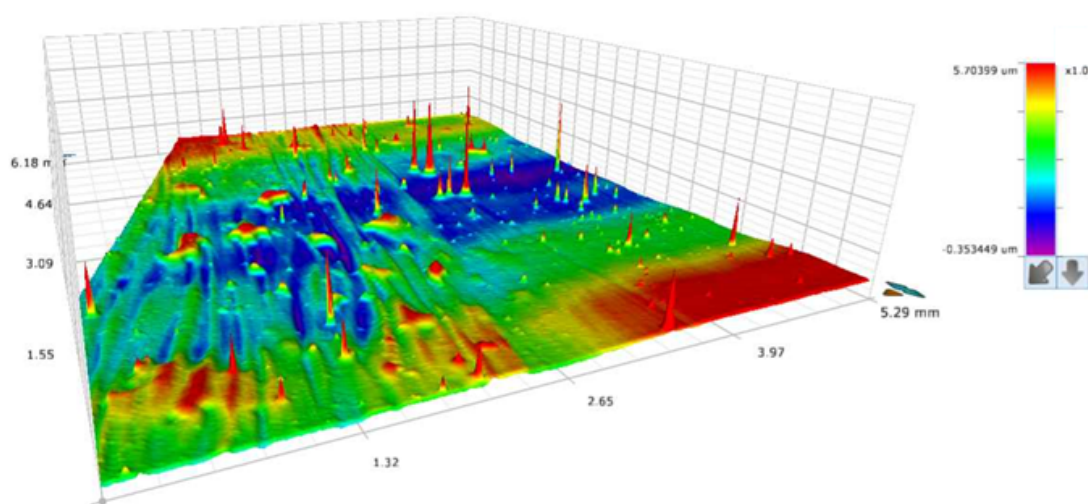


Figure 6.1: Surface profile of a silicon wafer covered with 0.8% SEBS solution and thermally annealed using cyclohexane.

Surfaces were scanned using AFM in tapping mode using RTESPA-350 probe and MultiMode 8-HR microscope. Both the height profile and the phase channel were investigated to identify the self-assembly behaviour. The control sample had a clear self-assembling behaviour observed only in the phase profile. The self-assembly was incomplete with mixed fingerprint pattern as well as spheres. The height profile also showed some major unevenness on the surface. This overall demonstrated that the self-assembly of the film was however required specific conditions.

6.3 Self-assembly in thin films

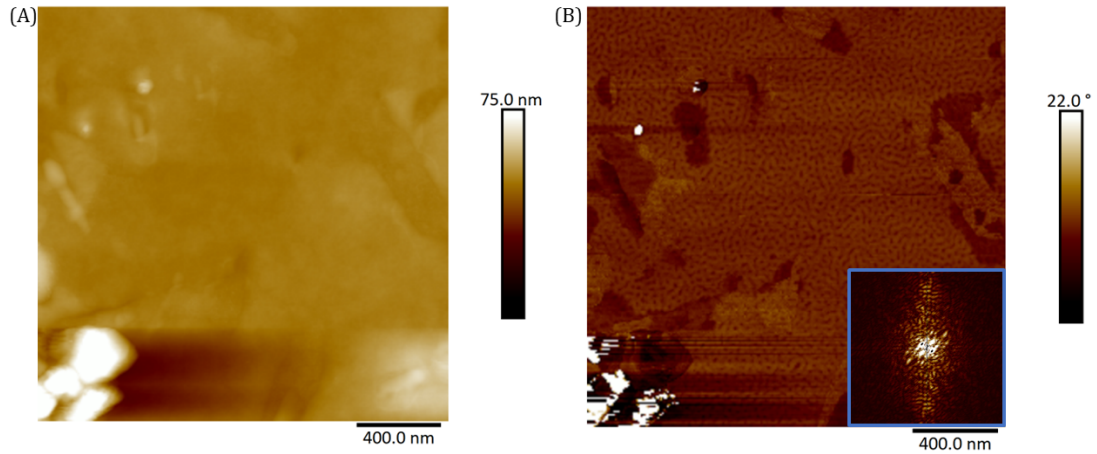


Figure 6.2: AFM images of SEBS Control sample prepared from 0.8% solution of pure SEBS in toluene, spin cast at 3000RPM for 20seconds and left at ambient temperature for 22 hours. (A) - Height profile (B) - Phase profile

The next sample investigated was the solvent annealed one. While the surface was uneven, it was still possible to find a spot on the surface sufficiently flat for the AFM to scan. However, measurements of film thickness can be performed on the AFM no appropriate AFM probe was available for the measurements. The phase and height profiles for small areas were collected. The solvent annealed surface under height profile was almost entirely flat only fluctuating by approx. 2nm.

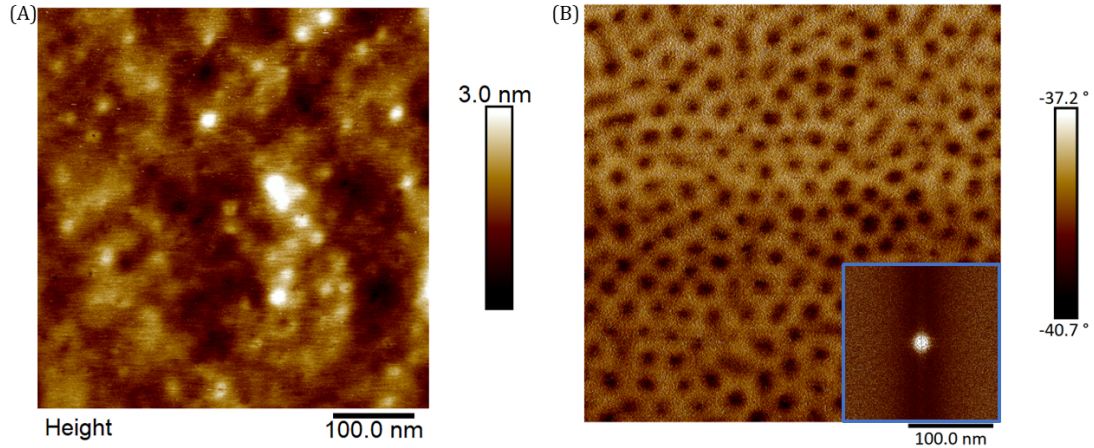


Figure 6.3: AFM images of SEBS sample prepared from 0.8% solution of pure SEBS in toluene, spin cast at 3000RPM for 20seconds and solvent annealed with toluene for 22 hours. (A) - Height profile (B) - Phase profile Inset in (B) corresponds to the FFT of the phase image.

No obvious self-assembly was observed in the height profile. The phase profile on the other hand clearly shows complete self-assembly of the BCP within thin film (Figure 6.5(b)) A diagonal cross section showing the height and phase differences in the same line were shown in Figure 6.4. The structures formed were predominantly tightly packed spheres. The size of the spheres was analysed for distribution with Nanoscope analysis software used for AFM imaging. The spheres varied in diameter at $20 \pm 3\text{nm}$.

6.3 Self-assembly in thin films

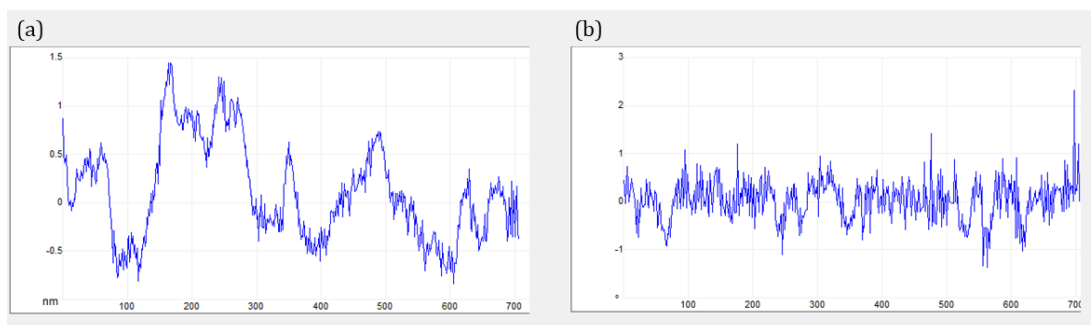


Figure 6.4: Top left to bottom right diagonal cross section of (a) height and (b) phase images of Figure 6.5 respectively.

The thermally annealed sample has formed long fingerprint-like pattern with few spheres remaining. The resulting spheres were found to be 27 ± 3 nm in diameter; larger than those observed under the solvent annealed sample.

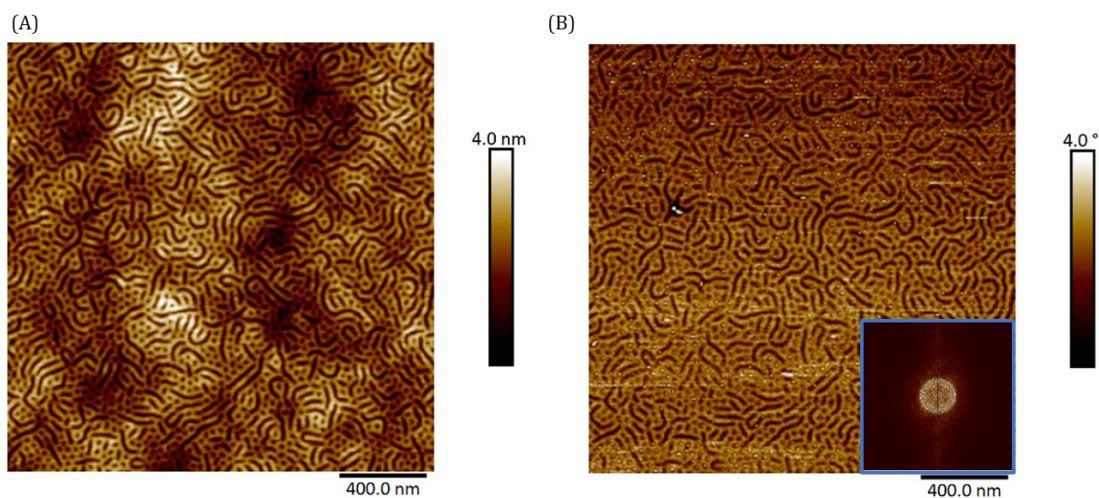


Figure 6.5: AFM images of SEBS sample prepared from 0.8% solution of pure SEBS in toluene, spin cast at 3000RPM for 20seconds and thermal annealed at 140°C for 22 hours. (A) - Height profile (B) - Phase profile. Inset in (B) corresponds to the FFT of the phase image.

6.3.2 Self-assembly of PStMA-b-PFOEMA

Within this section, the results for the thin-film self-assembly of PStMA-b-PFOEMA prepared in Chapter 4 as well as their acrylic equivalents are shown and discussed. The samples were prepared by dissolving pure $PStMA_{11} - b - PFOEMA_{50}$ in THF at 0.8% w/w and spin casting at 3000RPM for 20 seconds. The samples were then annealed through either thermal annealing at 150°C for 24 hours or by solvent vapour annealing by exposure to atmosphere saturated with cyclohexane. A control sample was also prepared and kept at ambient conditions for the same period of time as the other annealed samples.

The control sample of $PStMA_{11} - b - PFOEMA_{50}$ does not show any significant self-assembly after 24 hours at ambient. The sample appears to have formed large and polydisperse spheres between 50 and 200nm in diameter. No phase separation was seen in between or inside the resulting spheres (Figure 6.6(B)).

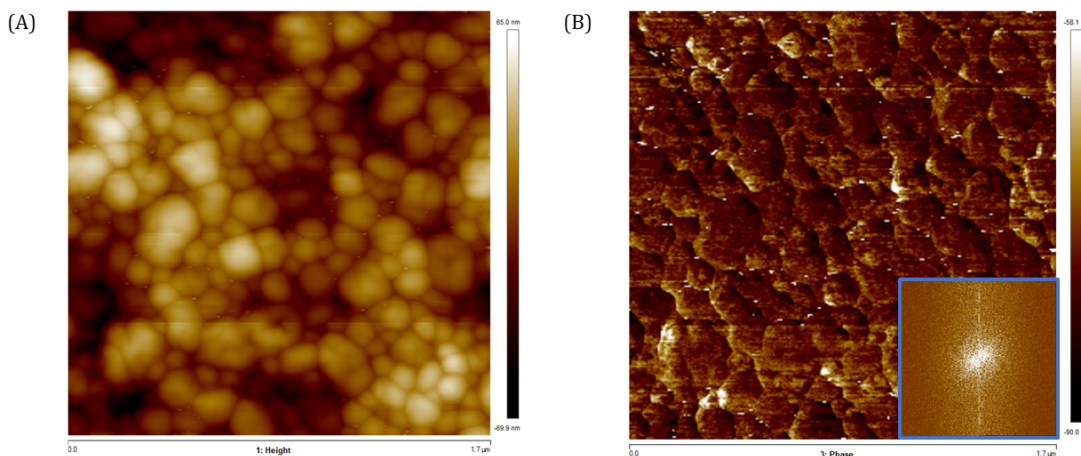


Figure 6.6: AFM images of $PStMA_{11} - b - PFOEMA_{50}$ prepared from 0.8% solution of precipitated polymer in THF, spin cast at 3000RPM for 20 seconds and left at ambient for 24 hours. (A) - Height profile (B) - Phase profile. Inset in (B) corresponds to the FFT of the phase image.

The thermally annealed sample of the methacrylic was found to have formed a uneven film after 24 hours. Within the height profile of the film (Figure 6.7(A)),

6.3 Self-assembly in thin films

no phase separation was observed. The phase profile on the other hand shows strong phase separation between the blocks. The self-assembly seems to be incomplete with it appearing to try to take form of spheres similar to those observed in SEBS sample however being trapped into more ellipsoidal shapes. These shapes formed were a result of the strong associative forces between the fluoroalkene side chains which appear to be kinetically frozen at the chosen temperature, similar to the reasons for the formation of the ellipsoidal particles in the PISA nanoobjects seen in Chapter 4.

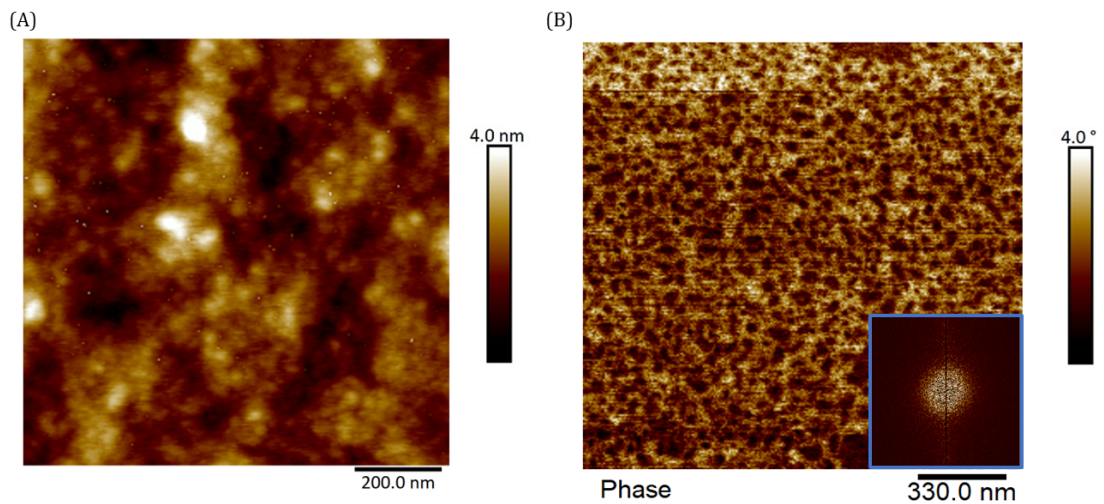


Figure 6.7: AFM images of $PStMA_{11} - b - PFOEMA_{50}$ prepared from 0.8% solution of precipitated polymer in THF, spin cast at 3000RPM for 20 seconds and thermally annealed at 150°C for 24 hours. (A) - Height profile (B) - Phase profile. Inset in (B) corresponds to the FFT of the phase image.

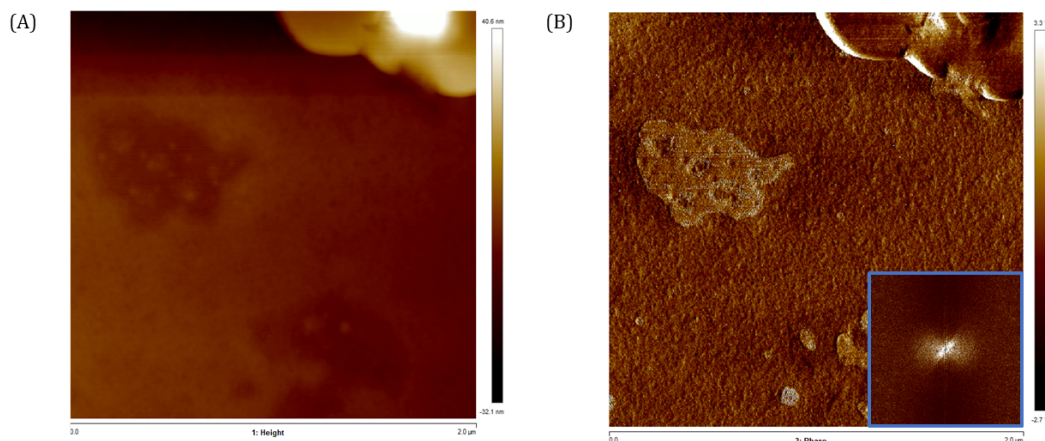


Figure 6.8: AFM images of $PStMA_{11} - b - PFOEMA_{50}$ prepared from 0.8% solution of precipitated polymer in THF, spin cast at 3000RPM for 20 seconds and solvent vapour annealed with cyclohexane at for 24 hours. (A) - Height profile (B) - Phase profile. Inset in (B) corresponds to the FFT of the phase image.

Solvent annealed sample (Figure (6.8)) was found to have formed a thin film however no self-assembly was observed in either the height or the phase profiles. Solvent vapour annealing was done over 24 hours which in within literature values for similar system is long enough to afford at least partial self-assembly provided the interaction parameters are sufficiently high or the solvent is not overly selective towards one of the blocks. Within the context of this system, a likely explanation for the observed results is the constant uptake and release of the solvent forcing adaptation of the structure to disrupting the interactions between the individual blocks as well as between the solvent and the film surface. Vapour annealing causes the film to swell (also leading to the decrease of glass transition temperature) where once the film is abruptly removed from the environment, the departure of the solvent disrupts the ordered structure it could have had before. As the associative forces for the perfluorinated parts of the molecule, it is possible for them to end up sticking together, away from the air-film interface once the solvent is no longer swelling the layer, leading to perceived absence of self-assembly under AFM.

6.3.3 Self-assembly of PChol6MA-b-PCB6MA

Thin films of PChol6MA-b-PCB6MA block copolymers prepared in Chapter 5 were prepared by spin casting stock solution of fully dissolved polymers in toluene. The samples were then annealed through thermal annealing or solvent annealing with toluene. (Figures 6.9 - 6.11) Toluene has a strong affinity for the biphenyl group.^[119]

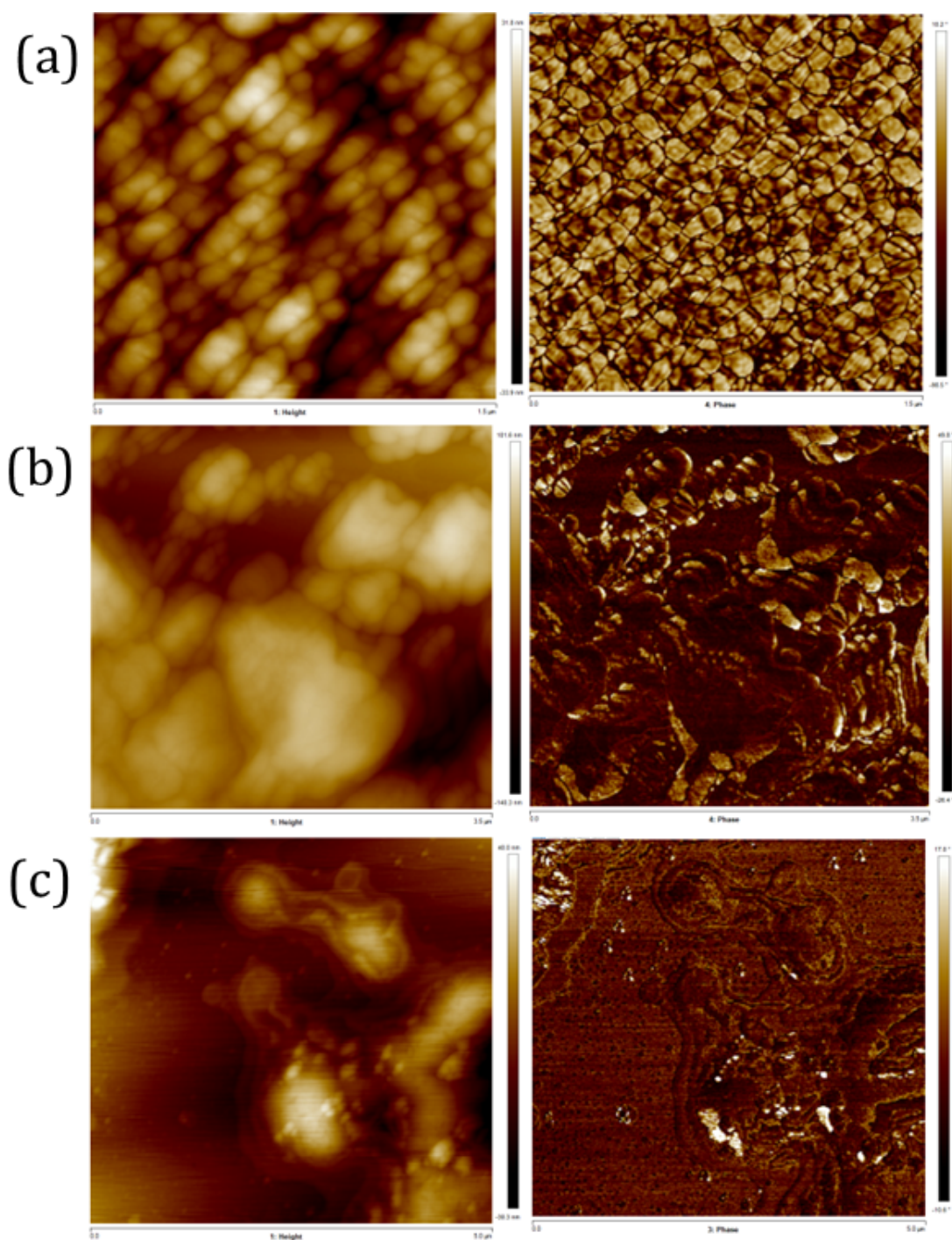


Figure 6.9: Height (left) and phase (right) AFM micrographs of PChol₅₀-b-PCB₅₀. (a) Control sample left at ambient conditions for 24 hours. (b) Solvent vapour annealed sample by exposure to toluene for 22 hours at ambient room temperature. (c) Thermally annealed sample prepared at 100°C for 24 hours.

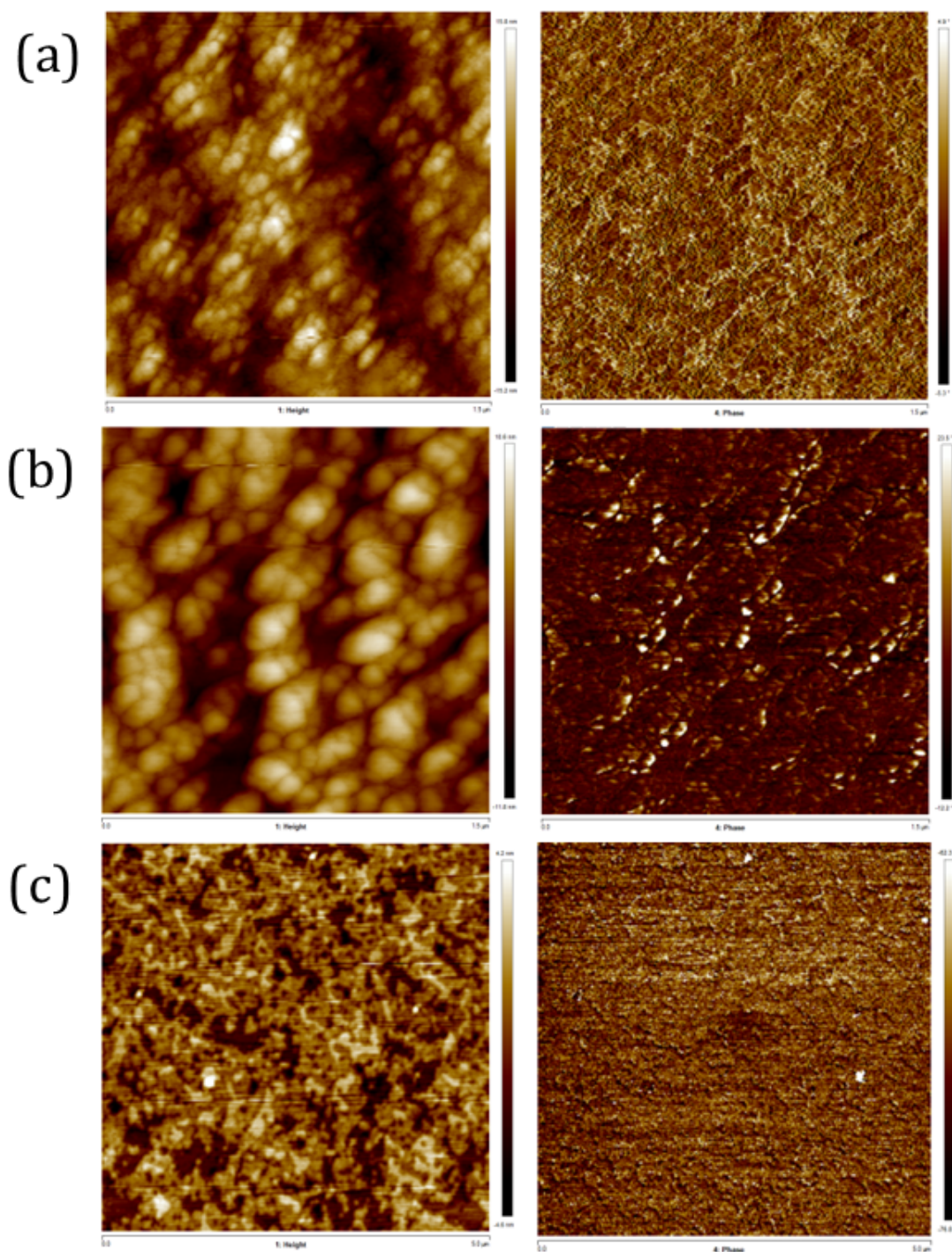


Figure 6.10: Height (left) and phase (right) AFM micrographs of PChol₅₀-b-PCB₁₀₀. (a) Control sample left at ambient conditions for 24 hours. (b) Solvent vapour annealed sample by exposure to toluene for 22 hours at ambient room temperature. (c) Thermally annealed sample prepared at 100°C for 24 hours.

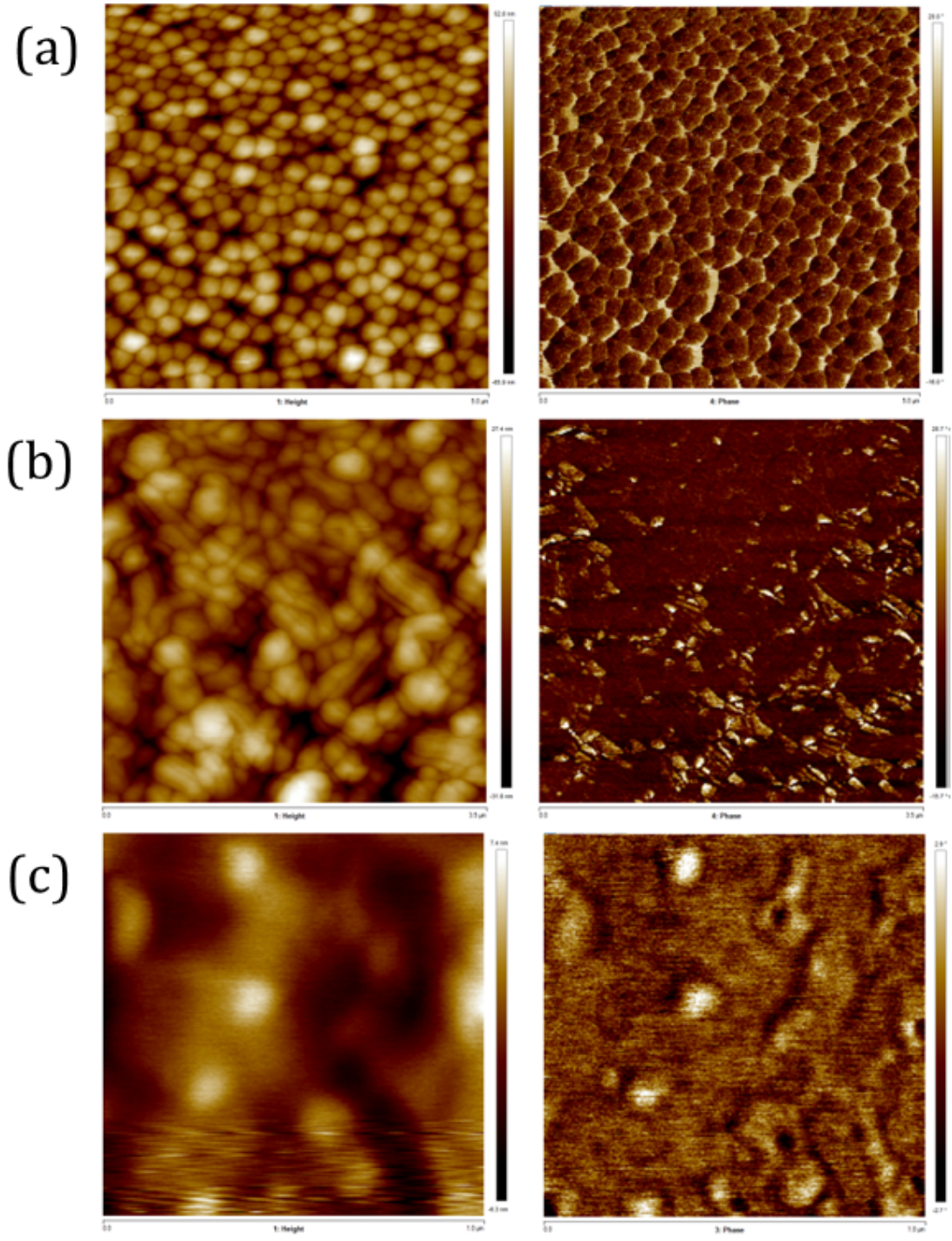


Figure 6.11: Height (left) and phase (right) AFM micrographs of PChol₅₀-b-PCB₁₅₀. (a) Control sample left at ambient conditions for 24 hours. (b) Solvent vapour annealed sample by exposure to toluene for 22 hours at ambient room temperature. (c) Thermally annealed sample prepared at 100°C for 24 hours.

The Chol-CB monomers appear to not have a sufficiently high Flory - Huggins interaction parameter to self-assemble under the solvent and thermal annealing, regardless of how significant the volume fraction of each block is. The thermodynamic driving force is not sufficiently large to ensure the blocks separate. Even though LC BCPs have been reported to self-assemble at lower χ values relative to non-LC BCPs, within this system the difference was still not sufficiently large.^[120] The enthalpy introduced into the system was abundant enough to allow the molecules to at least partially rearrange themselves, as indicated by the change of the thin films observed from the control sample which was kinetically locked into the conformation it was spin coated to and the thermally annealed samples which were kept at temperatures just below the order-order transition as indicated by the DSCs and POM images.

Selectivity of the solvent used in vapour annealing can perhaps be used to explain the lack of observed self-assembly. Due to high preference of the biphenyl block, the surface formed during the annealing process is not sufficiently neutral enough for the Cholesteryl block to interact with it and instead forming lamellar layers underneath the biphenyl phase. Such alignment of the BCP would be indistinguishable under AFM as a phase consisting of equal parts biphenyl and cholesteryl (i.e. fully mixed phase) would appear exactly the same as a pure biphenyl phase (i.e. not mixed at all). In order to differentiate such difference, more penetrating surface characterisation methods are needed such as Grazing Incidence SAXS.

6.3.4 Conclusion

Effective ways of self-assembling SEBS thin films on silicon substrates were achieved. Through the use of solvent annealing method with toluene, semi-periodic spherical structures were observed on the surface of the films. These structures were only present in the phase images of the films with the physical surface being rough and uneven however the roughness did not appear to be connected to the self-assembled structures found in the phase imaging. Thermal annealing was also used to successfully prepare fingerprint patterns. Unlike the spherical pattern

observed in the solvent annealed film, this fingerprint pattern was also a physical imprint within the thin film.

The self-assembly behaviour of PStMA-b-PFOEMA was studied in order to identify the role played by the LC order within the process. Solvent annealing with cyclohexane was found to be ineffective in formation of self-assembled films. While the film was formed uniformly with little defects relative to thermally annealed sample, no periodic structures were found. The thermally annealed on the other hand was found to have partially self-assembled into periodic spherical structures. This observation was only found within the phase diagram and was mostly absent in the physical topographical features of the film. Control sample was found to be unaffected by the conditions instead forming larger aggregates of spheres, likely coming together as a result of drying of the film.

The self-assembly of PChol6MA-b-PCB6MA LC BCP within thin films was investigated in order to establish its properties in contrast to copolymers containing non-LC groups. The polymers were found not to self-assemble into periodic structures in films based on thermal and solvent vapour annealing with toluene. The films were found to have relaxed and compared to their control samples however no actual self-assembly was observed using the AFM method.

Chapter 7

Conclusions

Block copolymers are great prospective materials for the next generation of smart nanomaterials, both as lithographic templates and as devices themselves. Synthetic methods for controlled preparation of polymers developed such as RDRP and ionic polymerisation has allowed chemists to prepare polymers with levels of precision not otherwise achievable with previous methods. Popularisation of RDRP and ionic polymerisations in the last decade has paved way for the invention of facile yet highly controlled methods for preparing variety of nanostructures from said polymers. Methods such as polymerisation-induced self-assembly or electrostatic self-assembly have already been shown to be more effective and reliable than their predecessors and have rightly taken the places for the most popular methods for controlled self-assembly in solution. Their highly tunable structures, controlled by simple variables such as solvent fractions and temperatures have made them accessible to even scientists inexperienced in the polymer synthesis techniques. Yet many classes of monomers remain underexplored despite showing promise in the limited number of studies. An example of such class remain liquid crystalline monomers. As seen in Figure 7.1, the number of articles containing the phrases 'liquid crystal' as well as 'polymerisation-induced self-assembly' lags behind the growth rate of pure PISA, despite being one of the class of molecules which originally lead to invention of PISA.

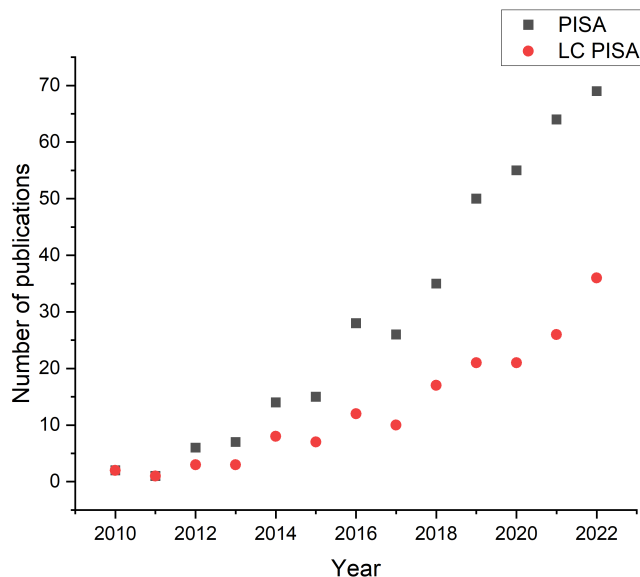


Figure 7.1: The number of publications containing the phrases 'liquid crystal' and 'polymerisation-induced self-assembly' per year as per Google Scholar. Accessed in 2022.

The work undertaken in this thesis focuses on expanding the range of available liquid crystalline monomers available for PISA as well as at demonstrating the potential applications these monomers bring to the table. While underexplored in this thesis, certain responsive elements of the particles are explored here. This PhD project was successful in bringing together the three aspects of liquid crystals field; chemistry, physics and engineering. Within the scope of the project, multiple new and never seen before polymers, liquid crystals and nanoobjects were prepared and characterised.

The synthetic pathways described in Chapter 3 were designed to be modular where the backbone, spacers and the mesogens can be interchanged easily to produce a wide variety of monomers for potential uses in PISA. In fact, an example of such molecules was demonstrated in Chapter 5 where the monomers were used for construction of liquid crystalline block copolymers not seen before. This in combination with RDRP techniques such as RAFT opened up chemical avenues for multi-block novel copolymers with tunable properties such as responsiveness

and controlled self-assembly.

Within Chapter 4, perhaps currently less popular perfluorinated mesogens were explored and brought back to the limelight. With modern polymerisation methods their previous limitations such as poor solubility and limited degree of polymerisation were overcome.

Appendix A

Appendix

FEOMA GAMESS summarised results

ATOM	CHARGE	X	Y	Z
C	6.0	5.7157289421	4.0996452584	2.6366425498
C	6.0	6.9250566656	3.9425397589	3.1293032892
C	6.0	7.8091631326	2.7879715167	2.6781395011
C	6.0	7.5551052415	4.8642760774	4.1655067949
O	8.0	7.1521432460	1.9465109696	1.7786750119
O	8.0	8.9534783049	2.5908189988	3.0463773264
C	6.0	7.9934966087	0.8819969231	1.3053366622
C	6.0	7.1761602292	0.0559452404	0.2877590735
C	6.0	6.8461618319	0.8778744920	-0.9999654782
C	6.0	5.9887918258	-0.0151272426	-2.0231716163
C	6.0	5.3708586507	0.8474101299	-3.2265276873
C	6.0	6.5077525440	1.5340539954	-4.1314427885
C	6.0	5.9674336914	1.9274825066	-5.5916085150
C	6.0	4.4908642876	3.6076214311	-6.9858566202
C	6.0	3.2807465431	4.6734057443	-6.9248086462
H	1.0	5.3149717449	3.4225393323	1.8943170468
H	1.0	5.0737475358	4.9110282847	2.9526153822
H	1.0	6.8670799691	5.6578615387	4.4406472642
H	1.0	8.4664561810	5.3080459117	3.7762866388

H	1.0	7.8102663364	4.3086116446	5.0659681552
H	1.0	8.3119353946	0.2325713863	2.1289869274
H	1.0	8.8992410306	1.2756902834	0.8314109668
H	1.0	6.2414416016	-0.2706325860	0.7382771934
H	1.0	7.7447730967	-0.8233804569	-0.0078119083
F	9.0	8.0104306905	1.2600593030	-1.6345958832
F	9.0	6.1377006828	2.0201229720	-0.7026208592
F	9.0	4.9356709492	-0.5992611560	-1.3523243215
F	9.0	6.7803316412	-1.0207288211	-2.5290594036
F	9.0	4.5606341647	1.8341797699	-2.7120104685
F	9.0	4.5960574348	0.0136658828	-4.0020464474
F	9.0	7.5705948351	0.6738676735	-4.2909691784
F	9.0	6.9581132036	2.6703949354	-3.4988372971
F	9.0	5.5050405765	0.8062290936	-6.2407146538
F	9.0	7.0261911915	2.4356803368	-6.3110004936
F	9.0	4.1494398866	2.5813579502	-7.8368901065
F	9.0	5.6099983714	4.2368382940	-7.4807305816
F	9.0	2.1465170755	4.0884495695	-6.4268701440
F	9.0	3.0180084332	5.1464774815	-8.1839958301
F	9.0	3.6223347716	5.7291514073	-6.1201844079
C	6.0	4.7914674622	3.0188612824	-5.5244015318
F	9.0	5.1456272819	4.0482863637	-4.6838084661
F	9.0	3.6508767120	2.4233465226	-5.0353264496

SAXS Gaussian fitting script (Python)

```
## Imports
import scipy.optimize as sc
import matplotlib.pyplot as plt
import numpy as np
import matplotlib.ticker as ticker
import glob, os

## Surpress warnings.
import warnings
warnings.filterwarnings("ignore")
workdir = r'' ## ENTER DIRECTORY FOR THE FILES

##Define functions
def gaus(x,a,x0,sigma):
    return a*np.exp(-(x-x0)**2/(2*sigma**2))

def linear(x,m,c):
    return m*x + c

def FWHM(sigma):
    return (sigma * 2 *(2*np.log(2))**0.5)

def qtod(q):
    twopi = 2*np.pi
    d = twopi/q
    return d

def multi_gaussian(x,*pars):
    offset = pars[-1]
    g1 = gaus(x, pars[0], pars[1], pars[2])
    g2 = gaus(x, pars[3], pars[4], pars[5])
```

```

    #g3 = gaus(x, pars[6], pars[7], pars[8])
    return g1 + g2 + offset# g3 + offset

def find_nearest(array, value):
    array = np.asarray(array)
    idx = (np.abs(array - value)).argmin()
    return idx ## return array[idx] to return nearest actual VALUE at idx (index)

class generatePlots:
    def genplot(self, s, manual = False, fits = False):
        ##Load Data
        filename = workdir
        datfile = r''.join(filename+'\\'+ s)

        data = np.genfromtxt(datfile)
        x = np.genfromtxt('E:/q.txt')
        fig, ax=plt.subplots()
        plt.title(s)
        plt.loglog((x),data,'ro', markersize=5) # Plot all data (Red)
        plt.show()

        if(manual == True):
            print('Select four points for baseline fitting')
            inputs = plt.ginput(4)
            (startDataRange1) = find_nearest(x,inputs[0][0])
            (endDataRange1) = find_nearest(x,inputs[1][0])
            (startDataRange2) = find_nearest(x,inputs[2][0])
            (endDataRange2) = find_nearest(x,inputs[3][0])
        if (manual == False):
            # # #Define variables
            startDataRange1,endDataRange1,startDataRange2, endDataRange2= 0 , 15

```

```

##Join selected data to be used for fitting.
x_for_fit = np.log(np.concatenate((x[startDataRange1:endDataRange1],x[st
y_for_fit = np.log(np.concatenate((data[startDataRange1:endDataRange1],d
x_for_fit = x_for_fit[np.logical_not(np.isnan(y_for_fit))])
y_for_fit = y_for_fit[np.logical_not(np.isnan(y_for_fit))])

##Fit using polyfit
fit = np.polyfit(x_for_fit,y_for_fit,1)
y_fit = np.polyval(fit,np.log(x))

##Subtract the baseline from the results.
y_presub = np.exp(y_fit)
y_subtracted = np.log(data)- y_fit

boundss = ((0,0,0,0,0,0),(np.inf,np.inf,np.inf,np.inf,np.inf,np.inf))

if (fits == True):
    print('Select range for gaussian fit')
    gausInputs=plt.ginput(2)
    gausStart = find_nearest(x,gausInputs[0][0])
    gausEnd = find_nearest(x,gausInputs[1][0])

    gaus_fits = sc.curve_fit(multi_gaussian,x[gausStart:gausEnd],y_subtr
    gaus_y_fit = multi_gaussian((x[gausStart:gausEnd]),gaus_fits[0][0],g

    print(gaus_fits)
    gaus_1_y_fit = gaus(x[gausStart:gausEnd],gaus_fits[0][0],gaus_fits[0
    gaus_2_y_fit = gaus(x[gausStart:gausEnd],gaus_fits[0][3],gaus_fits[0
    # gaus_3_y_fit = gaus(x[gausStart:gausEnd],gaus_fits[0][6],gaus_fits[

```

```

plt.loglog((x[gausStart:gausEnd]),np.exp((gaus_1_y_fit)))
plt.loglog((x[gausStart:gausEnd]),np.exp((gaus_2_y_fit)))
# plt.loglog((x[gausStart:gausEnd]),np.exp((gaus_3_y_fit)))

if (fits == False):
    ##Gaussian Fit
    gaus_fits = sc.curve_fit(multi_gaussian,x[endDataRange1:startDataRan
    gaus_y_fit = multi_gaussian((x[endDataRange1:startDataRange2]),gaus_

    gaus_1_y_fit = gaus(x[endDataRange1:startDataRange2],gaus_fits[0][0])
    gaus_2_y_fit = gaus(x[endDataRange1:startDataRange2],gaus_fits[0][3])
    gaus_3_y_fit = gaus(x[endDataRange1:startDataRange2],gaus_fits[0][6])

    plt.loglog((x[endDataRange1:startDataRange2]),np.exp((gaus_1_y_fit)))
    plt.loglog((x[endDataRange1:startDataRange2]),np.exp((gaus_2_y_fit)))
    plt.loglog((x[endDataRange1:startDataRange2]),np.exp((gaus_3_y_fit)))

## Print values used and calculated.
print('')
print('Sample: ',s)
print('a:', gaus_fits[0][0])
print('mean q: ',gaus_fits[0][1])
print('d: ', qtod(gaus_fits[0][1]))
print('sigma: ', gaus_fits[0][2])
print('FWHM: ',FWHM(gaus_fits[0][2]))
print((startDataRange1),',',',', (endDataRange1),',',',', (startDataRange2),',',',

##PLOT
fig, ax=plt.subplots()
plt.title(s)
plt.loglog((x),data,'ro', markersize=5)

```

```

plt.show()

##PLOTS LINEAR
plt.plot(np.log(x),np.log(data),'ro',markersize=5)
plt.plot(x_for_fit,y_for_fit,'bo',markersize = 5) # Plot data used for f
plt.plot(np.log(x),y_fit,'k') # Plot fitted data (Black line)
plt.plot(np.log(x[0:]),y_subtracted[0:], 'g',markersize = 1) # Plot DATA

##PLOTS LOGLOG
plt.loglog(np.exp(x_for_fit),np.exp(y_for_fit),'bo') ## Plot all data
plt.loglog(x,np.exp(y_fit),'k') ## Plot fit
plt.loglog(x,np.exp(y_subtracted),'g') ## Plot baseline subtracted value
if(fits == True):
    plt.loglog((x[gausStart:gausEnd])),np.exp((gaus_y_fit)),'b') ## Pl
if (fits == False):
    plt.loglog((x[endDataRange1:startDataRange2])),np.exp((gaus_y_fit))

## Plot residuals.
y_res = y_subtracted[gausStart:gausEnd]-gaus_y_fit

x_for_res = x[gausStart:gausEnd][np.logical_not(np.isnan(y_res))]
y_for_res = y_res[np.logical_not(np.isnan(y_res))]

frame2 = fig.add_axes()
plt.loglog(x_for_res,np.exp(y_for_res))

plt.errorbar(0,gaus_fits[0][2])

## Scale manipulations.
plt.xlim(0.1,0.5)

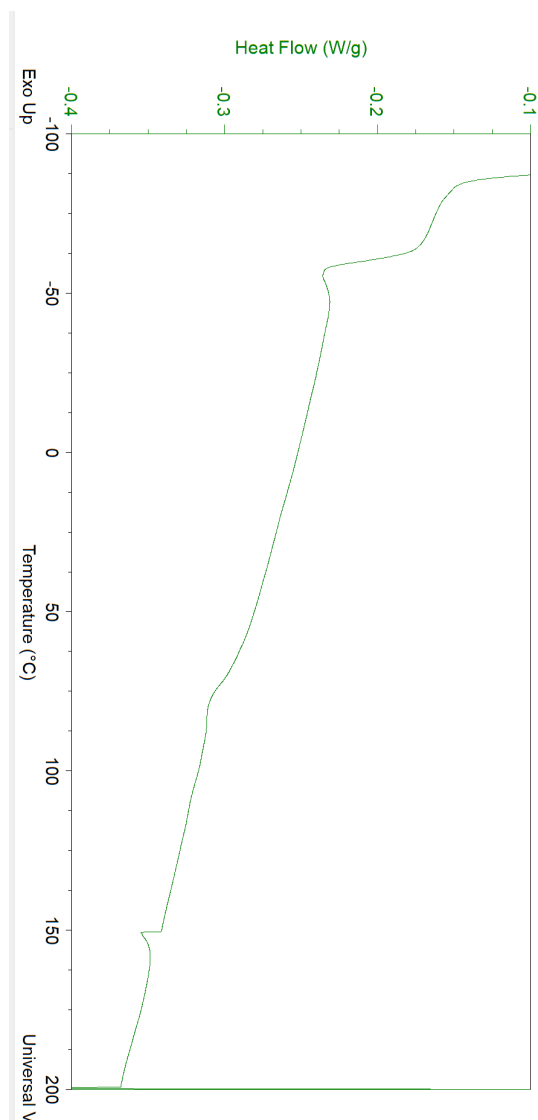
```

```
plt.ylim(0.1,10000000)
ax.set_yscale('symlog')
ax.set_xscale('symlog')
ax.xaxis.set_major_formatter(ticker.FormatStrFormatter('%.2f'))
ax.xaxis.set_minor_formatter(ticker.FormatStrFormatter('%.2f'))
ax.yaxis.set_major_formatter(ticker.FormatStrFormatter('%.2f'))
ax.yaxis.set_minor_formatter(ticker.FormatStrFormatter('%.1f'))

if __name__ == "__main__":
    os.chdir(workdir)
    files = glob.glob("*.dat")
    plot = generatePlots()
    plot.genplot(files[-1],True,True)
    tempdict = plot.__dict__

    for file in glob.glob("*.dat"):
        generatePlots(file)
```

DSC profile of SEBS polymer used in Chapter 5.



References

- [1] Wang, Y.C.; Xie, Y.B.; Zhang, T.J.; , a.; Sik Yoo, W.; Kang, K.; Murai, G.; Matsen, M.W. *Journal of Physics: Condensed Matter TOPICAL REVIEW* To cite this article: M W Matsen. Technical report, 2002. **5**, 34
- [2] Derry, M.J.; Fielding, L.A.; Armes, S.P. Polymerization-induced self-assembly of block copolymer nanoparticles via RAFT non-aqueous dispersion polymerization, 2016. <https://doi.org/10.1016/j.progpolymsci.2015.10.002>. **5**, 37
- [3] Bullard, B.; Stumpf, C.H.; Zhao, W.; Kuzenko, S.; Niehaus, G.D. Crystal Diagnostics Xpress S Kit for the rapid detection of Salmonella spp. in selected food matrixes. *Journal of AOAC International* **2017**, *100*, 1038–1050. <https://doi.org/10.5740/jaoacint.17-0035>. **14**
- [4] Schadt, M.; Helfrich, W. Voltage-dependent optical activity of a twisted nematic liquid crystal. *Applied Physics Letters* **1971**, *18*, 127–128. <https://doi.org/10.1063/1.1653593>. **14**
- [5] Chang, C.; Bang, K.; Wetzstein, G.; Lee, B.; Gao, L. Toward the next-generation VR/AR optics: a review of holographic near-eye displays from a human-centric perspective. *Optica* **2020**, *7*, 1563. <https://doi.org/10.1364/optica.406004>. **14**
- [6] Milton, H.E.; Morgan, P.B.; Clamp, J.H.; Gleeson, H.F. Electronic liquid crystal contact lenses for the correction of presbyopia. *Optics Express* **2014**, *22*, 8035. <https://doi.org/10.1364/oe.22.008035>. **14**

REFERENCES

- [7] Heilmeier, G.H.; Zanoni, L.A.; Barton, L.A. Dynamic scattering in nematic liquid crystals. *Applied Physics Letters* **1968**, *13*, 46–47. <https://doi.org/10.1063/1.1652453>. 14
- [8] *Handbook of Optoelectronics, Second Edition*; CRC Press, 2017. <https://doi.org/10.1201/9781315156996>. 18
- [9] Gleeson, H.F.; Coles, H.J. Optical Properties of Chiral Nematic Liquid Crystals. *Molecular Crystals and Liquid Crystals Incorporating Nonlinear Optics* **1989**, *170*, 9–34. <https://doi.org/10.1080/00268948908047744>. 19
- [10] Albuquerque, H.M.; Santos, C.M.; Silva, A.M. Cholesterol-based compounds: Recent advances in synthesis and applications. *Molecules* **2019**, *24*, 116. <https://doi.org/10.3390/molecules24010116>. 22
- [11] Hwang, J.J.; Iyer, S.N.; Li, L.S.; Claussen, R.; Harrington, D.A.; Stupp, S.I. Self-assembling biomaterials: Liquid crystal phases of cholesteryl oligo(L-lactic acid) and their interactions with cells. *Proceedings of the National Academy of Sciences of the United States of America* **2002**, *99*, 9662–9667. 22
- [12] Prévôt, M.E.; Andro, H.; Alexander, S.L.; Ustunel, S.; Zhu, C.; Nikolov, Z.; Rafferty, S.T.; Brannum, M.T.; Kinsel, B.; Korley, L.T.; et al. Liquid crystal elastomer foams with elastic properties specifically engineered as biodegradable brain tissue scaffolds. *Soft Matter* **2018**, *14*, 354–360. <https://doi.org/10.1039/c7sm01949a>. 22
- [13] Xie, W.; Ouyang, R.; Wang, H.; Li, N.; Zhou, C. Synthesis and cytotoxicity of novel elastomers based on cholesteric liquid crystals. *Liquid Crystals* **2020**, *47*, 449–464. <https://doi.org/10.1080/02678292.2019.1657594>. 22
- [14] Sharma, A.; Neshat, A.; Mahnen, C.J.; Nielsen, A.D.; Snyder, J.; Stankovich, T.L.; Daum, B.G.; Laspina, E.M.; Beltrano, G.; Gao, Y.; et al. Biocompatible, biodegradable and porous liquid crystal elastomer scaffolds

REFERENCES

- for spatial cell cultures. *Macromolecular Bioscience* **2015**, *15*, 200–214. <https://doi.org/10.1002/mabi.201400325>. 22
- [15] Liu, Y.; Wang, Y.; Zhuang, D.; Yang, J.; Yang, J. Bionanoparticles of amphiphilic copolymers polyacrylate bearing cholesterol and ascorbate for drug delivery. *Journal of Colloid and Interface Science* **2012**, *377*, 197–206. <https://doi.org/10.1016/j.jcis.2012.04.004>. 22
- [16] Platé, N.A.; Shibaev, V.P. Thermotropic liquid crystalline polymers—problems and trends. *Die Makromolekulare Chemie* **1984**, *6*, 3–27. <https://doi.org/https://doi.org/10.1002/macp.1984.020061984101>. 22, 27
- [17] Shibaev, V.P.; Plate, N.A.; Freidzon, Y.S. Thermotropic Liquid Crystalline Polymers. I. Cholesterol-Containing Polymers and Copolymers. *Journal of Polymer Science: Polymer Chemistry Edition* **1979**, *17*, 1655–670. 22, 28
- [18] Hamley, I.W.; Castelletto, V.; Parras, P.; Lu, Z.B.; Imrie, C.T.; Itoh, T. Ordering on multiple lengthscales in a series of side group liquid crystal block copolymers containing a cholesteryl-based mesogen. *Soft Matter* **2005**, *1*, 355–363. <https://doi.org/10.1039/b510512a>. 22
- [19] Zhou, Y.; Briand, V.A.; Sharma, N.; Ahn, S.k.; Kasi, R.M. Polymers comprising cholesterol: Synthesis, self-assembly, and applications, 2009. <https://doi.org/10.3390/ma2020636>. 22
- [20] Yusa, S.I. Self-assembly of cholesterol-containing water-soluble polymers, 2012. <https://doi.org/10.1155/2012/609767>. 22
- [21] Li, X.S.; Wu, Y.; Zhao, Y.; Yu, Z.Q. Employing Cholesterol Copolymerization Strategy for a Thermally Processable Organic Room-Temperature Phosphorescence Material. *Advanced Optical Materials* **2021**, *9*. <https://doi.org/10.1002/adom.202001893>. 22
- [22] Yang, S.Y.; Kang, J.H.; Jeong, S.Y.; Choi, K.H.; Lee, S.; Shin, G.J. Influence of chemical structure on the optical properties of new side-chain polymers containing cholesterol. *Liquid Crystals* **2014**, *41*, 1286–1292. <https://doi.org/10.1080/02678292.2014.919668>. 22

REFERENCES

- [23] Wang, Y.; Zhang, B.y.; He, X.z.; Wang, J.w. Side-chain cholesteric liquid crystalline polymers containing menthol and cholesterol - Synthesis and characterization. *Colloid and Polymer Science* **2007**, *285*, 1077–1084. <https://doi.org/10.1007/s00396-007-1654-4>. 22
- [24] Liu, X.; Guo, Z.; Xie, Y.; Chen, Z.; Hu, J.; Yang, L. Synthesis and liquid crystal behavior of new side chain aliphatic polycarbonates based on cholesterol. *Journal of Molecular Liquids* **2018**, *259*, 350–358. <https://doi.org/10.1016/j.molliq.2018.03.060>. 22
- [25] Li, L.; Zhou, F.; Li, Y.; Chen, X.; Zhang, Z.; Zhou, N.; Zhu, X. Cooperation of Amphiphilicity and Smectic Order in Regulating the Self-Assembly of Cholesterol-Functionalized Brush-Like Block Copolymers. *Langmuir* **2018**, *34*, 11034–11041. <https://doi.org/10.1021/acs.langmuir.8b01946>. 22, 78
- [26] Lee, A.L.; Venkataraman, S.; Sirat, S.B.; Gao, S.; Hedrick, J.L.; Yang, Y.Y. The use of cholesterol-containing biodegradable block copolymers to exploit hydrophobic interactions for the delivery of anticancer drugs. *Biomaterials* **2012**, *33*, 1921–1928. <https://doi.org/10.1016/j.biomaterials.2011.11.032>. 22
- [27] Venkataraman, S.; Lee, A.L.; Maune, H.T.; Hedrick, J.L.; Prabhu, V.M.; Yang, Y.Y. Formation of disk- and stacked-disk-like self-assembled morphologies from cholesterol-functionalized amphiphilic polycarbonate diblock copolymers. *Macromolecules* **2013**, *46*, 4839–4846. <https://doi.org/10.1021/ma400423b>. 22
- [28] Tran, T.H.; Nguyen, C.T.; Gonzalez-Fajardo, L.; Hargrove, D.; Song, D.; Deshmukh, P.; Mahajan, L.; Ndaya, D.; Lai, L.; Kasi, R.M.; et al. Long circulating self-assembled nanoparticles from cholesterol-containing brush-like block copolymers for improved drug delivery to tumors. *Biomacromolecules* **2014**, *15*, 4363–4375. <https://doi.org/10.1021/bm5013822>. 22
- [29] Zhang, C.Y.; Xiong, D.; Sun, Y.; Zhao, B.; Lin, W.J.; Zhang, L.J. Self-assembled micelles based on pH-sensitive PAE-g-MPEG-cholesterol

REFERENCES

- block copolymer for anticancer drug delivery. *International Journal of Nanomedicine* **2014**, *9*, 4923–4933. <https://doi.org/10.2147/IJN.S69493>. 22
- [30] Doganci, E.; Cakirlar, C.; Bayir, S.; Yilmaz, F.; Yasin, M. Methacrylate based side chain liquid crystalline polymers with pendant cholesterol group: Preparation and investigation of electrical conductivity mechanism. *Journal of Applied Polymer Science* **2017**, *134*. <https://doi.org/10.1002/app.45207>. 22
- [31] Bates, C.M.; Bates, F.S. 50th anniversary perspective: Block polymers—pure potential, 2017. <https://doi.org/10.1021/acs.macromol.6b02355>. 24
- [32] Ohkawa, S.; Ohta, R.; Kawabata, K.; Goto, H. Polymerization in liquid crystal medium: Preparation of polythiophene derivatives bearing a bulky pyrimidine substituent. *Polymers* **2010**, *2*, 393–406. <https://doi.org/10.3390/polym2040393>. 25
- [33] Park, J.H.; Singu, B.S.; Choi, O.B.; Lee, H.M.; Lee, J.Y.; Kim, S.J.; Cha, E.H.; Park, S.N.; Kwak, M.H.; So, B.K.; et al. Liquid crystal dimers having vary oxyethylene flexible spacers. *Molecular Crystals and Liquid Crystals* **2017**, *650*, 1–6. <https://doi.org/10.1080/15421406.2016.1263102>. 26
- [34] Fairclough, J.P.A.; Ryan, A.J.; Hamley, I.W.; Li, H.; Yu, G.E.; Booth, C. Diblock copoly(oxyethylene/oxybutylene) E41B8 in water: liquid-crystal mesophases studied by small-angle x-ray scattering. *Macromolecules* **1999**, *32*, 2058–2060. <https://doi.org/10.1021/ma981775j>. 26
- [35] Zha, R.H.; De Waal, B.F.; Lutz, M.; Teunissen, A.J.; Meijer, E.W. End groups of functionalized siloxane oligomers direct block-copolymeric or liquid-crystalline self-assembly behavior. *Journal of the American Chemical Society* **2016**, *138*, 5693–5698. <https://doi.org/10.1021/jacs.6b02172>. 26

- [36] Zhang, L.; Yao, W.; Gao, Y.; Zhang, C.; Yang, H. Polysiloxane-based side chain liquid crystal polymers: From synthesis to structure-phase transition behavior relationships. *Polymers* **2018**, *10*. <https://doi.org/10.3390/polym10070794>. 26
- [37] Al-Hussein, M.; Séréro, Y.; Konovalov, O.; Mourran, A.; Möller, M.; De Jeu, W.H. Nanoordering of fluorinated side-chain liquid crystalline/amorphous diblock copolymers. *Macromolecules* **2005**, *38*, 9610–9616. <https://doi.org/10.1021/ma050972x>. 26, 77
- [38] Shen, L.; Guo, H.; Zheng, J.; Wang, X.; Yang, Y.; An, Z. RAFT Polymerization-Induced Self-Assembly as a Strategy for Versatile Synthesis of Semifluorinated Liquid-Crystalline Block Copolymer Nanoobjects. *ACS Macro Letters* **2018**, *7*, 287–292. <https://doi.org/10.1021/acsmacrolett.8b00070>. 26, 27, 36, 77, 78, 79
- [39] Wang, J.; Mao, G.; Ober, C.K.; Kramer, E.J. Liquid Crystalline, Semifluorinated Side Group Block Copolymers with Stable Low Energy Surfaces: Synthesis, Liquid Crystalline Structure, and Critical Surface Tension **1997**. 26, 77
- [40] De Crevoisier, G.; Fabre, P.; Leibler, L.; Tencé-Girault, S.; Corpart, J.M. Structure of fluorinated side-chain smectic copolymers: Role of the copolymerization statistics. *Macromolecules* **2002**, *35*, 3880–3888. <https://doi.org/10.1021/ma010459t>. 26, 77
- [41] Huo, M.; Wan, Z.; Zeng, M.; Wei, Y.; Yuan, J. Polymerization-induced self-assembly of liquid crystalline ABC triblock copolymers with long solvophilic chains. *Polymer Chemistry* **2018**, *9*, 3944–3951. <https://doi.org/10.1039/c8py00643a>. 27, 77
- [42] Li, Y.; Lu, Q.; Chen, Q.; Wu, X.; Shen, J.; Shen, L. Directional effect on the fusion of ellipsoidal morphologies into nanorods and nanotubes. *RSC Advances* **2021**, *11*, 1729–1735. <https://doi.org/10.1039/d0ra09548f>. 27, 36, 77, 79

REFERENCES

- [43] Huo, M.; Li, D.; Song, G.; Zhang, J.; Wu, D.; Wei, Y.; Yuan, J. Semi-Fluorinated Methacrylates: A Class of Versatile Monomers for Polymerization-Induced Self-Assembly. *Macromolecular Rapid Communications* **2018**, *39*, 1700840–1700846. <https://doi.org/10.1002/marc.201700840>. 27, 36, 78
- [44] Xie, Y.; Hu, J.; Dou, Q.; Xiao, L.; Yang, L. Synthesis and mesomorphism of new aliphatic polycarbonates containing side cholesteryl groups. *Liquid Crystals* **2016**, *43*, 1486–1494. <https://doi.org/10.1080/02678292.2016.1185171>. 27
- [45] Doganci, E.; Davarci, D. Synthesized and mesomorphic properties of cholesterol end-capped poly(ϵ -caprolactone) polymers. *Journal of Polymer Research* **2019**, *26*. <https://doi.org/10.1007/s10965-019-1826-1>. 27
- [46] Finkelmann, H.; Ringsdorf, H.; Sol, W.; Wendoff, J.H. Synthesis of Cholesteric Liquid Crystalline Polymers Polyreactions in Ordered Systems, 15'). *Makromol. Chem* **1978**, *179*, 829–832. 27, 63
- [47] Hessel, F.; Herr, R.P.; Finkelmann, H. Synthesis and characterization of biaxial nematic side chain polymers with laterally attached mesogenic groups. *Makromol. Chem* **1987**, *188*, 1597–1611. 27
- [48] Xu, X.; Liu, X.; Li, Q.; Hu, J.; Chen, Q.; Yang, L.; Lu, Y. New amphiphilic polycarbonates with side functionalized cholesteryl groups as biomesogenic units: synthesis, structure and liquid crystal behavior. *RSC Advances* **2017**, *7*, 14176–14185. <https://doi.org/10.1039/c7ra00360a>. 28
- [49] Cowie, J.M.G.; Arrighi, V. *Polymers: Chemistry and Physics of Modern Materials*, 3rd ed.; CRC Press, 2007. 28
- [50] Finkelmann, H.; Kock, H.J.; Rehage, G. Investigations on Liquid Crystalline Polysiloxanes 3a) Liquid Crystalline Elastomers-A New Type of Liquid. *Makromol. Chem., Rapid Commun* **1981**, *2*, 317–322. 28

REFERENCES

- [51] Hu, J.S.; Zhang, B.Y.; Jia, Y.G.; Wang, Y. Structures and Properties of Side-Chain Cholesteric Liquid Crystalline Polyacrylates. *Polymer Journal* **2003**, *35*, 160–166. [28](#)
- [52] Yang, X.; Chen, S.; Chen, S.; Xu, H. Influencing factors on liquid crystalline properties of cholesterol side-chain liquid crystalline polymers without spacer: molecular weight and copolymerisation. *Liquid Crystals* **2019**, *46*, 1827–1842. <https://doi.org/10.1080/02678292.2019.1606352>. [28](#)
- [53] Klok, H.A.; Hwang, J.J.; Iyer, S.N.; Stupp, S.I. Cholesteryl-(L-lactic acid) building blocks for self-assembling biomaterials. *Macromolecules* **2002**, *35*, 746–759. <https://doi.org/10.1021/ma010907x>. [29](#)
- [54] Chiefari, J.; Chong, Y.K.; Ercole, F.; Krstina, J.; Jeffery, J.; Le, T.P.T.; Mayadunne, R.T.A.; Meijs, G.F.; Moad, C.L.; Moad, G.; et al. Living Free-Radical Polymerization by Reversible Addition-Fragmentation Chain Transfer: The RAFT Process. Technical report. [31](#)
- [55] Pascale Corpart, Sannois; Dominique Charmot, L.P.S.G.S.Z.Z.G.s.Y.T.B.O.D.M.N. METHOD FOR BLOCK POLYMER SYNTHESIS BY CONTROLLED RADICAL POLYMERISATION, 2000. [31](#)
- [56] Zhang, X.; Boissé, S.; Bui, C.; Albouy, P.A.; Brûlet, A.; Li, M.H.; Rieger, J.; Charleux, B. Amphiphilic liquid-crystal block copolymer nanofibers via RAFT-mediated dispersion polymerization. *Soft Matter* **2012**, *8*, 1130–1141. <https://doi.org/10.1039/c1sm06598j>. [35](#)
- [57] Huo, M.; Zhang, Y.; Zeng, M.; Liu, L.; Wei, Y.; Yuan, J. Morphology Evolution of Polymeric Assemblies Regulated with Fluoro-Containing Mesogen in Polymerization-Induced Self-Assembly. *Macromolecules* **2017**, *50*, 8192–8201. <https://doi.org/10.1021/acs.macromol.7b01437>. [36](#)
- [58] Huo, M.; Song, G.; Zhang, J.; Wei, Y.; Yuan, J. Nonspherical Liquid Crystalline Assemblies with Programmable Shape Transformation. *ACS Macro Letters* **2018**, *7*, 956–961. <https://doi.org/10.1021/acsmacrolett.8b00409>. [36](#), [79](#)

- [59] Li, X.; Jin, B.; Gao, Y.; Hayward, D.W.; Winnik, M.A.; Luo, Y.; Manners, I. Monodisperse Cylindrical Micelles of Controlled Length with a Liquid-Crystalline Perfluorinated Core by 1D “Self-Seeding”. *Angewandte Chemie* **2016**, *128*, 11564–11568. <https://doi.org/10.1002/ange.201604551>. 36
- [60] Guan, S.; Chen, A. Influence of Spacer Lengths on the Morphology of Biphenyl-Containing Liquid Crystalline Block Copolymer Nanoparticles via Polymerization-Induced Self-Assembly. *Macromolecules* **2020**, *53*, 6235–6245. <https://doi.org/10.1021/acs.macromol.0c00959>. 36
- [61] Guan, S.; Zhang, C.; Wen, W.; Qu, T.; Zheng, X.; Zhao, Y.; Chen, A. Formation of Anisotropic Liquid Crystalline Nanoparticles via Polymerization-Induced Hierarchical Self-Assembly. *ACS Macro Letters* **2018**, *7*, 358–363. <https://doi.org/10.1021/acsmacrolett.8b00082>. 36, 77
- [62] Wen, W.; Ouyang, W.; Guan, S.; Chen, A. Synthesis of azobenzene-containing liquid crystalline block copolymer nanoparticles: Via polymerization induced hierarchical self-assembly. *Polymer Chemistry* **2021**, *12*, 458–465. <https://doi.org/10.1039/d0py01442g>. 36
- [63] Wen, W.; Chen, A. The self-assembly of single chain Janus nanoparticles from azobenzene-containing block copolymers and reversible photoinduced morphology transitions. *Polymer Chemistry* **2021**, *12*, 2447–2456. <https://doi.org/10.1039/d1py00223f>. 36
- [64] Penfold, N.J.; Yeow, J.; Boyer, C.; Armes, S.P. Emerging Trends in Polymerization-Induced Self-Assembly, 2019. <https://doi.org/10.1021/acsmacrolett.9b00464>. 37
- [65] Jeng, S.C.; Hwang, S.J. Controlling the Alignment of Polyimide for Liquid Crystal Devices. In *High Performance Polymers - Polyimides Based - From Chemistry to Applications*; InTech, 2012. <https://doi.org/10.5772/53457>. 43
- [66] Glatter, V.O.; Kratky, O. *Small angle x-ray scattering*; Number 5, Academic Press Inc.: London, 1982. 51

REFERENCES

- [67] Glatter, O.; Kratky, O.; Kratky, H.C. *Small angle X-ray scattering*; Academic press, 1982. 51
- [68] Bolze, J.; Kogan, V.; Beckers, D.; Fransen, M. High-performance small- and wide-angle X-ray scattering (SAXS/WAXS) experiments on a multifunctional laboratory goniometer platform with easily exchangeable X-ray modules. *Review of Scientific Instruments* **2018**, *89*. <https://doi.org/10.1063/1.5041949>. 52
- [69] Williams, D.B.; Carter, C.B. *Transmission Electron Microscopy*; Springer US: Boston, MA, 2009. <https://doi.org/10.1007/978-0-387-76501-3>. 54
- [70] Coles, H.J.; Simon, R. High-resolution laser-addressed liquid crystal polymer storage displayst **1985**. 63
- [71] Meredith, G.R.; Vandusen, J.G.; Williams, D.J. Optical and Nonlinear Optical Characterization of Molecularly Doped Thermotropic Liquid Crystalline Polymers Introduction The ease of orientation of nematic liquid crystalline. *Macromolecules* **1982**, *15*, 1385–1389. 63
- [72] Tsvetkov, V.N.; Riumtsev, E.I.; Shtennikova, I.N.; Korneeva, E.V.; Krentsel, B.A.; Amerik, Y.B. INTRAMOLECULAR LIQUID-CRYSTAL ORDER IN POLYMERS WITH CHAIN SIDE GROUPS. *European Polymer Journal* **1973**, *9*, 481–492. 63
- [73] Craig, A.A.; Imrie, C.T. Effect of Spacer Length on the Thermal Properties of Side-chain Liquid-crystal Poly(methacrylate)s. Technical Report 4, 1994. 63
- [74] Zuffanti, S. Preparation of acyl chlorides with thionyl chloride. *Journal of Chemical Education* **1948**, *25*, 481. <https://doi.org/10.1021/ed025p481>. 65
- [75] Fesciyan, S.; Dahler, J.S.; Macromolecules ; Riseman, J.; Kirkwood, J.G.; Doi, M.; Edwards, S.F.; Zero, K.M.; Pécora, R.; Freed, K.F.; Jain, S.; et al.

REFERENCES

- Notes Synthesis of Methacrylate and Acrylate Monomers of Cholesteric Esters via Phase-Transfer Catalysis. Technical Report 2, 1983. 75
- [76] Yang, S.Y.; Ryu, I.; Kim, H.Y.; Kim, J.K.; Jang, S.K.; Russell, T.P. Nanoporous membranes with ultrahigh selectivity and flux for the filtration of viruses. *Advanced Materials* **2006**, *18*, 709–712. <https://doi.org/10.1002/adma.200501500>. 76
- [77] Jancar, J.; Douglas, J.F.; Starr, F.W.; Kumar, S.K.; Cassagnau, P.; Lesser, A.J.; Sternstein, S.S.; Buehler, M.J. Current issues in research on structure-property relationships in polymer nanocomposites, 2010. <https://doi.org/10.1016/j.polymer.2010.04.074>. 76
- [78] Kim, S.Y.; Lee, Y.M. Taxol-loaded block copolymer nanospheres composed of methoxy poly(ethylene glycol) and poly(-caprolactone) as novel anticancer drug carriers. *Biomaterials* **2001**, *22*, 1697–1704. 76
- [79] Fasolka, M.J.; Mayes, A.M. BLOCK COPOLYMER THIN FILMS **2001**. 76
- [80] Tseng, Y.C.; Darling, S.B. Block copolymer nanostructures for technology, 2010. <https://doi.org/10.3390/polym2040470>. 76
- [81] Bates, F.S.; Fredrickson, G.H. Block copolymers-designer soft materials. *Physics Today* **1999**, *52*, 32–38. <https://doi.org/10.1063/1.882522>. 76
- [82] Bhushan, B.; Schrickler, S.R. A review of block copolymer-based biomaterials that control protein and cell interactions, 2014. <https://doi.org/10.1002/jbm.a.34887>. 76
- [83] Riess, G. Micellization of block copolymers, 2003. [https://doi.org/10.1016/S0079-6700\(03\)00015-7](https://doi.org/10.1016/S0079-6700(03)00015-7). 76
- [84] Riess, G. Micellization of block copolymers, 2003. [https://doi.org/10.1016/S0079-6700\(03\)00015-7](https://doi.org/10.1016/S0079-6700(03)00015-7). 76, 77
- [85] Mai, Y.; Eisenberg, A. Self-assembly of block copolymers. *Chemical Society Reviews* **2012**, *41*, 5969–5985. <https://doi.org/10.1039/c2cs35115c>. 76

- [86] Kamata, Y.; Parnell, A.J.; Gutfreund, P.; Skoda, M.W.; Dennison, A.J.; Barker, R.; Mai, S.; Howse, J.R.; Ryan, A.J.; Torikai, N.; et al. Hydration and ordering of lamellar block copolymer films under controlled water vapor. *Macromolecules* **2014**, *47*, 8682–8690. <https://doi.org/10.1021/ma5014513>. 76
- [87] Warren, N.J.; Armes, S.P. Polymerization-induced self-assembly of block copolymer nano-objects via RAFT aqueous dispersion polymerization, 2014. <https://doi.org/10.1021/ja502843f>. 76
- [88] Warren, N.J.; Mykhaylyk, O.O.; Ryan, A.J.; Williams, M.; Doussineau, T.; Dugourd, P.; Antoine, R.; Portale, G.; Armes, S.P. Testing the vesicular morphology to destruction: Birth and death of diblock copolymer vesicles prepared via polymerization-induced self-assembly. *Journal of the American Chemical Society* **2015**, *137*, 1929–1937. <https://doi.org/10.1021/ja511423m>. 76, 96
- [89] Canning, S.L.; Smith, G.N.; Armes, S.P. A Critical Appraisal of RAFT-Mediated Polymerization-Induced Self-Assembly. *Macromolecules* **2016**, *49*, 1985–2001. <https://doi.org/10.1021/acs.macromol.5b02602>. 76
- [90] Mai, Y.; Eisenberg, A. Self-assembly of block copolymers. *Chemical Society Reviews* **2012**, *41*, 5969–5985. <https://doi.org/10.1039/c2cs35115c>. 77
- [91] Bajpai, A.K.; Shukla, S.K.; Bhanu, S.; Kankane, S. Responsive polymers in controlled drug delivery. *Progress in Polymer Science (Oxford)* **2008**, *33*, 1088–1118. <https://doi.org/10.1016/j.progpolymsci.2008.07.005>. 77
- [92] Guan, S.; Chen, A. One-Pot Synthesis of Cross-linked Block Copolymer Nanowires via Polymerization-Induced Hierarchical Self-Assembly and Photodimerization. *ACS Macro Letters* **2020**, *9*, 14–19. <https://doi.org/10.1021/acsmacrolett.9b00868>. 77
- [93] Blanazs, A.; Madsen, J.; Battaglia, G.; Ryan, A.J.; Armes, S.P. Mechanistic insights for block copolymer morphologies: How do worms form vesicles?

REFERENCES

- Journal of the American Chemical Society* **2011**, *133*, 16581–16587. <https://doi.org/10.1021/ja206301a>. 78
- [94] Zhang, B.; Lv, X.; Zhu, A.; Zheng, J.; Yang, Y.; An, Z. Morphological Stabilization of Block Copolymer Worms Using Asymmetric Cross-Linkers during Polymerization-Induced Self-Assembly. *Macromolecules* **2018**, *51*, 2776–2784. <https://doi.org/10.1021/acs.macromol.8b00246>. 78
- [95] Chen, X.; Liu, L.; Huo, M.; Zeng, M.; Peng, L.; Feng, A.; Wang, X.; Yuan, J. Direct Synthesis of Polymer Nanotubes by Aqueous Dispersion Polymerization of a Cyclodextrin/Styrene Complex. *Angewandte Chemie* **2017**, *129*, 16768–16772. <https://doi.org/10.1002/ange.201709129>. 78
- [96] Mellot, G.; Guigner, J.M.; Bouteiller, L.; Stoffelbach, F.; Rieger, J. Driving Polymerization-Induced Self-Assembly towards the Fibre Morphology. *Angewandte Chemie* **2019**, p. pp. <https://doi.org/10.1002/anie.201809370>. 78
- [97] Ding, Y.; Cai, M.; Cui, Z.; Huang, L.; Wang, L.; Lu, X.; Cai, Y. Synthesis of Low-Dimensional Polyion Complex Nanomaterials via Polymerization-Induced Electrostatic Self-Assembly. *Angewandte Chemie - International Edition* **2018**, *57*, 1053–1056. <https://doi.org/10.1002/anie.201710811>. 78
- [98] Wang, X.; Guerin, G.; Wang, H.; Wang, Y.; Manners, I.; Winnik, M.A. Cylindrical Block Copolymer Micelles and Co-Micelles of Controlled Length and Architecture. 78
- [99] Morton, M.; McGrath, J.E.; Juliano, P.C.; Polym Sci, J.; Kraus, G.; Naylor, F.E.; Rollmann, K.W.; Nguyen, A.; Delvaux, M.j.; Fetters, L.J.; et al. Colloidal and Morphological Behavior of Block and Graft Copolymers. *Polym. Prepr., Am. Chem. Soc., Div. Polym. Chem* **1980**, *13*, 14. 79
- [100] Volkov, V.V.; Plat6, N.A.; Takahara, A.; Kajiyama, T.; Amaya, N.; Murata, Y. Aggregation state and mesophase structure of comb-shaped polymers with fluorocarbon side groups **1992**. 79

REFERENCES

- [101] Zhao, W.; Ta, H.T.; Zhang, C.; Whittaker, A.K. Polymerization-Induced Self-Assembly (PISA) - Control over the Morphology of 19F-Containing Polymeric Nano-objects for Cell Uptake and Tracking. *Biomacromolecules* **2017**, *18*, 1145–1156. <https://doi.org/10.1021/acs.biomac.6b01788>. 79
- [102] Semsarilar, M.; Ladmiral, V.; Blanazs, A.; Armes, S.P. Poly(methacrylic acid)-based AB and ABC block copolymer nano-objects prepared via RAFT alcoholic dispersion polymerization. *Polym. Chem.* **2014**, *5*, 3466–3475. <https://doi.org/10.1039/C4PY00201F>. 79
- [103] Krupers, M.; Moiler, M. Semifluorinated diblock copolymers. Synthesis, characterisation and amphiphilic properties. *Macromol. Chem. Phys* **1997**, *198*, 2163–2179. 79
- [104] Soulestin, T.; Ladmiral, V.; Dos Santos, F.D.; Améduri, B. Vinylidene fluoride- and trifluoroethylene-containing fluorinated electroactive copolymers. How does chemistry impact properties? *Progress in Polymer Science* **2017**, *72*, 16–60. <https://doi.org/10.1016/j.progpolymsci.2017.04.004>. 79
- [105] Hirao, A.; Sugiyama, K.; Yokoyama, H. Precise synthesis and surface structures of architectural per- and semifluorinated polymers with well-defined structures. *Progress in Polymer Science* **2007**, *32*, 1393–1438. <https://doi.org/10.1016/j.progpolymsci.2007.08.001>. 79
- [106] Vitale, A.; Bongiovanni, R.; Ameduri, B. Fluorinated Oligomers and Polymers in Photopolymerization. *Chemical Reviews* **2015**, *115*, 8835–8866. <https://doi.org/10.1021/acs.chemrev.5b00120>. 79
- [107] Dorsman, I.R.; Derry, M.J.; Cunningham, V.J.; Brown, S.L.; Williams, C.N.; Armes, S.P. Tuning the vesicle-to-worm transition for thermoresponsive block copolymer vesicles prepared: Via polymerisation-induced self-assembly. *Polymer Chemistry* **2021**, *12*, 1224–1235. <https://doi.org/10.1039/d0py01713b>. 81

- [108] Iborra, A.; Díaz, G.; López, D.; Giussi, J.M.; Azzaroni, O. Copolymer based on lauryl methacrylate and poly(ethylene glycol) methyl ether methacrylate as amphiphilic macrosurfactant: Synthesis, characterization and their application as dispersing agent for carbon nanotubes. *European Polymer Journal* **2017**, *87*, 308–317. <https://doi.org/10.1016/j.eurpolymj.2016.12.027>. 84
- [109] Ma, W.; Ameduri, B.; Takahara, A. Molecular Aggregation Structure and Surface Properties of Biomimetic Catechol-Bearing Poly[2-(perfluorooctyl)ethyl acrylate] and Its Application to Superamphiphobic Coatings. *ACS Omega* **2020**, *5*, 8169–8180. <https://doi.org/10.1021/acsomega.0c00439>. 84
- [110] Barca, G.M.J.; Bertoni, C.; Carrington, L.; Datta, D.; De Silva, N.; Deustua, J.E.; Fedorov, D.G.; Gour, J.R.; Gunina, A.O.; Guidez, E.; et al. Recent developments in the general atomic and molecular electronic structure system. *The Journal of Chemical Physics* **2020**, *152*, 154102. <https://doi.org/10.1063/5.0005188>. 92
- [111] Filik, J.; Ashton, A.W.; Chang, P.C.Y.; Chater, P.A.; Day, S.J.; Drakopoulos, M.; Gerring, M.W.; Hart, M.L.; Magdysyuk, O.V.; Michalik, S.; et al. Processing two-dimensional X-ray diffraction and small-angle scattering data in DAWN 2j. *Journal of Applied Crystallography* **2017**, *50*, 959–966. <https://doi.org/10.1107/S1600576717004708>. 94
- [112] Narayanan, T.; Sztucki, M.; Zinn, T.; Kieffer, J.; Homs-Puron, A.; Gorini, J.; Van Vaerenbergh, P.; Boesecke, P. Performance of the time-resolved ultra-small-angle X-ray scattering beamline with the Extremely Brilliant Source. *Journal of Applied Crystallography* **2022**, *55*, 98–111. <https://doi.org/10.1107/S1600576721012693>. 94
- [113] Ilavsky, J.; Jemian, P.R. Irena : tool suite for modeling and analysis of small-angle scattering. *Journal of Applied Crystallography* **2009**, *42*, 347–353. <https://doi.org/10.1107/S0021889809002222>. 94

REFERENCES

- [114] Derry, M.J.; Mykhaylyk, O.O.; Ryan, A.J.; Armes, S.P. Thermoreversible crystallization-driven aggregation of diblock copolymer nanoparticles in mineral oil. *Chemical Science* **2018**, *9*, 4071–4082. <https://doi.org/10.1039/c8sc00762d>. 96
- [115] Cogswell, F.N.; Wissbrun, K.F. Rheology and processing of liquid crystal polymer melts. In *Rheology and Processing of Liquid Crystal Polymers*; Springer Netherlands: Dordrecht, 1996; pp. 86–134. https://doi.org/10.1007/978-94-009-1511-4_4. 117
- [116] Kagan, C.R.; Hyeon, T.; Kim, D.H.; Ruiz, R.; Tung, M.C.; Wong, H.S. Self-Assembly for electronics. *MRS Bulletin* **2020**, *45*, 807–814. <https://doi.org/10.1557/mrs.2020.248>. 123
- [117] Liu, C.C.; Franke, E.; Mignot, Y.; Xie, R.; Yeung, C.W.; Zhang, J.; Chi, C.; Zhang, C.; Farrell, R.; Lai, K.; et al. Directed self-assembly of block copolymers for 7 nanometre FinFET technology and beyond. *Nature Electronics* **2018**, *1*, 562–569. <https://doi.org/10.1038/s41928-018-0147-4>. 123
- [118] Nickmans, K.; Schenning, A.P.H.J. Directed Self-Assembly of Liquid-Crystalline Molecular Building Blocks for Sub-5 nm Nanopatterning. *Advanced Materials* **2018**, *30*. <https://doi.org/10.1002/adma.201703713>. 123
- [119] Bedolla Pantoja, M.A.; Abbott, N.L. Surface-Controlled Orientational Transitions in Elastically Strained Films of Liquid Crystal That Are Triggered by Vapors of Toluene. *ACS Applied Materials and Interfaces* **2016**, *8*, 13114–13122. <https://doi.org/10.1021/acsami.6b02139>. 133
- [120] Lee, M.; Cho, B.K.; Zin, W.C. Supramolecular structures from rod-coil block copolymers, 2001. <https://doi.org/10.1021/cr0001131>. 137